Design and Performance Evaluation of a Magnetically Geared Axial-Flux Permanent Magnet Generator

by

Lodewyk Brönn

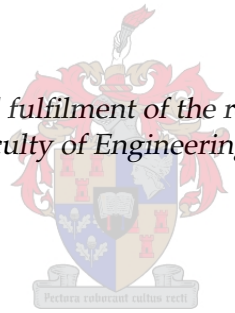

Thesis presented in partial fulfilment of the requirements for the degree Master of Science in the Faculty of Engineering at Stellenbosch University

Supervisor: R. Wang, PhD

March 2012

DECLARATION

By submitting this thesis electronically, I declare that the entirety of the work contained therein is my own, original work, that I am the sole author thereof (save to the extent explicitly otherwise stated), that reproduction and publication thereof by Stellenbosch University will not infringe any third party rights and that I have not previously in its entirety or in part submitted it for obtaining any qualification.

Date: March 2012 .....

ABSTRACT

Design and Performance Evaluation of a Magnetically Geared Axial-Flux Permanent Magnet Generator

L. Brönn

Thesis: MScEng (EE)

March 2012

This thesis is a description of how the first magnetically geared axial flux permanent magnet generator (MGAFG) is designed, constructed and experimentally evaluated. Magnetic gears (MGs) allow for contact-less power transfer and lubricant free operation, which may solve the reliability concerns with current mechanically geared wind energy converters.

However, the complex structure of MGs may present serious challenges to its design. Thus, special care should be given to the mechanical layout and the electromagnetic influence of every component.

The MGAFG can be configured to be magnetically coupled or decoupled. In the coupled configuration the permanent magnets (PMs) of the MG contribute to the total flux linkage in the PM generator (PMG). The coupled configuration is therefore more efficient. The processing time required to optimise the decoupled configuration is however much faster, since the MG and the PMG can be optimised separately.

The optimised results show that a torque density in excess of 100kNm/m^3 could be achieved, which is significantly higher than any of known electrical machines. However, owing to excessive losses in the mechanical support structures, the prototype exhibited lower torque density and poor efficiency. The design related aspects and issues are analysed and discussed in detail in an attempt to outline problem areas in the design process. Relevant recommendations are also given for future design improvements.

The costs of magnetic material accounts for over fifty percent of the total cost of the prototype. Therefore to make the manufacturing of the MGAFG more economically viable magnetic material should be minimised in the design process.

UITTREKSEL

Ontwerp en Prestasie Evaluering van 'n Magnetiese Geratte Aksiale-Vloed Permanent Magneet Generator

L. Brönn

Tesis: MScIng (EE)

Maart 2012

In hierdie tesis word die eerste magnetiese geratte aksiale vloed permanente magneet generator (MGAVG) ontwerp, vervaardig en eksperimenteel geëvalueer. In magnetiese ratte (MR) is daar geen kontak tussen werkende dele nie, daarom word geen smeermiddels benodig nie. Dit dra by tot die betroubaarheid van die ratkaste in wind energie generators en kan onderhoud grotendeels uitskakel.

Die komplekse struktuur van magnetiese ratte kan egter die betroubaarheid van die ontwerp juis verswak. Daarom moet die meganiese uitleg noukeurig beplan word sodat dit nie die elektromagnetiese werking ondermyn nie.

Die magnetiese rat (MR) en die permanente magneet generator (PMG) van die masjien kan magneties of sonder magnetiese koppeling verbind word. In die gekoppelde konfigurasie dra all die permanente magnete van die MR gesamentlik by tot die totale vloed-koppeling in die PMG. Wat die magnetiese gekoppelde konfigurasie meer doeltrefend maak. Minder tyd word benodig om die nie magnetiese gekoppelde konfigurasie te optimaliseer omdat die MR en die PMG apart geoptimaliseer kan word.

Die optimale resultate toon dat 'n wringkrag van meer as $100\text{kNm}/^3$ bereik kan word, wat aansienlik beter is as die van bekende elektriese masjiene.

Maar as gevolg van oormatige verliese in die meganiese strukture, toon die prototipe lae wringkrag digtheid en swak doeltreffendheid. Die ontwerp probleme word ontleed en bespreek in 'n poging om probleem areas in die ontwerp te identifiseer. Relevante aanbevelings word gegee vir toekomstige ontwerp verbeterings.

Die koste van die magnetiese material verteenwoordig meer as vyftig persent van die vervaardigings koste van die prototipe. Koste kan bespaar word op die vervaardiging van die MGAVG deur die hoeveelheid magnete wat gebruik word te beperk.

ACKNOWLEDGEMENTS

Thanks to...

- **Jesus Christ** - Lord and Saviour.
  for undeserved love and opportunities.
- **Dr. R.J. Wang** - Study leader
  for wise counsel, encouragement and patience even when it was not deserved.
- **Prof. M.J. Kamper**
  for wise counsel, motivation and providing financial support to the project.
- **P.H. Petzer, A. Swart and M.H. Jumat** - The electrical workshop staff
  for helping with all the prototype building and wise counsel.
- **Me. D. Kleyn** - Electrical and electronic secretary
  for helping with procurements.
- **EMLab colleagues**
  for their camaraderie and help.
- **Mom and Dad**
  for their loving support and encouragement throughout my studies.

CONTENTS

LIST OF FIGURES

LIST OF TABLES

NOMENCLATURE

Constants

C_p	Betz criterion	[0.593]
π	Pi	[3.141 592 654]

Variables

A_c	Coil cross-section area	[mm^2]
A_{con}	Area of a single conductor	[mm^2]
A_{cu}	Available area for placing conductors (copper)	[mm^2]
ag_h	High-speed rotor air-gap height	[m]
ag_l	Low-speed rotor air-gap height	[m]
A_s	Blade swept area	[m^2]
ag_s	Stator air-gap height	[m]
B_r	Radial flux distribution	[T]
B_{rA}	Radial flux distribution (without flux-modulator)	[T]
B_{rB}	Radial flux distribution (with flux-modulator)	[T]
b_{rm}	Fourier coefficient for the radial flux density distribution (without FM)	[T]
B_θ	Circumferential flux distribution	[T]
$B_{\theta A}$	Circumferential flux distribution (without FM)	[T]
$B_{\theta B}$	Circumferential flux distribution (with FM)	[T]
$b_{\theta m}$	Fourier coefficient for the circumferential flux density distribution (without FM)	[T]
C	Bearing dynamic load rating	[kN]
c_0	Learning factor	[ ]
c_1	Learning factor	[ ]
c_2	Learning factor	[ ]
c_3	Learning factor	[ ]
C_p	Power coefficient (Betz criterion)	[ ]
D	Outer diameter	[m]
d	Inner diameter	[m]
E_1	Electromotive force due to high-speed rotor	[V]
E_2	Electromotive force due to low-speed rotor	[V]
E_a	RMS value of the phase EMF	[V]
E_d	d-axis speed voltage	[V]

E_{kw}	Kinetic energy	[J]
E_q	q-axis speed voltage	[V]
F	Force	[N]
F_{avg}	Average force	[N]
f_c	Cogging factor	[ ]
F_{H_A}	Axial force of high-speed rotor	[N]
F_{H_R}	Radial force of high-speed rotor	[N]
F_{MP_A}	Axial force of flux-modulator	[N]
F_{MP_R}	Radial force of flux-modulator	[N]
F_{L_A}	Axial force of low-speed rotor	[N]
F_{L_R}	Radial force of low-speed rotor	[N]
f_{out}	Output electrical frequency	[Hz]
F_{R_A}	Axial force of self-centring lock	[N]
F_{rod}	Force on rod	[N]
F_{R_R}	Radial force of self-centring lock	[N]
G	Best value achieved so far by any particle	[ ]
G_r	Gear ratio	[ ]
hs_h	High-speed rotor height	[m]
hs_{ph}	High-speed rotor core height (gear side)	[m]
hs_{ph2}	High-speed rotor core height (stator side)	[m]
hs_{pp}	High-speed rotor pole pitch ratio (gear side)	[ ]
hs_{pp2}	High-speed rotor pole pitch (stator side)	[ ]
I	Current space phaser	[A]
i_{abc}	Instantaneous three phase currents	[A]
I_d	d-axis current	[A]
I_d1	d1 current component	[A]
i_{dq0}	dq currents	[A]
I_q	q-axis current	[A]
I_q1	q1 current component	[A]
i_{rms}	RMS current value	[A]
I_{rms}	RMS current value	[A]
I_s	Stator current	[A]
I_{s1}	Current amplitude	[A]
J	Current density	[A/mm^2]

k_f	Filling factor	[ ]
K_p	Park's transformation	[ ]
L	Particle's own best value achieved	[ ]
l	Active length of a coil	[m]
L_{10}	Bearing basic rating life	[Mrev]
L_{10h}	Bearing rating life	[hours]
L_e	Endwinding leakage inductance per phase	[H]
l_e	End-winding length of a coil	[m]
ls_h	Low-speed rotor core height	[m]
L_{linear}	Linear model length	[m]
L_m	Main inductance	[H]
ls_{ph}	Low-speed rotor pole height	[m]
ls_{pp}	Low-speed rotor pole pitch ratio	[ ]
L_s	Stator inductance	[H]
mp_h	Flux-modulator height	[m]
mp_p	Flux-modulator pitch ratio	[ ]
M_R	Bending moment of self-centring lock	[Nm]
N	Best solution in its neighbourhood	[ ]
n	Operating speed	[rpm]
N_c	Smallest common multiple between the number of pole-pairs and FM pieces	[ ]
n_H	High-speed rotor speed	[rpm]
n_L	Low-speed rotor speed	[rpm]
N_p	Number of poles	[ ]
N_R	Bearing power loss	[W]
n_s	Number of modulation pieces	[ ]
$n_{strands}$	Number of strands per conductor	[ ]
n_{tp}	Number of turns in series per phase	[ ]
P	Bearing equivalent load	[N]
p	Number of pole-pairs on a permanent magnet rotor	[ ]
P_a	Power available in the wind	[W]
P_c	Total core losses	[W]
P_{cu}	Copper losses	[W]
P_f	Power factor	[ ]
P_{gear}	Gear losses	[W]

p_H	Number of pole-pairs on the high-speed rotor	[ ]
P_{in}	Input power	[W]
p_L	Number of pole-pairs on the low-speed rotor	[ ]
P_{Loss}	Total losses	[W]
P_{out}	Output power	[W]
$P_{windage}$	Windage losses	[W]
q_1	Number of coils per pole per phase	[ ]
R	Linear model average radius	[m]
r	Radial distance	[m]
r_1	Uniformly distributed random number in (0, 1)	[ ]
r_2	Uniformly distributed random number in (0, 1)	[ ]
r_3	Uniformly distributed random number in (0, 1)	[ ]
R_c	Core loss resistance	[Ω]
R_s	Stator resistance	[Ω]
S	Apparent power	[VA]
s_{cu}	Cross section area of the wire	[m^2]
s_h	Stator height	[m]
ss_h	Slot height	[m]
ss_w	Slot width	[m]
ss_{ta}	Slot tooth angle	[deg]
ss_{tt}	Slot tooth thickness	[m]
ss_{tw}	Slot tooth width	[m]
T	Linear model thickness	[m]
t	Time	[s]
T_{avg}	Average torque	[Nm]
T_D	Torque density	[kNm/m^3]
T_H	High-speed rotor torque	[Nm]
T_{He}	High-speed rotor steady state torque	[Nm]
T_L	Low-speed rotor torque	[Nm]
T_{Le}	Low-speed rotor steady state torque	[Nm]
T_{MP}	Flux-modulator torque	[Nm]
T_{normal}	Average torque for normal magnet placement	[Nm]
$T_{shifted}$	Average torque for shifted magnets	[Nm]
v	Bearing lubricant operating viscosity	[mm^2/s]

V_a	Volume of air interacting with the turbine	[m^3]
V_d	d-axis terminal voltage component	[V]
V_{GEAR}	Volume of gear	[m^3]
v_i	Velocity at the previous iteration	[ ]
v_i'	Velocity at the current iteration	[ ]
V_q	q-axis terminal voltage component	[V]
v_w	Wind velocity	[m/s]
v_{rms}	RMS voltage value	[V]
V_{rms}	RMS voltage value	[V]
x_i	Position at the previous iteration	[ ]
x_i'	Position at the current iteration	[ ]
z	Number of turns per coil	[ ]

Greek Alphabet Symbols

α	Slot pitch angle	[deg]
η	Efficiency	[ ]
γ	The integer multiple of magnets out of phase with each other	[ ]
λ_{abc}	Three phase flux-linkages	[Wb − t]
λ_d	d-axis stator flux-linkage	[Wb − t]
λ_{dq0}	dq-axis stator flux-linkage	[Wb − t]
λ_q	q-axis stator flux-linkage	[Wb − t]
λ_{rj}	Fourier coefficients of the flux density distribution, radial (with FM)	[ ]
$\lambda_{\theta j}$	Fourier coefficients of the flux density distribution, circumferential (with FM)	[ ]
ω_r	Rotational velocity of the permanent magnet rotor	[rad/s]
ω_s	Rotational velocity of the flux-modulator	[rad/s]
μ_o	Permeability of air	[H/m]
ρ_a	Air density	[kg/m^3]
σ_T	Electric conductivity of the wire at temperature T	[ ]
θ	Rotation angle	[rad]
θ_m	Offset angle	[ ]
θ_o	Angle that each magnet needs to be shifted relative to the others	[rad]

Abbreviations

2D	Two Dimensional
3D	Three Dimensional

EMF Electromotive force

EP Extreme Pressure

FE Finite Element

FEA Finite Element Analysis

FEM Finite Element Model

FM Flux Modulator

HS High Speed

LS Low Speed

MG Magnetic Gear

MGAFG Magnetically Geared Axial Flux Generator

MGPMG Magnetically Geared Permanent Magnet Generator

MP Modulation Pieces (Flux Modulator)

PM Permanent Magnet

PMG Permanent Magnet Generator

Subscripts

d d-axis

H High-speed rotor

i Index of the variable

L Low-speed rotor

rms Root mean square value

q q-axis

CHAPTER 1

LITERATURE REVIEW

1.1 Introduction

In recent years renewable energy power generation systems have received a great deal of attention. Usually a high speed electrical machine is used together with a mechanical gearbox, which often requires gear lubrication and cooling, while noise, vibration and reliability are also significant issues.

Take the wind power industry for an example. Typically wind turbines have a 20 year designed lifetime, the gearboxes however commonly fail within an operational period of 5 years (24). The 20 year lifetime goal is itself a reduction from an earlier 30 year lifetime design goal.

In this project a magnetically geared permanent magnet generator is proposed and evaluated, in an attempt to address the major problems of mechanical gears. Magnetic gears (MGs) offer significant advantages, such as contact-less power transfer, lubricant free operation, inherent over load protection, high torque densities, potential for high efficiency and little or no maintenance.

Despite these advantages, MGs have received little attention from both research institutions and industry, due to the relative complexity of MGs and the shortcomings of earlier permanent magnets (PMs).

In the 80s rare earth PMs, especially neodymium-iron-boron ($Nd_2Fe_{14}B$) magnets, started to become commercially available (25). These rare earth magnets revived the interest in PM machines and magnetic gears. This can be observed in the magnetic gear research activity histogram (see Figure 1.1). The histogram illustrates the number of publications written per year over the last 100 years and reviewed by the researcher. From the figure it can be observed that MGs started to become more popular in the 1990s just after the commercialisation of rare earth PMs.

The advantages that MGs offer over traditional mechanical gears and the high energy rare earth PMs readily available are the main drives behind recent MG development.

The operating principle of MG is similar to that of mechanical gears, except that all the gear teeth are replaced with magnets, as illustrated in Figure 1.2. The magnetic force between the magnets on the opposing shafts will transfer the force between the shafts in the same way that the gear teeth transfer power by pushing or resisting the opposing teeth.

1.2 Magnetic Gear History

Magnetic gearing can be traced back to the beginning of the 20^{th} century. Armstrong (1) designed an electromagnetic spur gear in 1901. The gear consisted of two gears, one with electromagnets as the gear teeth and the other with steel pieces. The electromagnets on the primary gear were switched on and off

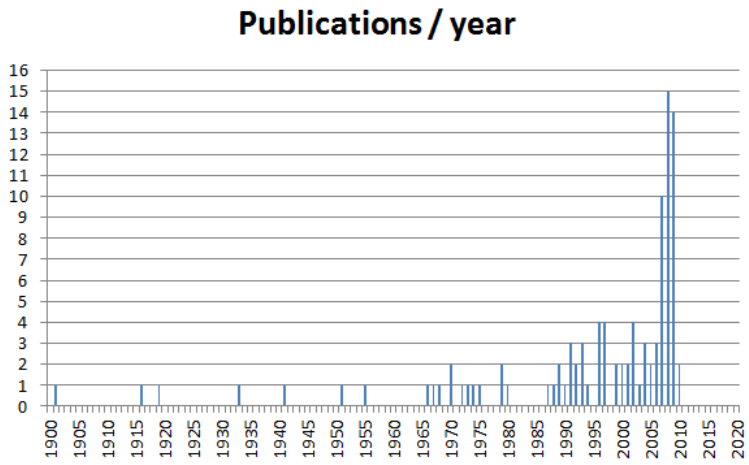

Figure 1.1: Magnetic Gear Histogram

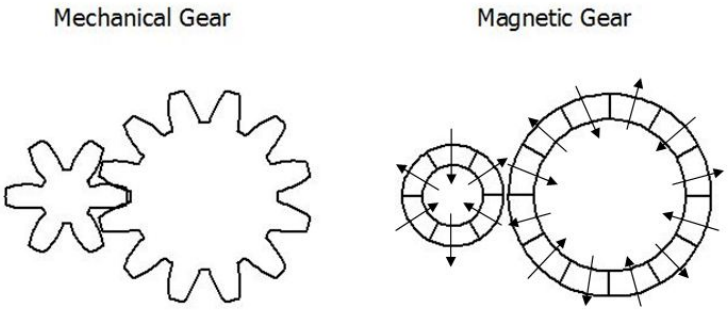

Figure 1.2: Comparison Between Mechanical- and Magnetic-Gears

according to their relative position to the secondary gear teeth. An illustration can be seen in Figure 1.3. The gear had the advantage of contact-less power transfer and low noise operation, but fell short in the amount of torque that could be transferred for the volume occupied. Only one to three electromagnets transferred torque at any given moment. The electromagnets had to be connected electrically with slip rings, which caused unnecessary losses and needed high maintenance.

In 1916 Neuland (2) invented a far superior magnetic gear. The gear consisted of three main parts, a laminated steel outer- and inner-rotor and magnetic modulation pieces in between the two steel rotors (see Figure 1.4). The modulation pieces were shaped to modulate magnetic flux so that the inner rotor and the outer rotor saw the correct harmonics in accordance with the number of teeth on each shaft. The ratio of teeth on the outer- and inner-rotor determined the gear ratio between the shafts. The torque density of this configuration was greatly improved compared to the spur-type design from (1), since most of the gear teeth transfered torque at any given moment. The patent also described a few variations on the design. The problem with this design was that there were only magnets on one of the shafts, which led to impractical air-gap sizes.

Zweigbergk (26) designed an electromagnetic gear in 1919. The machine was known as Electric-Continuous-Variable-Transmission (or E-CVT). E-CVT was basically two electrical machines joined to-

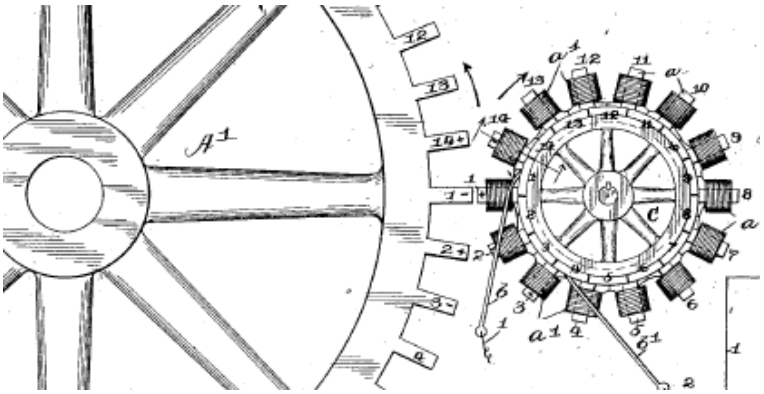

Figure 1.3: First Magnetic Gear (1)

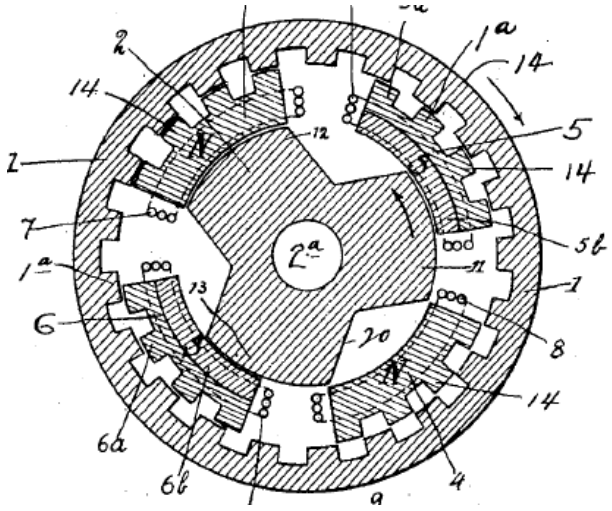

Figure 1.4: Coaxial Magnetic Gear (2)

gether; one motor and one generator. The generator acted as the input and the electricity generated drove the motor, the motor was the output. The advantage of the machine described was that the output speed of the motor could be controlled; hence continuous variable transmission could be obtained. CVT could be very advantageous especially in renewable energy applications. If constant output speed could be maintained the power electronics controlling the generated electricity quality could be reduced to a simple system. The disadvantage of this E-CVT was that two machines were needed, which doubled the amount of magnetic and electrical materials needed and most likely one of the machines would need slip rings. The efficiency of the system would then be the combined efficiency of the individual systems.

In 1933 Chubb (3) incorporated a simple steel rotor into a vernier machine. The steel rotor had a predetermined number of steel segments as can be seen in Figure 1.5 part number (32). The steel segments modulated the magnetic flux from the stator (30) to the rotor (34) in a predetermined ratio. This acted as a magnetic gearing mechanism. The machine was designed for small applications such as clock-motors. The extra rotor increased the air-gap length and thus decreased the amount of power that could be transferred.

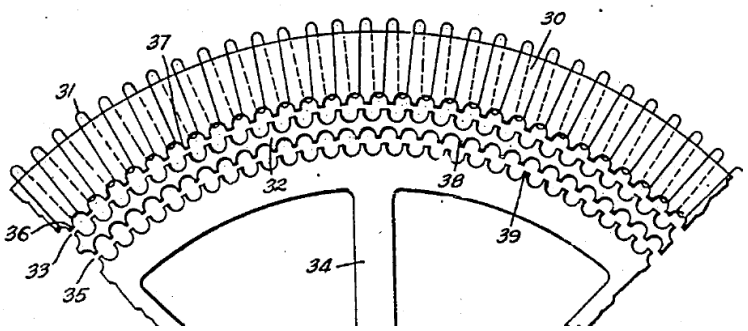

Figure 1.5: Magnetic Geared Vernier Motor (3)

H.T. Faus designed a magnetic spur-type gear in 1941, (4). The gear operated in the same manner as the electromagnetic spur gear from (1) as described above. The only difference was that it used permanent magnets (Figure 1.6 illustrates the original design from the patent). All the north poles of the magnets pointed radially outwards, thus the torque was transferred between the shafts by the repulsion of the identical poles of the magnets. When the maximum torque was exceeded in this design the gear slipped and caused one of the permanent magnets to break, since the PMs still made contact. Thus this design was not suitable when overload protection was necessary. Although it improved on the previous spur-type designs by eliminating the electromagnets, which decreased the weight and the size of the gear while making the control circuit dispensable, the weak utilisation of the PMs in the spur-type design made the design impractical. In the patent a worm-type gear was also described.

In 1901 when Armstrong (1) designed his gear, PMs were not yet strong enough for efficient gearing, but as the PM technology improved, more and more PM gears appeared.

In 1951 Hurvitz (5) invented a spur-type magnetic gearbox, where the gear ratio could be changed by switching the active gears by means of electromagnets. The whole system was not efficient and very bulky (Figure 1.7 illustrates his design).

In 1955 Cluwen's patent (6) described a number of spur-type magnetic gear arrangements from normal spur gear arrangements to gearbox arrangements where the gear ratio could be changed by means

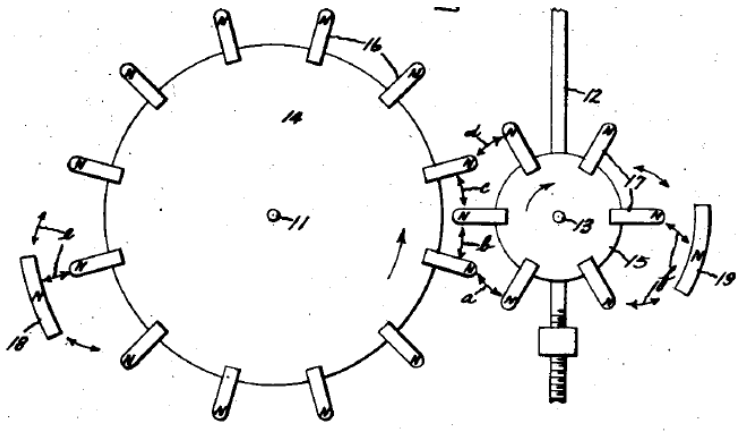

Figure 1.6: Permanent Magnet Spur-Type Gear (4)

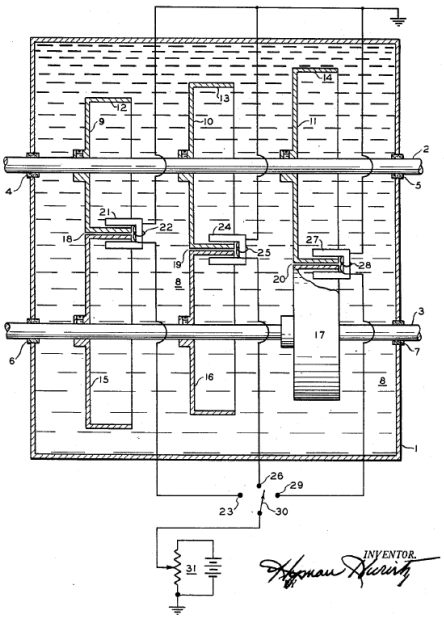

Figure 1.7: Electromagnetic Spur-Type Gearbox (5)

of moving the driven shaft mechanically to a new position (see Figure 1.8). The patent also described gear arrangements where the axes of rotation were at an angle to one another.

In 1966 Baermann (7) invented a device for electricity generation. The device was a belt and pulley system made of permanent magnets (see Figure 1.9). The belt was then moved past electric coils, where the moving magnets induced an electric current in the coils. The movement of the belt was accomplished by the magnetic attraction between the poles on the belt and the pulleys.

In 1967 Reese (27) invented a magnetic gear similar to the one described in (2). The difference was that the inner rotor contained the PMs (see Figure 1.10 for an illustration of the gear). The two outer rotors had a different number of teeth. The inner PM-rotor was the high speed shaft, the middle rotor was the output shaft and the outer rotor was kept stationary. When the inner PMs were rotated, the middle rotor would rotate with it. The magnetic flux of the PM's tended to take the path with the lowest permeability, which is through the steel teeth of the rotors. This made the teeth of the rotor rotate in

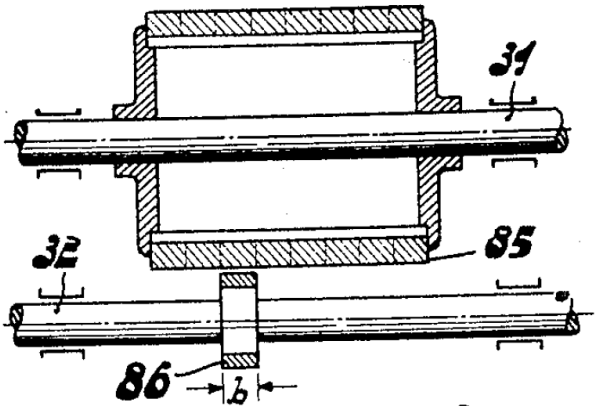

Figure 1.8: Spur-Type Magnetic Gearbox (6)

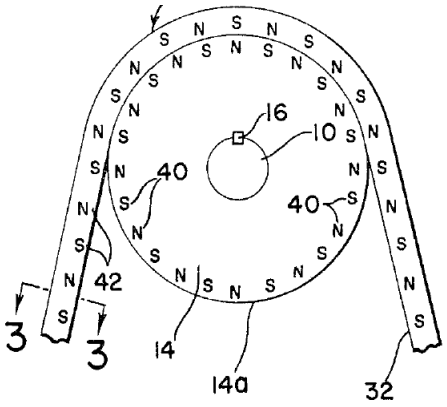

Figure 1.9: Belt and Pulley Permanent Magnet Device (7)

accordance with the magnetic flux of the PMs. The speed of the rotor then became a function of the ratio of the number of teeth between the rotors and the number of PM poles.

In 1968 Martin (8) designed a similar gear as (2) and (27), by replacing the outer rotor with PM's (see Figure 1.11). The flux-modulator (28) modulated the magnetic flux between the outer- and the inner-rotor. The operating principle of the flux-modulation can be explained with the help of Figure 1.12. The right side of each picture represents the PMs on the outer rotor. The middle black pieces represents the flux-modulator and the left side represents the flux content that the inner rotor would interact with. Figure 1.12A is an illustration of the inner rotor interacting with a north pole. Figure 1.12B is an illustration of what happens when the modulation pieces are moved just by one space and the inner rotor faces a south pole. If the modulation pieces are spaced differently the inner rotor would interact with a north and a south pole (as seen in Figure 1.12C). The flux-modulator controls how the two rotors interact with each other. The gear ratio is a function of the number of PM's on both rotors and the number of modulation pieces in the flux modulator. The patent also described a number of designs where the flux-modulator was reconfigured in other configurations, but the same operating principle counted.

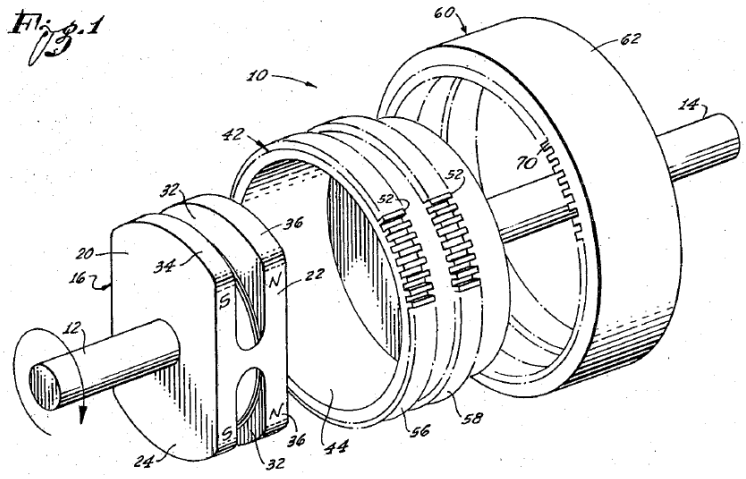

Figure 1.10: Coaxial Magnetic Gear

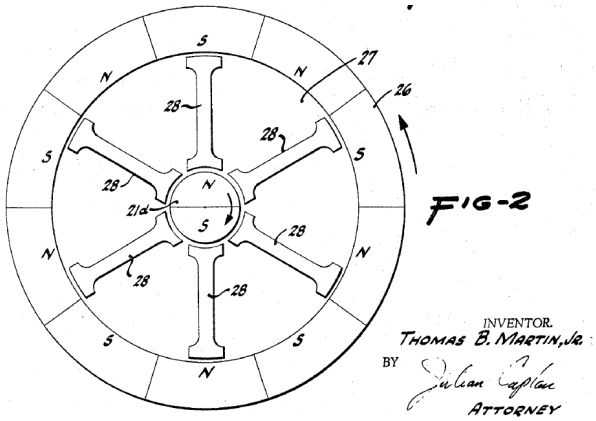

Figure 1.11: Coaxial Magnetic Gear (Shutter-Type) (8)

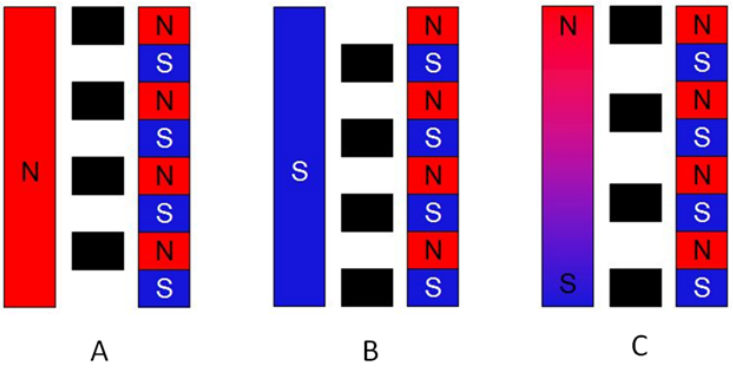

Figure 1.12: Modulation Pieces Explained

In 1970 Rand (9) took out a patent for a simple spur-type magnetic gear. He designed the PMs so that both the north and south poles of the PMs faced radially outward (see Figure 1.13). This increased the amount of magnetic material needed and the cost of manufacturing.

In 1972 Laing (28) took out a patent for a magnetic gear very similar to (8) of 1968. The difference was that the flux-modulator in between the PM rotors were a bit different and that only every second pole on the rotors contained a PM (see Figure 1.14). In 1973 Laing took out another patent, (29), this patent described the magnetic gear incorporated into a centrifugal pump. The advantage of using a magnetic gear in a pump is that the two rotating shafts transferred torque without physical contact, thus the pump could be sealed.

Kaegi (30) proposed a coaxial magnetic gear for use in pumps where the advantage of contact-less power transfer made the gear ideal in sealed chambers (1979). The patent described the design of the chamber wall to minimise losses and still keep the mechanical strength of a solid wall.

Sakai (31) patented a planetary magnetic gear in 1989 where each of the planet gears was connected to a pump, so one input shaft could drive multiple pumps. The patent also described a few different planet arrangements for magnetic gears.

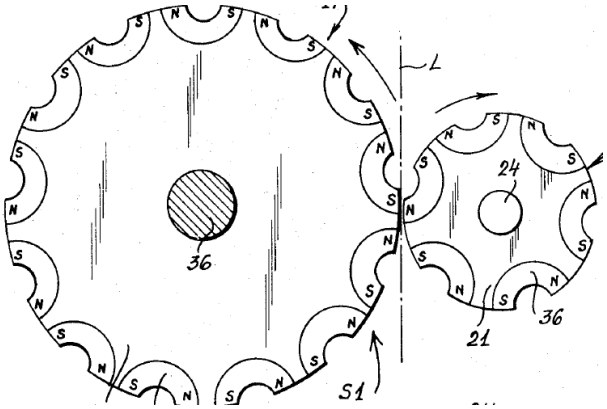

Figure 1.13: Spur-Type Magnetic Gear with U-Magnets (9)

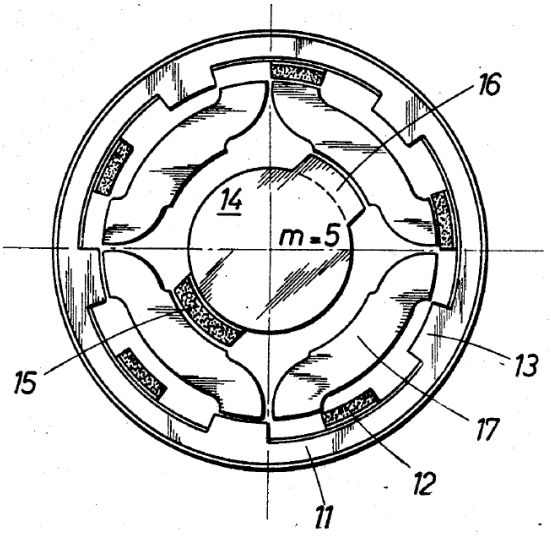

Figure 1.14: Coaxial Magnetic Gear

Hesmondhalgh *et al.*(1980) (32) proposed an array of Neuland's (2) magnetic gears (see Figure 1.15), in a hope that the array of gears would increase the maximum torque and efficiency and reduced the cogging torque. However, the total efficiency for the system was very low and the combined gears made the whole system too large and complex.

K. Tsurumoto was the inventor of the axial flux disk type spur magnetic gear (see Figure 1.16). In 1987 Tsurumoto (33) published his first paper on the non-contact magnetic gear. The permanent magnet material used was samarium-cobalt. The gear had a gear ratio of 1/3. The maximum torque that could be transferred was 5.5 Nm. In 1988 he described an attempt to improve the performance of the gear by mounting the magnets directly on a soft steel plate or a yoke (34). His conclusion was that identical gears could be used for both internal and external meshing.

The next paper was published in 1989, (35), it expanded on the previous article and concluded that the output torque could be 3.2 times improved if the magnets were placed on yokes.

Tsurumoto published another paper in 1990, (36), in which he described the design and overlap area of PM's and the performance characteristics of circular arc magnetic gears. He concluded that circular

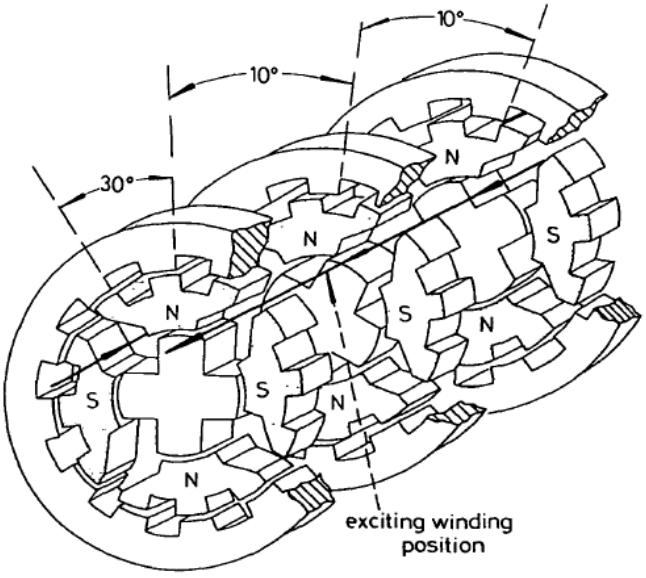

Figure 1.15: A Multi-Element Magnetic Gear

arc magnetic gears are 6% more efficient than those in his original design. The efficiency increase was due to the extra PM material in the meshing area.

In (37) Tsurumoto investigated the mechanism by which magnetic force was generated in the meshing area of the two opposing rotors. In 1992 he wrote a paper (38) about using a two-dimensional model was used an approximation of the generated magnetic force between the main contacting and intersecting zones of a magnetic gear using permanent magnets.

In 1993 a paper was published (39), which dealt with methods of high-speed start-up enabling direct connection to a driving motor. It was found that a trial magnetic gear could be started at a high speed of 1500 rpm by utilizing an eddy current effect.

An interesting paper (40) was written in 2002 that described a superconducting axial flux magnetic gear. Superconducting magnets can be several times stronger than rare earth magnets. However this required constant refrigeration which increased the total size and mass. The author also described the development of a three dimensional electromagnetic field analysis program to analyse characteristics of the proposed gear. Two superconducting magnetic gears with different configurations were manufactured and tested. The test results did not show good agreement with the calculated results, due to scatter in the experimental results. Superconducting magnetic gears could greatly improve the maximum torque that can be transferred when compared to normal permanent magnetic gears.

In the next paper (10) a magnetic worm gear was described (1993). The proposed gear has a gear ratio of 1:33. The original design had a low maximum torque capability, due to a large air-gap. The air-gap was then decreased by mating the worm gear with the wheel (as can be seen in Figure 1.17) and the output torque increased by about 1.5 times. However, the intricate parts increased the fabrication and assembly costs. The magnetic worm gear was feasible but the complexity and the costs of manufacturing were only worthwhile in applications where the advantages of magnetic gears were necessary.

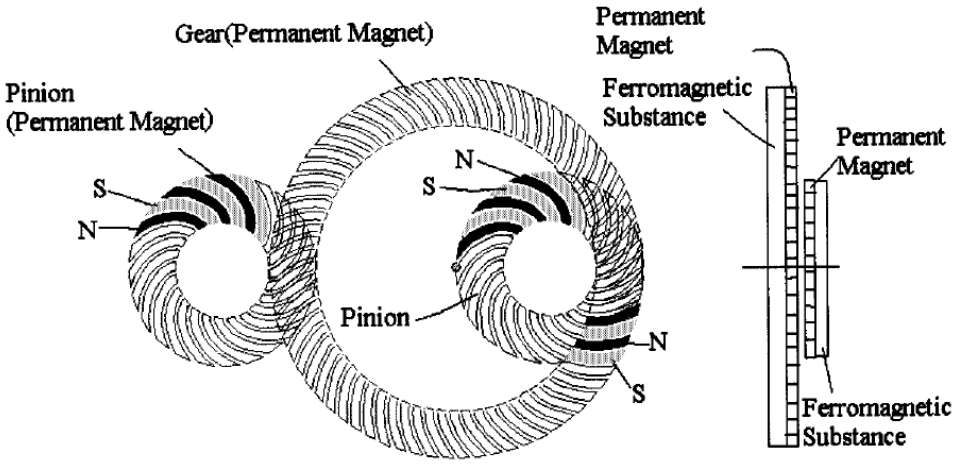

Figure 1.16: Axial-Flux Disk-Type Spur Magnetic Gear

Magnetic skew gears were discussed in (41; 42). The gear consisted of two worm mates and no wheel gear. Thus only a small magnetic area was responsible for the transfer of torque at any given moment. This design was worse than the design of 1993 because of the small area that could be used to transfer power, but the fabrication cost was decreased.

In 1996 a paper, (11), was published where a perpendicular magnetic gear was designed, built and experimentally evaluated (an illustration of the proposed gear can be seen in Figure 1.18). The paper described a critical separation distance (d in Figure 1.18) where if the air-gap length was smaller than the critical distance the transmitted torque could be increased by increasing the number of poles.

Yao *et al.* (from 1996 to 1997) described the coupling between spur-type magnetic gears. The first paper, (43), described the coupling of spur-type magnetic gears with both two- and three-dimensional finite element analysis (FEA). The conclusion was that for a 2mm air-gap the torque could be increased by increasing the number of poles. The torque was inversely proportional to the number of poles when the number of poles was larger than ten.

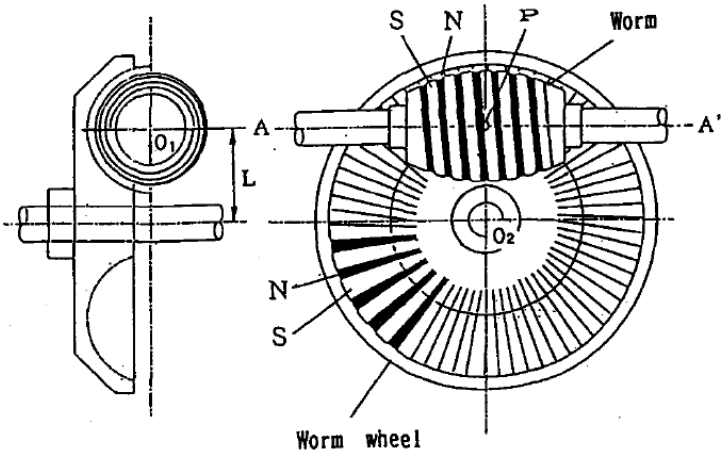

Figure 1.17: Magnetic Worm Gear, (10)

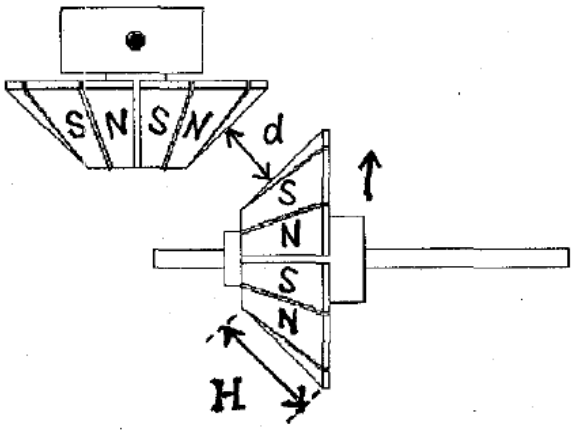

Figure 1.18: Perpendicular Magnetic Gear (11)

In the next paper (44) the optimization conclusions of a 2D FEA simulation were described. It was concluded that with a fixed air-gap distance a maximum torque could be obtained for a particular number of poles. The number of poles increased as the ratio of the radius to the thickness of the magnets increased. The number of poles decreased when an iron yoke was added.

In the following paper (45) the authors attempted to prove the conclusions made in the previous two papers by experimental testing.

Furlani (46) presented a formula to calculate the coupling between spur-type magnetic gears in 1997. The formula was based on two-dimensional analytical analysis and it was expressed as a finite sum of elementary functions. The formula was demonstrated practically and was verified using 2D FEA. The formula was ideal for parametric analysis.

In 2000 Yao *et al.* patented (47) a method designing an optimal spur-type magnetic gear.

Further work on spur-type magnetic gears include (48; 49)

Ackerman *et al.* (12) received a patent in 1997 for a coaxial magnetic gear. The gear was very similar to the earlier designs of 1960 ((28) and (50)) except that the flux-modulator was simplified and connected (see Figure 1.19A). There were three parts which were movable relative to each other. One of the rotors was connected to a drive and one kept stationary, while the remaining one would be the output shaft.

In 1999 Ackerman took out another patent (51) for the same kind of gear, except that the flux-modulator was moved to the outer rotor (see Figure 1.19B).

Atallah *et al.* (2000) wrote a paper (13) on a "novel" magnetic gear. The gear was fundamentally the same as Ackerman's 1997 gear, except that the flux-modulator was not connected (see Figure 20). In the paper the relationship between the number of poles and the number of modulation pieces in the gear were described to determine the gear ratio. It was claimed that by using rare earth magnets a torque density exceeding 100 kNm/m^3 could be achieved.

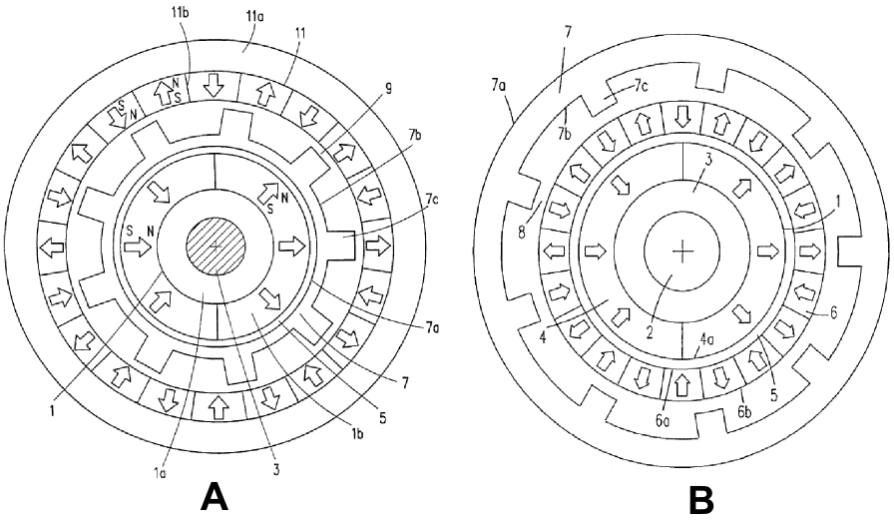

Figure 1.19: Coaxial Magnetic Gears, (12). A) Middle Flux-Modulator. B) Outer Flux-Modulator

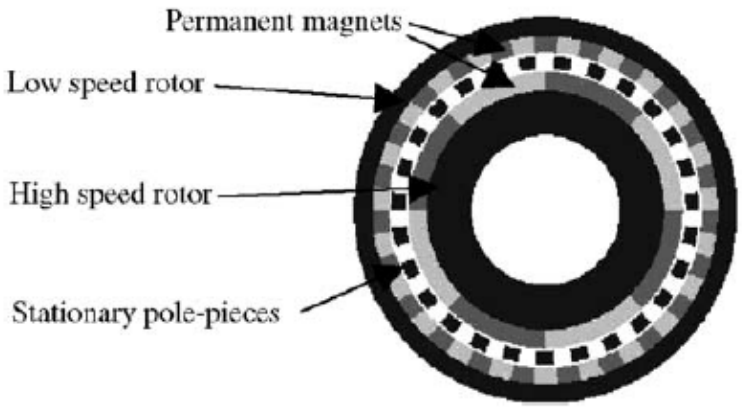

Figure 1.20: Coaxial Magnetic Gear (Unconnected Modulation Pieces), (13)

In 2003 Rasmussen wrote a paper, (14), on a coaxial magnetic gear, the same as described above, except that the inner rotor's magnets were arranged in a spoke-type arrangement and not surface mounted (see Figure 1.21). It was calculated that the gear would have a gear ratio of 1:5.5 and a stall torque of 27 Nm. However, the experimental results showed a stall torque of only 16 Nm. The reduction in the stall torque seemed to be caused by the end-effects of the short stack length of the magnets. In the paper MG is also compared with conventional mechanical gears with the same gear ratio and maximum torque capabilities. It was concluded that a theoretical efficiency of 96% could be reached if the end-effect losses were minimized and the gear had a higher torque density when compared to other mechanical gears.

In 2004 Atallah *et al*. (52) improved their previous paper on coaxial magnetic gears by demonstrating that an efficiency of 97% could be reached for transmitted torque values higher than 75% of the pull-out torque.

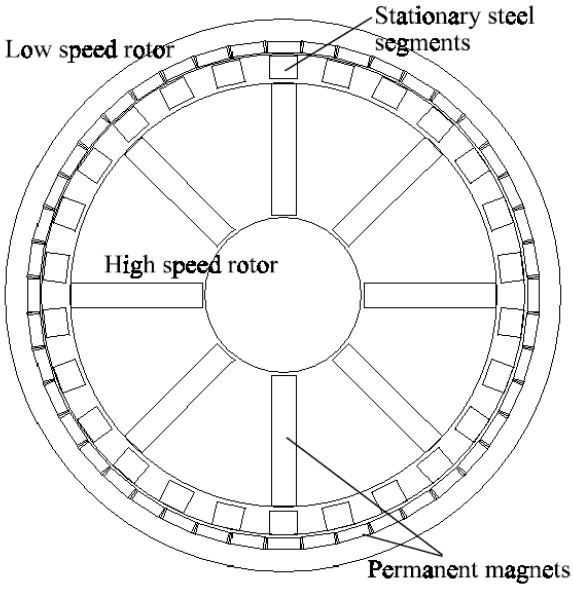

Figure 1.21: Coaxial Magnetic Gear with Spoke-Type High Speed Rotor Magnets (14)

In the same year Razzel and Cullen took out a patent (53) for a compact electrical machine. The machine consisted of a coaxial magnetic gear integrated into a PM generator (see Figure 1.22). The combined machine then became a high torque low speed machine.

Atallah *et al*. 2005 published a paper (16) on a linear magnetic gear. The gear operated on the same principle as the coaxial magnetic gear. There were three parts that moved relative to each other: two PM armatures connected to steel yokes and one flux-modulator core (see Figure 1.23). The flux-modulator core modulated the magnetic flux between the inner and outer PM armatures, so that the PM yokes interacted with the correct number of poles (correct space harmonics). The proposed linear gear was simulated and the results showed that a thrust force of 1.7 MN/m^3 could be obtained. It was also shown that a linear magnetic gear combined with a linear electrical machine could obtain a high force density, even with a relatively low gear ratio.

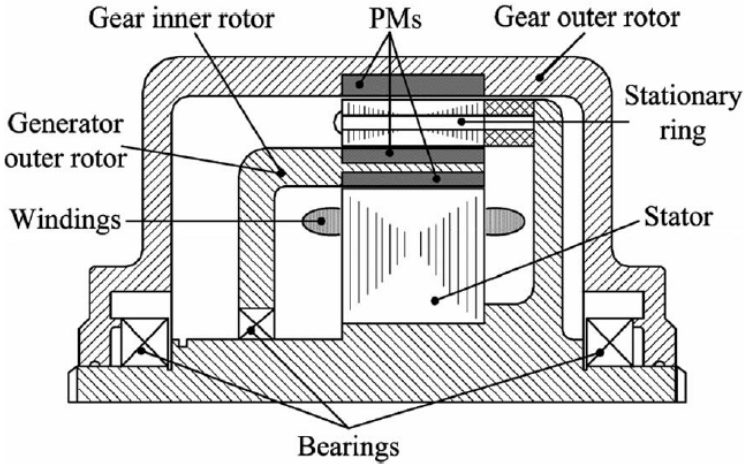

Figure 1.22: Magnetic Geared PM Generator, (picture from (15))

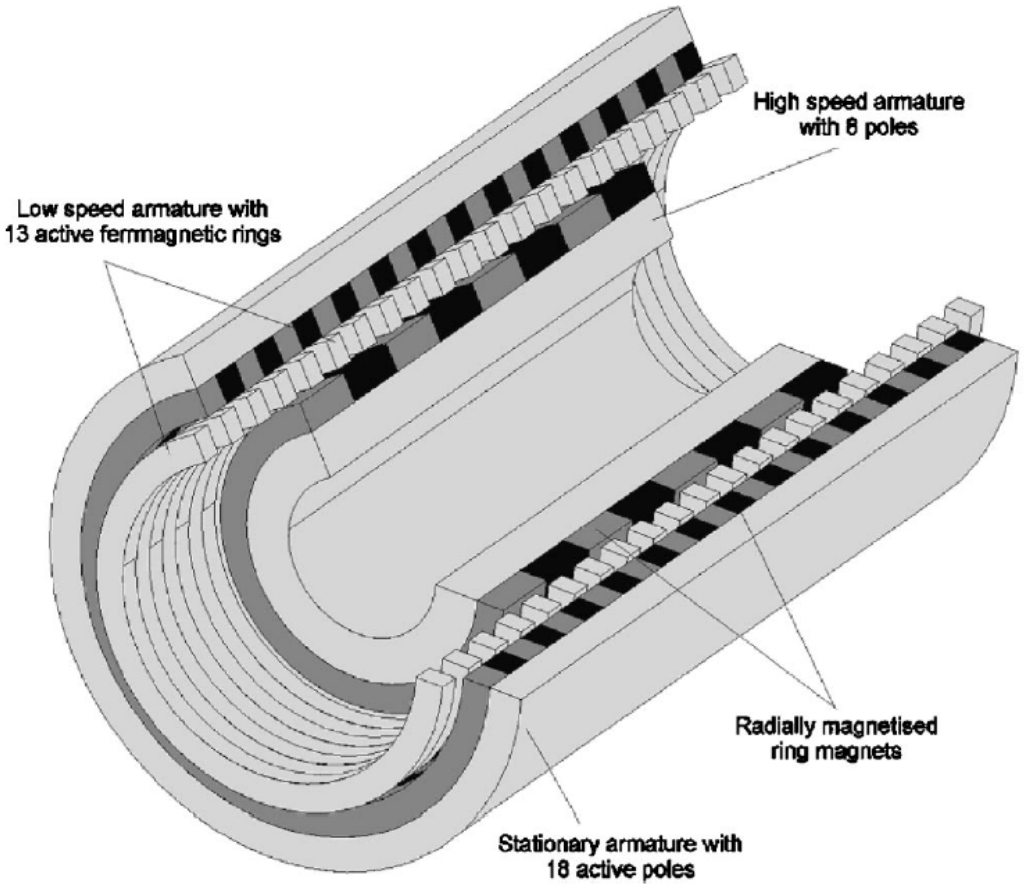

Figure 1.23: Linear Magnetic Gear (16)

In 2006 a paper (17) was published about an axial field magnetic gear operating on the same principle as described in Atallah's coaxial and linear magnetic gear, (13; 16) (an illustration of the proposed gear can be seen in Figure 1.24). The gear was particularly suitable for applications which required isolation between input and output shafts, for example pumps. It was concluded that a torque density in excess of 70 kNm/m^3 could be reached and that the axial forces which were exerted on the low- and high-speed rotors, were relatively low. Typically a single row angular contact ball bearing would be more than adequate to handle the axial forces. For example, the maximum axial force for the prototype reached just under 3 kN. However, an angular contact ball bearing for a 20 mm shaft diameter can withstand 10 kN.

In 2007 an interesting paper, (54) surfaced, in which the experimental results for the application of a coaxial magnetic gearbox being used in a contra-rotating tidal turbine were described. The contra-rotating tidal turbine comprised of two sets of blades; the upstream blade rotated in a clockwise direction whilst the downstream blade rotated in an anti-clockwise direction. The upstream blade was connected to the low speed outer rotor and the downstream blade was connected to the flux-modulator of the coaxial magnetic gear. The coaxial magnetic gearbox combined the output of both contra-rotating shafts into a single high speed rotating shaft (inner rotor). A complete prototype with the blades needed to be constructed in order to test the system.

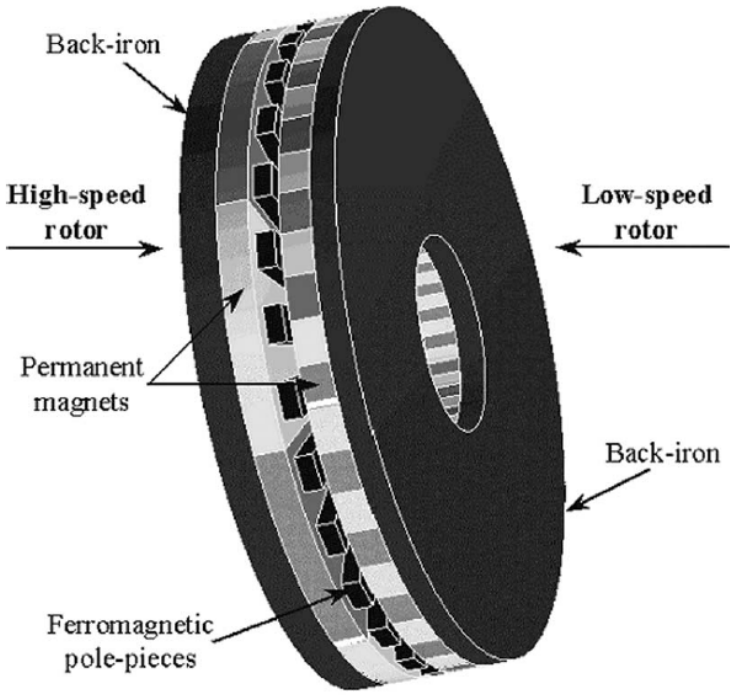

Figure 1.24: Axial-Flux Magnetic Gear, (17)

Rens et al. (18) 2007 proposed a harmonic magnetic gear. The operating principle of the proposed gear was similar to that of a mechanical harmonic gear (see Figure 1.25). The operating principle of a harmonic gear was that a high speed input on the wave generator caused gear teeth on the flexible-spline (input) to engage with internal teeth on the circular-spline (output). Since the flexible-spline had two teeth fewer than the circular-spline, each revolution of the input caused a 2-tooth displacement of the output. (Figure 1.25B shows a magnetic version of the harmonic gear). For the magnetic harmonic gear the high speed rotor deformed the flexible low speed rotor which rotated within the rigid outer stator. The time varying sinusoidal variation of the air gap length modulated the field produced by the magnets on the low speed rotor and resulted in a dominant asynchronous space harmonic field which interacted with the magnets on the stator to facilitate torque transmission and the magnetic gear action.

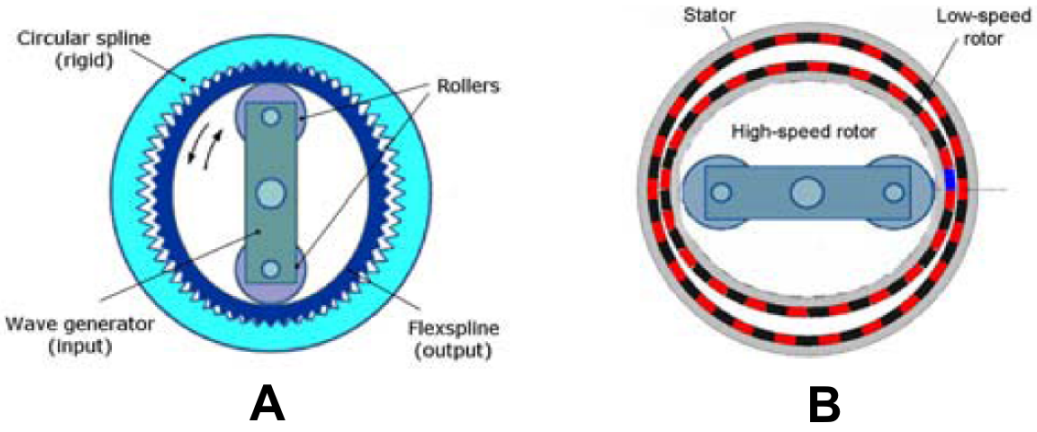

Figure 1.25: A) Mechanical Harmonic Gear. B) Magnetic Harmonic Gear

The harmonic gear was further complicated by the need for a flexible permanent magnet low speed rotor assembly. One way to simplify the design and make it more practical, was to use a rigid low speed rotor which was driven eccentrically by the high speed rotor so that a single cyclic variation of the air gap resulted between the permanent magnets on the low speed rotor and the stator (see Figure 1.26). This version was far better than the flexible version (as can be seen in 1.25B) but not without complexities.

The problem with this design is that the rigid low speed rotor rotated eccentrically; the output shaft needed to be connected with this eccentrically moving rigid low speed rotor and this could only be done with a flexible coupling or with two bearings one inside the other but with the same eccentric distance apart. (Figure 1.27 shows the cycloidal bearings with the eccentric distance between the bearings). Another problem associated with the eccentric distance is that an unbalanced magnetic force was generated because one side of the high speed rotor was always closer to the low speed rotor (the varying air gap).

Rens *et al.* 2007, (18) proposed a dual stage magnetic harmonic gear (see Figure 1.28). This eliminated the need for a flexible coupling and further increased the gear ratio. It was shown in the paper that a dual stage harmonic gearbox could obtain very high gear ratios. Torque densities of up to 110 kNm/m^3 could be achieved and the transmitted torque exhibited no torque ripple. Finally the dual stage harmonic magnetic gear exhibited a higher gear ratio than the product of the ratios of the individual stages.

Figure 1.26: More Practical Harmonic Magnetic Gear

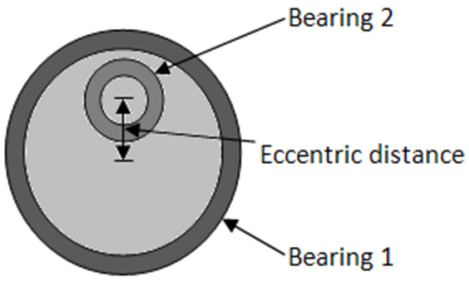

Figure 1.27: Cycloidal Bearing

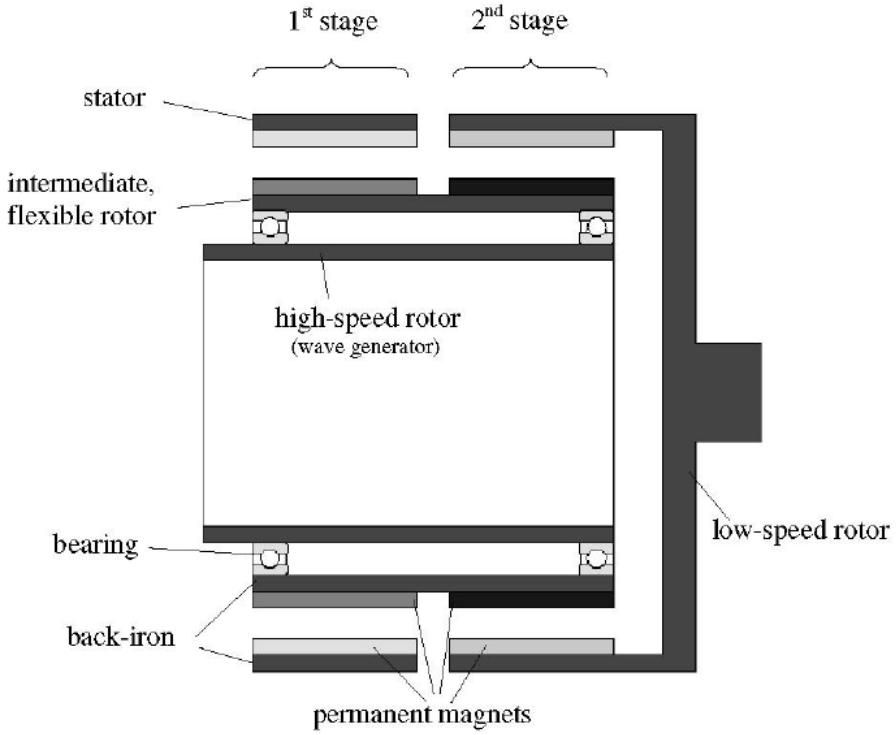

Figure 1.28: Dual Stage Harmonic Magnetic Gear, (18)

In 2008 Rens wrote another paper, (55), very similar to the one mentioned above and again in 2010, (56).

In 2008 Jorgensen *et al.* wrote a paper, (57), on a harmonic gear with two identical stages. The second stage was placed so that the unbalanced force of the varying air-gap of the first stage was cancelled by the unbalanced force of the second stage. The problem with this arrangement was that the cycloid motion of the two stages needed to be transferred from the one to the other stage and to the output shaft. The problem was solved by employing cycloidal bearings (see Figure 1.27). However, 12 bearings were needed to solve the cycloid motion, which in turn caused extra losses. Despite all the extra bearings the proposed gearbox succeeded in reaching an efficiency of over 90%.

Chau et al. published a paper, (19) about a new integrated design in 2007. The paper described a PM DC brushless motor integrated into a coaxial magnetic gear. The machine was similar to Razzel's design of 2004 (see Figure 1.29). The combined system offered the low speed capabilities of magnetic gears and the high speed requirements for compact motor design, which gave the combined system high torque density and high efficiency at relatively low speeds. The machine was proposed for electrical vehicles. The proposed motor had fractional slot windings which decreased the cogging torque. The motor without the gearbox had a maximum output torque of 15 Nm, which was insufficient to launch the vehicle. With the gearbox the output torque was increased to 103 Nm, almost 7 times larger, which was sufficient to launch the vehicle.

In 2008 two more papers, (58; 59), were written on the design process described above. Jian *et al.* (60) built a 500 W prototype of the proposed machine. Both the static and dynamic characteristics of

the motor have been studied by time-stepping finite element method and Matlab/Simulink. Both the simulation results and the experimental results verified the validity of the proposed motor.

In 2009 Jian *et al.* (15) proposed the same configuration for use in wind turbine applications. The combined system was ideal for wind power generation. The proposed machine was then compared to a direct drive and a planetary geared PM brushless machines with identical electrical specifications. The proposed topology was of smaller size and lighter weight than both machines, with also lower material cost than the direct driven one.

Hafla *et al.* 2007 wrote a paper, (61), on the efficient design analysis of a coaxial magnetic gear on a high performance computer. The emphasis of this paper was on an efficient analysis of a magnetic gear with an integral equation method. For an accurate analysis of a coaxial magnetic gear a non-linear three dimensional analysis was necessary. The analysis required meshing of all the components including the small air-gaps. By using a fast and efficient matrix compression technique and parallelisation the meshing of the air-gaps became unnecessary and this resulted in accurate results along with acceptable computational costs. In the paper there was a description of full numerical analysis of a magnetic gear including saturation effects and the three-dimensional structure with integral equation method and how it could be implemented with parallelisation, which was necessary for the efficient use of modern computers.

It could be beneficial to realise variable gear ratio magnetic gears. However this is difficult to achieve with coaxial magnetic gears since the number of poles determines the gear ratio and not the strength of the PMs. Graham's patent, (62), described a coaxial magnetic gear where electromagnets (14) were placed in-between every modulation piece (see Figure 1.30). The advantage of adding electromagnets was that the modulation between the inner- and outer-rotor would be affected by switching the electro-

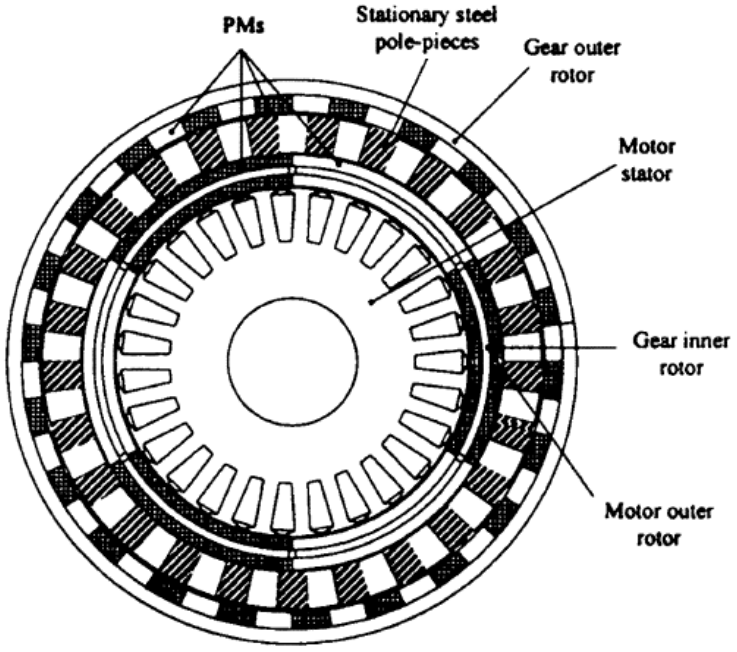

Figure 1.29: Magnetic Geared PM Machine (with Internal Stator), (19)

magnets on or off. Thus more gear ratios could be obtained by controlling the number of electromagnets that were on or off at a specific time. The patent described the layout of the proposed gear with variable gear ratios, however efficiency and performance were not mentioned.

In 2007 Atallah *et al.*, (63), patented a MG integrated into a brushless PM machine, which they called a PSEUDO machine. The machine was very similar to Razzel's US patent of 2004, (53).

In the same year Atallah were granted another international patent, (64), for a harmonic magnetic gear, similar to the one described in a previous paper (18). In 2008 he wrote two more papers about the PSEUDO drives, (65; 66). In both papers the operating principle of magnetically geared brushless machines were described. In both papers it was concluded that the machines could reach torque densities in excess of 60 kNm/m^3 and that the machines had a power factor of 0.9 or higher.

In 2008 Wang *et al.* (20) proposed a simplified version of Chau's (19) design of 2007. The proposed machine had no inner rotor (see Figure 1.31). The machine was called a flux modulated permanent magnet machine. The machine operated in the same manner as a coaxial magnetic gear, however the high speed rotary field was produced with an armature rather than by magnets. In 2009 he wrote a similar paper, (67). In this paper they described the topology and its operating principle. Some techniques were employed to optimize and improve the motor performance, while the validity of the proposed techniques were verified with finite-element analysis. Moreover, an alternative operating condition was proposed and analysed. This was where the outer rotor was kept stationary and the flux-modulator was rotated. The proposed operating principle further decreased the motor speed, while increasing the output torque.

Haung *et al.* 2008 wrote a detailed paper, (68), on a magnetic planetary gear (an illustration can be seen in Figure 1.32). The gear arrangement had a sun, planets and a ring-gear very similar to conventional mechanical planetary gears. The difference was that every tooth was replaced with a PM. The maximum torque could be increased by increasing the number of planets, but by increasing the number

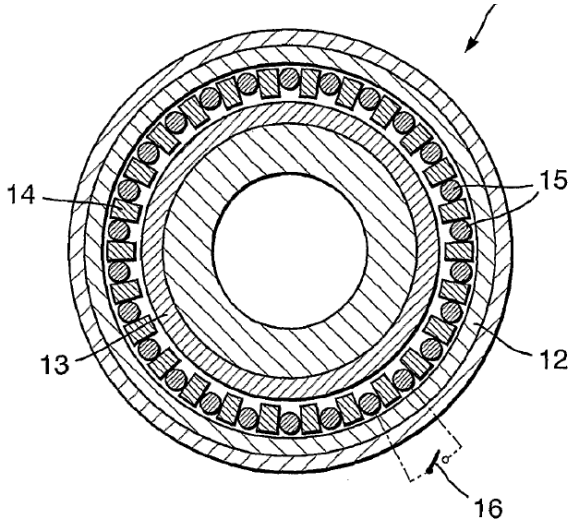

Figure 1.30: Coaxial Magnetic Gear with Electromagnets to Control Gear Ratios

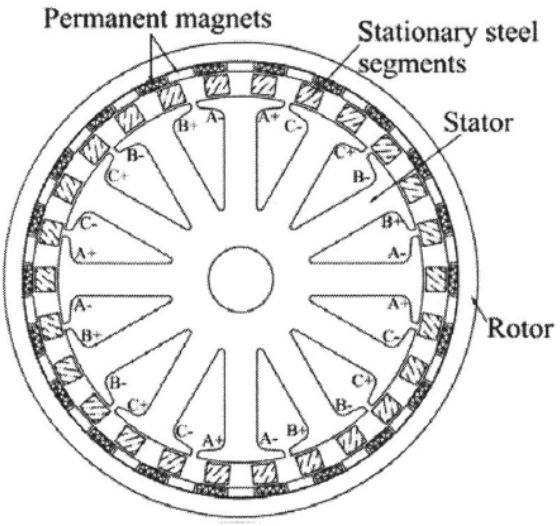

Figure 1.31: Magnetic Geared PM Brushless Machine (no Inner Rotor), (20)

of planets the cogging torque would also be increased. The constructed gearbox exhibited a maximum torque density of 100 kNm/m^3.

Reinap and Marquez published a paper (69) that focused on the design of a linear magnetic gear. The main purpose of the project was to gain analysis skills as well as practical experience of dealing with electromagnetic design for electrical engineering education. In the paper the whole design process was described and an example was given, which makes it ideal for a student with minimal experience in magnetic gears and electromagnetic design.

Davey *et al.* wrote a general paper (70) on magnetic gears in 2008. The paper described the mainstream magnetic gearboxes and focused on the harmonic magnetic gears.

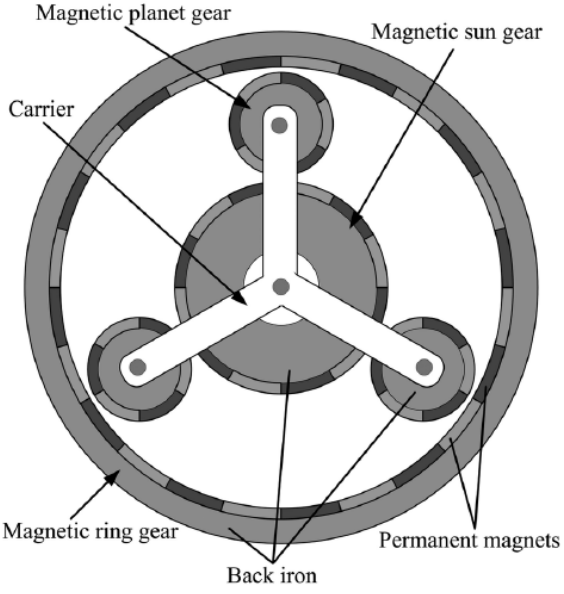

Figure 1.32: Magnetic Planetary Gear

Jong *et al.* rearranged the coaxial magnetic gear in his paper, (71), of 2008. The proposed gear had the same components as a coaxial magnetic gear, except that both rotors were internal (see Figure 1.33). The proposed configuration reduced the external diameter of the gear and simplified the mechanical design. The placing of the shafts and supporting bearings had to be considered carefully, so as not to cause unwanted eddy current losses. The paper included an interesting sizing procedure where the influence of the different part sizes was compared in order to determine an optimum design. The configuration could be ideal in applications where the layout is desirable.

In 2009 Jian *et al.* wrote a paper, (72), in which a new analytical approach was proposed to calculate the magnetic field distribution in coaxial magnetic gears. A set of partial differential equations in terms of scalar magnetic potential was used to describe the field behaviour, and the solution was determined by considering the boundary constraints. The accuracy of the proposed approach was verified by comparing the field distribution results with those obtained from the finite element method.

In the same year he wrote another paper, (73), in which two coaxial magnetic gears were compared with each other one with radially magnetised PM's and the other with halbach magnetised PM's. Analysis showed that the halbach magnetised PM's could offer higher pull-out torque, lower torque ripple and lower iron losses than the radially magnetised PM's.

Jian *et al.* then wrote a paper, (74), about the integrated machine with halbach magnetised PM's. The advantage was that the PM motor field and the magnetic gear field were decoupled. In addition, the halbach arrays could enhance the effective harmonic components as well as suppress the unwanted harmonic components of the magnetic field. Other advantages of the halbach array was that maximum torque was increased and iron losses in the outer rotor was decreased. Simulation results based on the time-stepping finite element method were given to verify the validity of the proposal.

Liu et al. wrote a paper, (75), about the coaxial magnetic gear in 2009. In the paper a new topology where the PM's were buried into the iron core of the outer rotor was described. Rather than embedding the alien-polarity PM's into the outer-rotor iron core (as shown in Figure 1.34a) the proposed configuration inserted the PMs with the same polarity into the iron core (as shown in Figure 1.34b). The PM flux

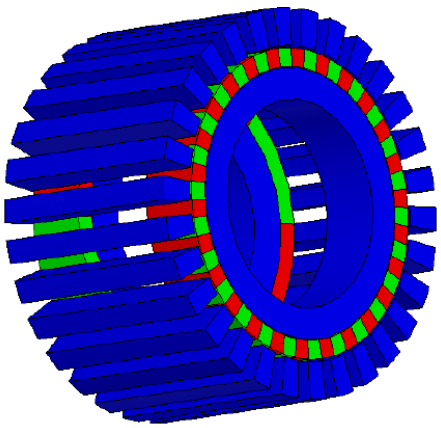

Figure 1.33: Internal High- and Low-Speed Rotors

flowed in the core bridges equivalently from the alien poles, thus creating a distributed magnetic field with the same number of pole pairs. This improved the mechanical integrity and PM material could be saved while the torque density was maintained. The proposed configuration reduced the magnetic material by 16.5% while decreasing the pull-out torque by only 5.3% for the prototype build.

Frank *et al.* wrote two papers in 2009, (76; 77), in which different applications of coaxial magnetic gears were described. In the first one the use of coaxial magnetic gears for ship propulsion was discussed and in the next one wind power. In both papers the performance of the gear, especially the cogging torque at different gearing ratios was described.

In 2009 Rasmussen *et al.* published a paper, (78), on a motor integrated magnetic gear similar to the design in (19). In the previous integrated designs the end windings of the stators were not taken into consideration in the calculation of the torque density. In the proposed design the motor and the gear were carefully designed so that the end windings would not take up extra space. In the paper a scaling process was described in order to determine an optimised gear with the least amount of material and cost. The proposed machine had a maximum torque density of 130 kNm/m^3.

Fu et al. in 2010, (79), compared the performance of a flux-modulated PM machine (see Figure 1.31) with a magnetically geared PM machine (see Figure 1.29), a traditional PM machine and with a fractional slot PM machine using magnetic field FEA. When comparing the four machines it was necessary to make sure that all motors had the same outside radius and axial length. The motors had the same amount and type of magnetic materials and the same grade of copper and iron materials. The motors also had the same temperature rise at full load. It was concluded that the magnetically-geared motor delivered very large torque at low speeds. The disadvantage was that the machine had too many rotational parts. Compared to the conventional machines the FM-machine had similar torque density. However, the FM-machine had a smaller number of slots and ventilation was better because of the gaps between the modulation pieces. The conventional PM motor had too many slots, its slot area could not be utilized efficiently, the end windings were too long and it also had very large cogging torque. The fractional-slot multi-pole motor had a small number of slots and short end windings. Its output torque was smaller than that of the motor with conventional windings and it had small cogging torque.

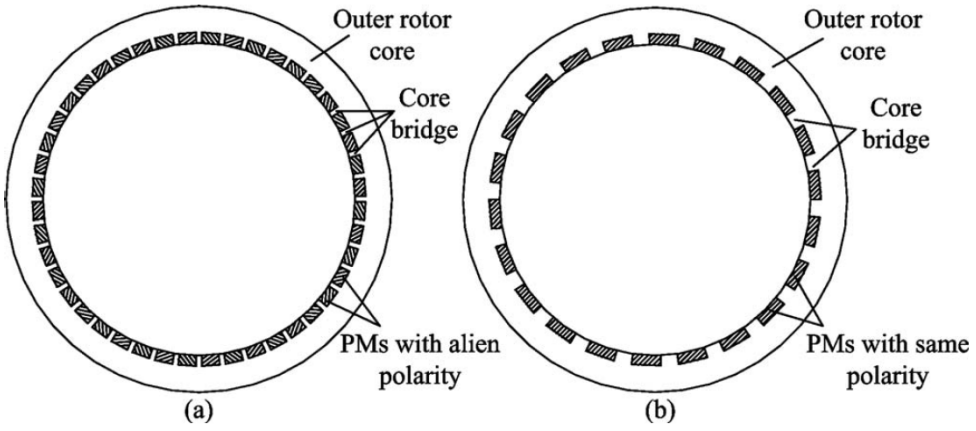

Figure 1.34: Interior PM Rotor Configurations. a) Traditional. b) Proposed

1.2.1 Conclusion Drawn from Magnetic Gear History

From the history section it can be observed that magnetic gears are very versatile, MGs can basically be configured in any arrangement that traditional mechanical gears can be configured into. However, MGs offer significant advantages over traditional mechanical gears. Typically, mechanical gears transfer torque with only one to three gear teeth at any given instant, where MG may transfer torque with all of their permanent magnets at any given instant. Thus, MG may occupy a smaller volume and still transfer the same amount of power when compared to mechanical gears.

They offer other advantages as well, such as:

- Power transfer with no contact between parts.
- High gear ratios at a single stage.
- Lubricant free operation.
- Inherent overload protection.
- High torque densities.
- Potential for high efficiency.
- Little or no maintenance.

Two main MG configurations were identified which may offer the most advantages, namely: The coaxial magnetic gear of (2; 27; 8) and the harmonic magnetic gear of (18). Of theses two configurations the coaxial MG stands out the most. The harmonic MG have too many complexities that still need to be addressed, such as the unbalanced force of the eccentric rotation. Therefore it was decided that the coaxial magnetic gear would be further investigated.

1.3 Problem Statement

The demand for power generation through conversion of wind energy has escalated as the result of the international demand for alternative energy sources. However, the traditional gearboxes have proven unreliable and difficult to maintain (24).

In this project a magnetically geared permanent magnet generator is proposed and evaluated in an attempt to address the major problems of mechanical gears in the wind energy industry.

From the literature reviewed it is observed that the coaxial magnetic gear in the axial-flux topology has never been constructed and experimentally evaluated. Since all of the main components are observable in the axial-flux topology, the experience gained from experimental evaluation could greatly contribute to the progress in MG development.

1.3.1 Problems to Solve

The magnetically geared axial-flux topology had to be designed, manufactured, constructed and experimentally evaluated.

This study aims to address these foremost challenges:

- Selection of suitable machine topology.
- Suitable design specifications for wind energy conversion applications.
- Formulation of an effective design approach.
- Optimisation of a prototype machine with the best performance, against predefined constraints.
- Mechanical design aspects of the prototype machine.
- Manufacture and construction of a prototype magnetically geared permanent magnet generator.
- Experimental evaluation of the prototype.
- Evaluation of the difference between coupled and decoupled configurations.
- Identification of problem areas for further MG development.

1.3.2 Approach to Problem

Firstly, magnetic gear literature is reviewed to determine the progress and challenges in MG development. Secondly the theory of magnetic gears is further investigated to gain extra understanding.

Based on these a suitable machine topology and configuration, which will be most suitable for purposes of this study is chosen. The design specifications for a prototype machine are chosen for application in wind energy conversion. The prototype machine is then electromagnetically optimised against predefined goals. The mechanical design is analysed to ensure that the prototype machine is mechanically sound. With the design in place, the components can be manufactured and the prototype machine can be constructed. After the prototype has been constructed it can be experimentally evaluated. Finally, the results are examined to identify challenge areas for future MG development.

1.4 Thesis Layout

Chapter 1: Literature Review

A brief historic review is given, to identify the magnetic gear configuration with the most advantages for purposes of this study. Contemporary problems are identified and possible solutions are suggested.

Chapter 2: Theory of Magnetic Geared Permanent Magnet Machines

The theory of magnetic gearing, the determination of the gear ratio and the calculation of the parameters of the equivalent circuit for a magnetically geared PM machine are presented.

Chapter 3: Design Specifications

Based on the specific applications the design specifications of the prototype magnetically geared permanent magnet generator are considered.

Chapter 4: Design and Optimisation

The electromagnetic design, optimisation procedure and results for the prototype machine are presented. Relevant results are discussed

Chapter 5: Mechanical Design and Construction

The mechanical design and analysis of the prototype is given in this chapter, in which the forces, namely the electrical interaction, the mechanical interaction and the component properties such as weight are considered to investigate the strength and reliability of the prototype machine.

Chapter 6: Experimental Evaluation

The prototype machine are experimentally evaluated and the measured results are discussed.

Chapter 7: Conclusion and Recommendations

Some conclusions are drawn and recommendations are made.

Appendix A: Graphs to Assist in Choosing Magnetically Geared Parameters

Graphs to assist in choosing magnetically geared machine parameters, by sweeping through parameter combinations.

Appendix B: Flux-Modulator Assembly Process

Photos of the flux-modulator assembly process.

Appendix C: New Improved Low Speed Rotor Design

Alternative low speed rotor design, which solves the vibration concerns of the low speed rotor.

CHAPTER 2

THEORY OF MAGNETICALLY GEARED PERMANENT MAGNET MACHINES

2.1 Introduction

In this chapter the theory of magnetic gearing, the determination of the gear ratio and the calculation of the parameters of the equivalent circuit for a magnetically geared PM machine are presented. With the equivalent circuit parameters known the performance of the machine can be calculated. In the first section of this chapter magnetic gear theory will be described and in the second section permanent magnet generator theory.

2.2 The Operational Principle of Magnetic Gearing

Fundamental to the operation of a coaxial magnetic gear are the magnetic fields produced by the permanent magnets on either the high- or low-speed rotors by the steel pole pieces (flux-modulation pieces), which result in space harmonics having the same number of poles as the related magnet rotor.

In Figure 2.1 a generic layout of a radial field magnetic gear is presented. The flux distribution in radial direction at a radial distance r and angle θ produced by either permanent magnet rotor, without taking into consideration the flux-modulator, can be written in the following form (71; 80):

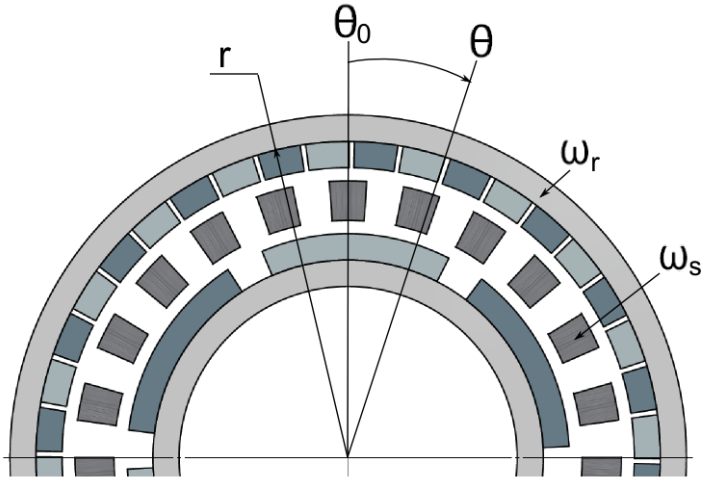

Figure 2.1: Magnetic Gearing Parameters

$$B_{rA}(r,\theta) = \sum_{m=1,3,5,\ldots} b_{rm}(r)cos(mp(\theta - \omega_r t) + mp\theta_0) \tag{2.1}$$

and the modulation function can be written as:

$$B_{rB}(r,\theta) = \lambda_{r0}(r) + \sum_{j=1,2,3,\ldots} \lambda_{rj}(r)cos(jn_s(\theta - \omega_s t)) \tag{2.2}$$

The resultant field components for the radial component are:

$$B_r(r,\theta) = B_{rA}(r,\theta) \times B_{rB}(r,\theta) \tag{2.3}$$

Similarly for the circumferential flux distribution, we have

$$B_{\theta A}(r,\theta) = \sum_{m=1,3,5,\ldots} b_{\theta m}(r)sin(mp(\theta - \omega_r t) + mp\theta_0) \tag{2.4}$$

$$B_{\theta B}(r,\theta) = \lambda_{r0}(r) + \sum_{j=1,2,3,\ldots} \lambda_{\theta j}(r)sin(jn_s(\theta - \omega_s t)) \tag{2.5}$$

$$B_\theta(r,\theta) = B_{\theta A}(r,\theta) \times B_{\theta B}(r,\theta) \tag{2.6}$$

where p is the number of pole-pairs on a permanent magnet rotor, n_s is the number of modulation pieces, ω_r is the rotational velocity of the permanent magnet rotor and ω_s is the rotational velocity of the flux-modulator. The Fourier coefficients for the radial and circumferential flux density distribution without the flux-modulation pieces are; b_{rm} and $b_{\theta m}$, respectively. The Fourier coefficients for the radial and circumferential components of the flux density distribution resulting from the introduction of the flux-modulation pieces are λ_{rj} and $\lambda_{\theta j}$, respectively.

On substitution of 2.1 and 2.2, Equation 2.3 can be further expressed as:

$$\begin{aligned} B_r(r,\theta) = {} & \lambda_{r0} \sum_{j=1,3,5,\ldots} b_r m(r)cos(mp(\theta - \omega_r t) + mp\theta_0) \\ & + \frac{1}{2} \sum_{m=1,3,5,\ldots} \sum_{j=1,2,3,\ldots} \lambda_{rj}(r)b_{rm}cos\left((mp + jn_s)\left(\theta - \frac{mp\omega_r + jn_s\omega_s}{mp + jn_s}t\right) + mp\theta_0\right) \\ & + \frac{1}{2} \sum_{m=1,3,5,\ldots} \sum_{j=1,2,3,\ldots} \lambda_{rj}(r)b_{rm}cos\left((mp - jn_s)\left(\theta - \frac{mp\omega_r - jn_s\omega_s}{mp - jn_s}t\right) + mp\theta_0\right) \end{aligned} \tag{2.7}$$

Similarly on substitution of Equation 2.4 and 2.5, Equation 2.6 becomes:

$$\begin{aligned} B_\theta(r,\theta) &= \lambda_{\theta_0} \sum_{m=1,3,5,\dots} b_{\theta m}(r) sin(mp(\theta - \omega_r t) + mp\theta_0) \\ &+ \frac{1}{2} \sum_{m=1,3,5,\dots} \sum_{j=1,2,3,\dots} \lambda_{rj}(r) b_{rm} sin\left((mp + jn_s)\left(\theta - \frac{mp\omega_r + jn_s\omega_s}{mp + jn_s}t\right) + mp\theta_0\right) \\ &+ \frac{1}{2} \sum_{m=1,3,5,\dots} \sum_{j=1,2,3,\dots} \lambda_{rj}(r) b_{rm} sin\left((mp - jn_s)\left(\theta - \frac{mp\omega_r - jn_s\omega_s}{mp - jn_s}t\right) + mp\theta_0\right) \end{aligned} \tag{2.8}$$

From Equation 2.7 and 2.8, it can be seen that the number of pole pairs in the space harmonic flux density distribution produced by either the high- or low-speed rotor is given by:

$$\begin{aligned} p_{m,k} &= |mp + kn_s| \\ m &= 1, 3, 5, ..., \infty \\ k &= 0, \pm 1, \pm 2, \pm 3, ..., \pm\infty \end{aligned} \tag{2.9}$$

The rotational velocity of the flux density space harmonic is given by:

$$\omega_{m,k} = \frac{mp}{mp + kn_s}\omega_r + \frac{kn_s}{mp + kn_s}\omega_s \tag{2.10}$$

From Equation 2.10, it can be seen that the velocity of the space harmonics due to the introduction of the flux-modulator ($k \neq 0$), is different to the velocity of the rotor which carries the permanent magnets. Therefore, in order to transmit torque at a different speed (change the gear ratio), the number of pole-pairs of the other permanent magnet rotor must be equal to the number of pole-pairs of a space harmonic for which $k \neq 0$. Since the combination $m = 1$ and $k = -1$ results in the highest asynchronous space harmonic, the number of pole-pairs of the other rotor must be equal to $(n_s - p)$. The gear ratio when the flux-modulator is held stationary ($\omega_s = 0$), is then given by;

$$G_r = \frac{n_s - p_H}{p_H} \tag{2.11}$$

or

$$G_r = \frac{p_L}{p_H} \tag{2.12}$$

which gives;

$$n_s = p_H + p_L \tag{2.13}$$

where p_H and p_L are the number of pole-pairs on the high- and low-speed rotors, respectively.

Sometimes, it may be preferred to keep the outer rotor stationary ($\omega_r = 0$) as it may simplify the overall mechanical design. The torque will then be transmitted to the flux-modulator instead of the outer rotor, the gear ratio then becomes:

$$G_r = \frac{n_s}{p_H} \tag{2.14}$$

2.3 The Equivalent Circuit of a Magnetically Geared Permanent Magnet Generator

There are two different configurations for magnetically geared PM machines, in which the magnetic circuits of the gear part and the machine part could be decoupled and coupled, respectively (as shown in Figure 2.2). This is important, since the permanent magnets on the low-speed rotor for the coupled system, contribute to the total flux-linkage in the stator. In the decoupled system however, the low-speed rotor is magnetically decoupled to the generator part of the machine, thus the PMs on the low-speed rotor do not contribute to the total flux-linkage that the stator will interact with.

To calculate the performance of the MGAFG, it is essential to consider the equivalent circuits of the machine.

2.3.1 Magnetically Decoupled MGPMG

For a magnetically decoupled MGPMG the per phase electrical equivalent circuit of the PMG is shown in Figure 2.3(a). In this circuit, E_1 is the electromotive force (EMF) induced in the stator windings due to the fundamental air-gap PM flux-linkages of the high-speed rotor, L_s is the stator inductance, R_s is the stator resistance and I_s is the stator current. The shunt resistance R_c is the core loss resistance.

With the 2D finite element method the total stator flux-linkage can be calculated, however the end-winding flux-linkage is not calculated in 2D FEM. Thus the stator inductance L_s is split into two terms, namely the main inductance L_m and the endwinding leakage inductance L_e, as shown in Figure 2.3 (b). In the circuit R_c may be shifted to the left of L_e as an approximation. The approximation allows that

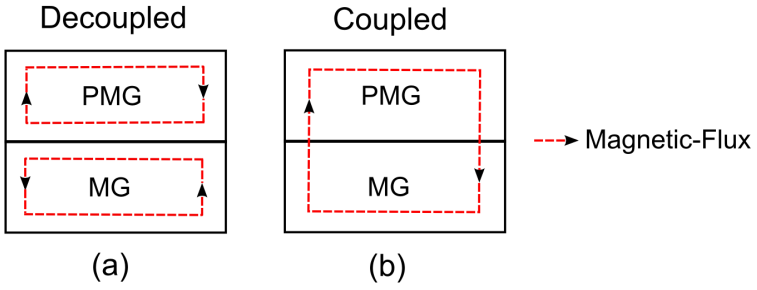

Figure 2.2: Magnetic Geared PM Machine with (a) Magnetically Decoupled and (b) Magnetically Coupled Topologies

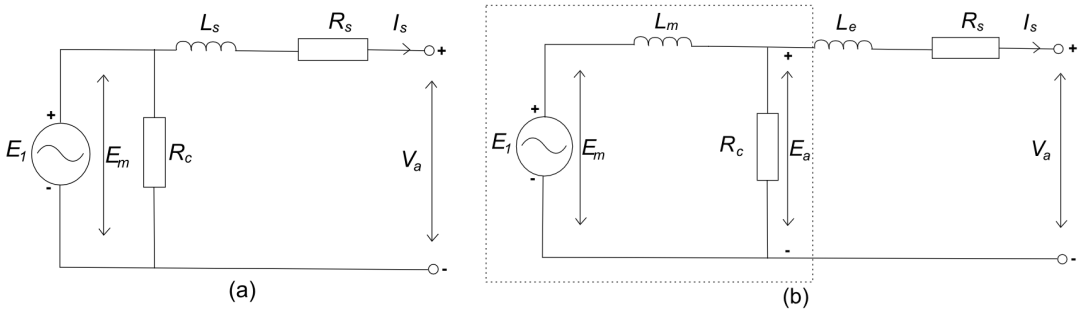

Figure 2.3: Per Phase Equivalent Circuits

the left side of the equivalent circuit marked by the dashed lines can be accurately calculated by directly using finite element method.

In this section the rest of the electrical parameters that are not accounted for in the FEM analysis will be calculated. The following equations and performance calculation approach is inspired from (81; 15). Thus, all of the parameters on the right side of Figure 2.3 (b) will be calculated. The corresponding steady state $d-$ and q-axis equivalent circuits are shown in Figure 2.4. The flux-linkages λ_d and λ_q are the d- and q-axis stator flux-linkage (λ_{dq0}) components.

Park's transformation K_p is used to transform the equivalent circuit in the abc reference frame to the equivalent circuits in the dq reference frame:

$$K_p = 2/3 \begin{bmatrix} cos\theta & cos(\theta - 2\pi/3) & cos(\theta + 2\pi/3) \\ sin\theta & sin(\theta - 2\pi/3) & sin(\theta + 2\pi/3) \\ 1/2 & 1/2 & 1/2 \end{bmatrix} \tag{2.15}$$

As mentioned, the input of the equivalent circuit are the parameters calculated in the FE analysis, however the input of the FE analysis are the instantaneous three phase currents i_{abc}. The instantaneous three phase currents can be calculated by determining the maximum allowable current-density that the given stator coils can handle. Thus, the amplitude of the current space phasor I can be calculated from

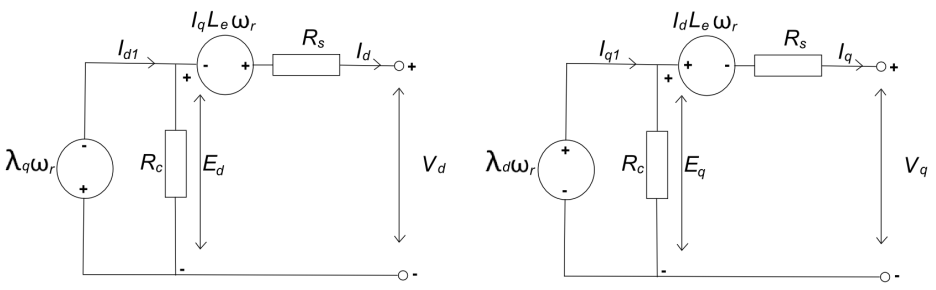

Figure 2.4: Decoupled dq Equivalent Circuits

the input current density J with the following formula

$$I = \sqrt{2} J A_{cu} n_a / z \tag{2.16}$$

where A_{cu} is the available area for placing conductors (copper) in mm^2, n_a is the number of parallel circuits and z is the number of turns per coil. Equation 2.17 can be used to calculate the available conductor area A_{cu}.

$$A_{cu} = A_c * k_f \tag{2.17}$$

where A_c is the coil cross-section area and k_f is the filling factor, which is calculated with the following equation

$$k_f = A_{con} z n_{strands} / A_c \tag{2.18}$$

In the equation A_{con} is the area of a single conductor and $n_{strands}$ is the number of strands per conductor. The instantaneous three-phase currents can then be calculated and used as inputs to the FE analysis and the three phase flux-linkages λ_{abc} will be the output of the FE analysis. With the three phase flux-linkages and Park's transformation the dq flux-linkages λ_{dq0} can be determined

$$[\lambda_{dq0}] = [K_p][\lambda_{abc}] \tag{2.19}$$

From this the speed voltages E_d and E_q of the equivalent circuit can be determined.

$$E_d = -\lambda_q \omega_r \quad E_q = \lambda_d \omega_r \tag{2.20}$$

Next the core-loss resistance R_c needs to be calculated, R_c is calculated with the rms value of the phase EMF, E_a, and the total core losses P_c. The rms value of the phase EMF, E_a, is calculated with the following equation

$$E_a = \sqrt{\frac{E_d^2 + E_q^2}{2}} \tag{2.21}$$

and the total core losses P_c are determined in the FEM analysis. Thus, R_c is calculated with the following equation:

$$R_c = \frac{3E_a^2}{P_c} \tag{2.22}$$

The next step is to calculate the dq currents i_{dq0}. The dq currents can be calculated with Park's transformation and the instantaneous three phase currents i_{abc} as determined in Equation **??**.

$$[i_{dq0}] = [K_p][i_{abc}] \tag{2.23}$$

From the known dq current components (I_d and I_q), the calculated dq speed voltages (E_d and E_q) and the core loss resistance R_c, the $dq1$ current components (I_{d1} and I_{q1}) and the current amplitude I_{s1} can be calculated:

$$\begin{aligned} I_{d1} &= I_d + E_d/R_c \\ I_{q1} &= I_q + E_q/R_c \\ I_{s1} &= \sqrt{I_{d1}^2 + I_{q1}^2} \end{aligned} \tag{2.24}$$

Next the end-winding inductance per phase is calculated with (82);

$$L_e = \frac{4\mu_o n_{tp}^2 l_e P_{le}}{p q_1} \tag{2.25}$$

where μ_o is the permeability of air ($\mu_o = 4\pi 10e^{-7}$), n_{tp} is the number of turns in series per phase, q_1 is the number of coils per pole per phase and l_e is the end-winding length of a coil. Then the dq inductances are determined from the following equations:

$$L_q = \lambda_q / I_q \tag{2.26}$$

and

$$L_d = L_q \tag{2.27}$$

After this the per phase stator winding resistance can be calculated (81),

$$R_s = \frac{2n_{tp}(l + l_e)}{\sigma_T n_a s_{cu}} \tag{2.28}$$

where l is the active length of a coil, σ_T is the electric conductivity of the wire at temperature T and s_{cu} is the cross section area of the wire. The skin effect has not been taken into account in Equation 2.28. The skin effect is minimal if thin parallel wires are used. With the per phase stator winding resistance (R_s) and the current amplitude (I_{s1}), the total copper losses can be determined:

$$P_{cu} = 3I_{s1}^2 R_s \tag{2.29}$$

The dq terminal voltage components (V_d and V_q) and the voltage amplitude are calculated from:

$$\begin{aligned} V_d &= E_d + L_e I_q w_r - I_d R_s \\ V_q &= E_q + L_e I_d w_r - I_q R_s \\ V_s &= \sqrt{V_d^2 + V_q^2} \end{aligned} \tag{2.30}$$

The steady state torque T_{He} of the high-speed rotor can also be calculated from the equivalent circuit elements, by:

$$T_{He} = \frac{3}{2} p(\lambda_d I_q - \lambda_q I_d) \tag{2.31}$$

With the gear ratio G_r of the magnetic gear known, the steady state torque of high-speed rotor referred to low-speed side can be calculated as:

$$T_{Le} = T_{He} \times G_r \tag{2.32}$$

The next step is to calculate the apparent power S:

$$S = \frac{3}{2} V_s I_s \tag{2.33}$$

Then the power factor is determined from the following equation:

$$P_f = cos[tan^{-1}(\frac{V_d}{V_q}) \pm tan^{-1}(\frac{I_d}{I_q})] \tag{2.34}$$

With the apparent power S and the power factor P_f the output power P_{out} is calculated:

$$P_{out} = S \cdot P_f \tag{2.35}$$

The input power of MGAFG P_{in} is calculated from the output power and the total losses P_{Loss}:

$$P_{in} = P_{out} + P_{Loss} \tag{2.36}$$

where P_{Loss} consists of; the copper losses P_{cu}, the core losses P_c, the losses of the magnetic gear part of the machine P_{gear} and the windage losses $P_{windage}$.

$$P_{Loss} = P_{cu} + P_c + P_{gear} + P_{windage} \tag{2.37}$$

And finally the efficiency η can be calculated;

$$\eta = \frac{P_{out}}{P_{in}} \tag{2.38}$$

Thus, the machine performance can be accurately calculated by simulating the machine in a FE analysis, extracting the results and further processing the machine parameters with the help of the equivalent circuit.

2.3.2 Magnetically Coupled MGPMG

For the coupled system the flux-linkage of the low-speed rotor contribute to the total flux-linkage in the stator. Thus a secondary EMF source E_2 is introduced in the equivalent circuit (see Figure 2.5).

The speed voltage components of Equation 2.20 will thus have another flux-linkage component due to the flux-linkage contribution of the low-speed rotor. Thus the total dq flux-linkages becomes:

$$\lambda_d = \lambda_{dH} + \lambda_{dL} \qquad \lambda_q = \lambda_{qH} + \lambda_{qL} \tag{2.39}$$

where the subscripts $_H$ and $_L$ are the high- and low-speed rotor contributions, respectively. Even though the high- and low-speed rotors rotate at different velocities, the rotational velocity ω_r of the high-speed rotor is still used in Equation 2.20 to calculate the speed voltages, since the flux-modulator modulates the flux component of the low-speed rotor at the same velocity as that of the high-speed rotor's flux component.

The total flux-linkage is however calculated in the FEM analysis, thus the same procedure as described for the decoupled system can be used to calculate the performance of the coupled system.

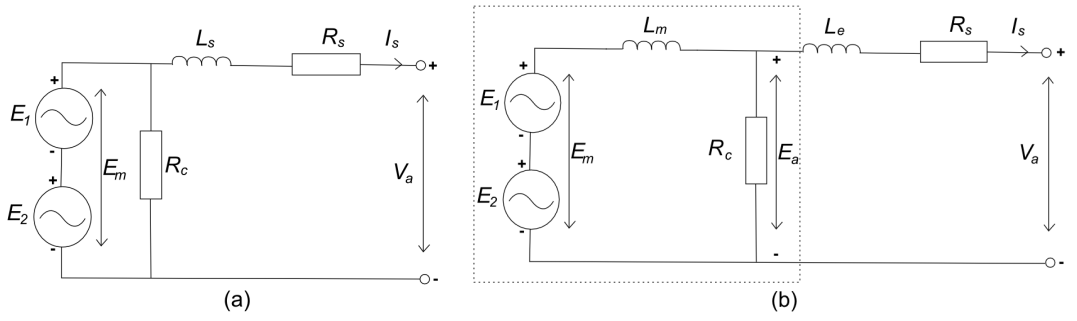

Figure 2.5: Coupled Per Phase Equivalent Circuits

CHAPTER 3

DESIGN SPECIFICATIONS

In this chapter the design specifications of a magnetically geared permanent magnet generator will be considered. The machine specifications greatly rely on the type of application that they will be used for. Thus, in the first section the application that the machine is designed for will be described. With the application known the best machine configuration and topology can be selected, which is explored in the second section. In the last section the determination of the rest of the machine parameters in an attempt to achieve the best machine performance, will be dealt with.

3.1 Design for Wind Power Application

As discussed in Chapter 1, there are many potential applications for magnetically geared electric machines. Amongst others the wind power energy conversion systems is a potential area where MGPMG could find application. Wind energy has been harnessed through the ages and is a major competitor in the current fight for more renewable energy solutions.

Wind is moving air which possesses kinetic energy. Kinetic energy in a fluid is a function of mass and momentum (83). The kinetic energy E_{kw} in wind can be calculated by (84)

$$E_{kw} = \frac{1}{2}\rho_a V_a v_w^2 \tag{3.1}$$

where E_{kw} is measured in Joule, ρ_a is the air density (1.225 kg/m^3 at sea level), V_a is the volume of air interacting with the turbine and v_w is the wind velocity. To calculate the power P_a available in the wind as a function of the blade swept area, A_s, the following equation 3.2 can be used (85).

$$P_a = \frac{1}{2}\rho_a A_s v_w^3 \tag{3.2}$$

From this equation it can be seen that the wind power is proportional to the density of the air, the swept area of the turbine blades and the cube of the wind velocity. Even though the density of air is relatively low the speed of the wind plays a much larger role in the power produced. This is why wind farms is normally situated in coastal regions where the wind velocity is higher.

Furthermore a power coefficient C_p needs to be introduced in Equation 3.2, since not all of the available power can be extracted from the wind. The power production depends on the aerodynamic interaction between the turbine blades and the wind. With a great interaction more power is extracted, however the greater the interaction, the larger the resistance of the blades against the wind. This will cause the air to build up and since the air needs to pass through the turbine blade area, some of the

kinetic energy in the wind should be retained. This brings us to the power coefficient C_p and Equation 3.3.

$$P_a = \frac{1}{2} C_p \rho_a A_s v_w^3 \tag{3.3}$$

The power coefficient C_p describes the fraction of power present in the wind that can be converted into mechanical power by the turbine (85). In an ideal wind turbine the maximum theoretical value of the power coefficient is $C_p = 0.5926$, which is also known as the Betz criterion (85).

From all the above it can be established that wind speed is the major contributor to the power converted from kinetic energy to mechanical power. That is why the design is normally site specific.

For this particular design project,the site and turbine specifications were based on the other research project (86) in the same research group. The site is located at the South African Antarctic Research Base SANAE IV. Research done there is part of an ongoing project to integrate a small wind energy conversion system with the current diesel fuelled power system. However for this project the machine will not be implemented in the field and will only be tested in a laboratory. The experience gained from this project with the specific site conditions, will however be a good indication on whether a magnetically geared machine is feasible for the SANAE IV wind project.

Figure 3.1 shows the power generated versus the input speed of a 15kW wind turbine for various wind speeds at the SANAE IV base.

From (21) and Figure 3.1 the ideal input speed for the given site is 150 rpm. The input speed at the low-speed side of the magnetically geared PM machine would thus be $n_L = 150$ rpm.

3.2 Choosing the Machine Configuration and Topology

Typical small-scale (sub-100 kW) grid-connected wind turbine generators can be configured as shown in Figure 3.2. Figure 3.2(a) represents a doubly-fed induction generator (DFIG) with gearbox (GB) and partial-scale frequency converter. Figure 3.2(b) shows a synchronous generator (SG) or a permanent

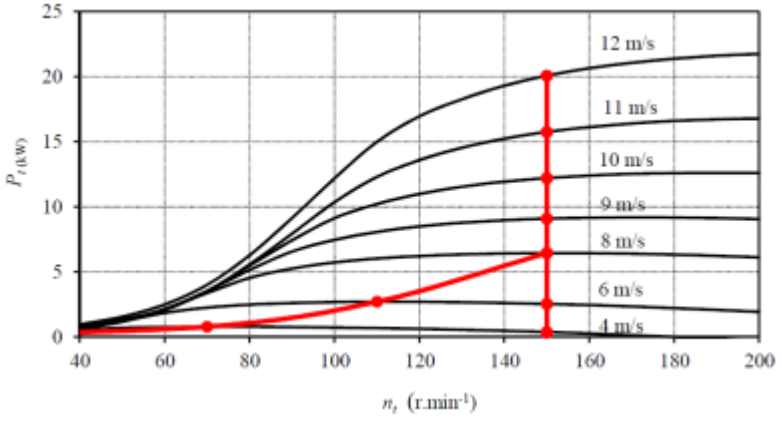

Figure 3.1: Turbine Power Curves with Proposed Operational Speed, (21)

magnet synchronous generator (PMSG) with full-scale frequency converter and both can be with or without a gearbox.

Based on the statistics of wind power system failure, (24), the weakest links in the power train for the wind turbine configurations are the mechanical gearboxes. Typically wind turbines have a 20 year design lifetime; the gearboxes however commonly fail within an operational period of 5 years. It may alleviate the problem if the mechanical gears are replaced with magnetic gears, as MGs operate contactless, no lubrication is required, which decreases the amount of maintenance and which could increase the operational lifetime.

However for this project a combined magnetic gear and permanent magnet generator is designed, which could further increase the advantages. A combined machine offers advantages, such as high power density, which may reduce the size and weight of a wind turbine when compared to conventional systems. Thus, for this project a configuration as shown in Figure 3.3 is designed and investigated.

In Figure 3.4 three different topologies of coaxial magnetically geared machines, namely; radial, linear and axial topologies are illustrated.

The machine in Figure 3.4 (a) is a magnetically geared radial-flux PM generator. This topology has been widely investigated in literature (15; 19; 20; 59; 60; 78). The machine is of smaller size and lighter weight when compared to a direct-drive PM machine and a planetary-geared PM machine with equivalent design parameters (15). Thus, the machine exhibits high power density and good torque quality.

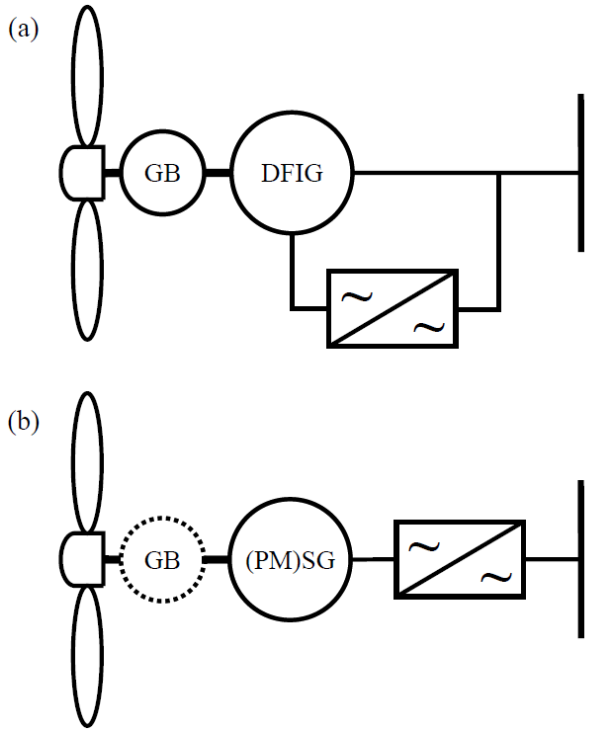

Figure 3.2: Conventional Grid-Connected Wind Power Generation System Configurations: (a) DFIG with Gearbox and Partial-Scale Frequency Converter, (b) SG or PMSG with Full-Scale Frequency Converter (22)

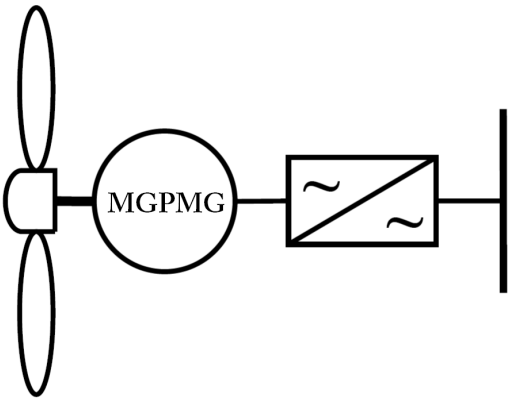

Figure 3.3: Grid-Connected Magnetic-Geared Permanent Magnet Generator with Full-Scale Frequency Converter

The linear machine of Figure 3.4 (b) does not fit the scope of this project, however it is mentioned to show the different topologies of the magnetic gear. In the figure only the gear part of the machine is shown, a stator can also be added as in the other machines in the figure. The combined machine could be a good alternative in wave energy or applications where linear motion needs to be converted directly to electrical power. The linear gear offers a highly competitive force density when compared to traditional linear actuators, such as a leadscrew and a nut (16).

The machine (c) in Figure 3.4 is a magnetically geared axial-flux PM generator. The axial-flux topology has never been constructed, only (17) have simulated the gear part of the machine. This topology is especially suitable for applications which require isolation between the input and output shafts, such as pumps. Since all of the components are observable the topology is also suitable for experimental evaluation. The disadvantage of this topology is that the axial forces of the rotors could be problematic, since the forces are predominantly in one direction, they do not counter each other as in radial machines.

The axial-flux topology was chosen for this project, because of the novelty of this topology and the observable rotors in experimental evaluation. Thus, this will be the first time an axial-flux magnetically geared machine is designed and experimentally tested.

Another aspect which needs to be discussed, is whether the high-speed rotor needs double- or single-row permanent magnets. Figure 3.5 illustrates the two different high-speed rotor configurations. With the single-row PMs the magnetic gear part of the machine will always be magnetically coupled to the generator part of the machine. In this configuration the torque density will improve, since the axial length of the machine will decrease. However the decrease in space will also complicate the mechanical design, since little room is left for mechanical strengthening. In the double-row configuration more space is available for mechanical strengthening and the machine can be configured to be magnetically coupled and decoupled, which will be explained further in the following chapters. The double-row configuration was chosen for this project, since mechanical strength is a major concern for axial-flux topologies.

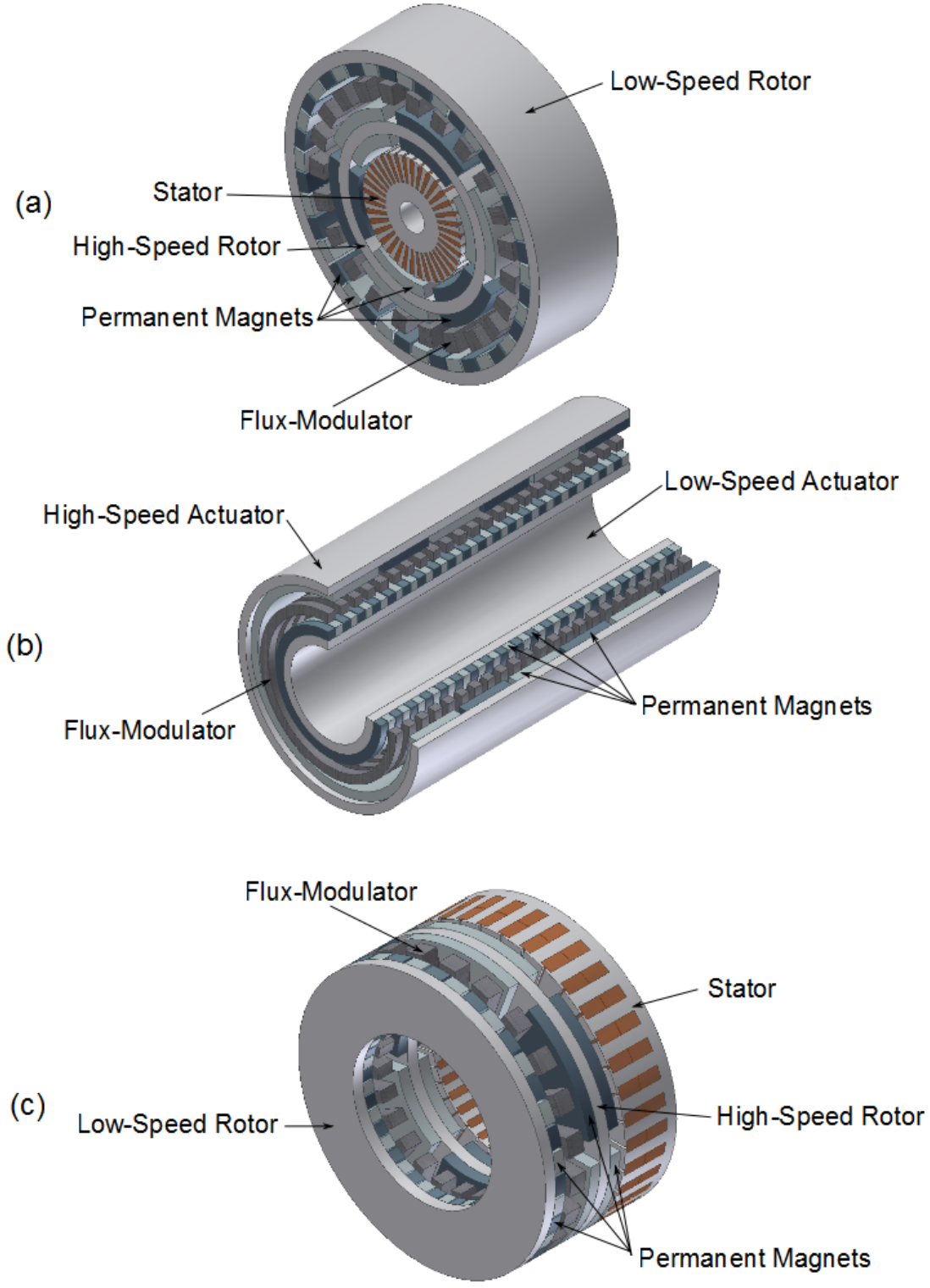

Figure 3.4: Coaxial Magnetic Geared Integration Topologies: (a) Magnetic-Geared Radial-Flux Generator, (b) Linear Magnetic Gear, and (c) Magnetic-Geared Axial-Flux Generator

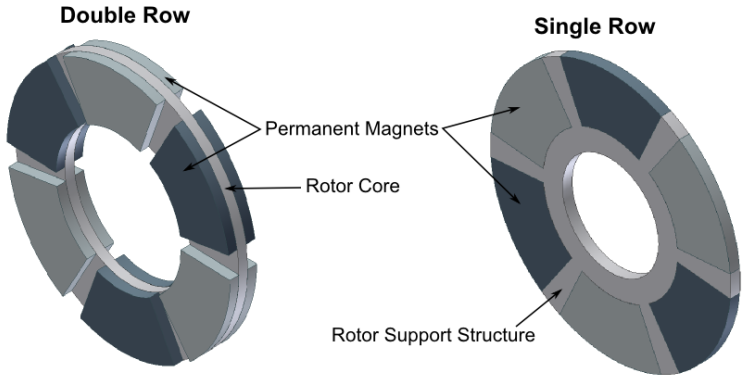

Figure 3.5: Double- versus Single-Row PM High Speed Rotor Configurations

3.3 Calculating Machine Parameters

In this section a procedure for calculating initial machine parameters with good torque quality will be considered. In the first part the general approach of how to determine the best parameters for a magnetically geared machine is described and in the second part the parameters chosen for this project is described, since an industrial stator was chosen for the project.

3.3.1 Calculating Machine Parameters for a Magnetic Gear

The gear ratio G_r of the machine is a function of the number of pole-pairs on the high- and low-speed rotors (p_H and p_L) and the number of modulation pieces n_s, as explained in the previous chapter. Thus, a good approach of choosing the machine parameters is to keep an initial parameter fixed and sweep through the other parameters. For instance if the number of high-speed pole-pairs is known, calculate the other parameters for a number of instances and choose the parameters with the best qualities:

For example if the number of pole-pairs on the high speed rotor was chosen as $p_H = 3$, calculate the rest of the parameters for the number of pole-pairs on the low-speed rotor p_L from 1 to 40. The gear ratio can then be calculated with Equation 2.12 from the previous chapter.

$$G_r = \frac{n_H}{n_L}$$

Next the number of modulation pieces n_s can be determined (from Equation 2.13):

$$n_s = p_H + p_L$$

With these parameters known the correct combination should be chosen, ideally the combination with the best torque characteristics. To check the severity of the cogging torque, a cogging factor f_c is introduced, from (87). The cogging factor gives a good indication of the severity of the cogging torque.

The lower the cogging factor the lower the cogging torque will be. The cogging factor is expressed as:

$$f_c = \frac{2pn_s}{N_c} \tag{3.4}$$

where N_c is the smallest common multiple between the number of poles on one of the permanent magnet rotors p and the number of modulation pieces n_s. From the equation it can be observed that the larger the smallest common multiple and the lower the number of poles, the smaller the cogging factor will be and thus the cogging torque. To obtain the lowest cogging torque the factor should be one ($f_c = 1$).

Figure 3.6 illustrates the machine parameter combinations with 3 pole-pairs on the high-speed rotor. In Appendix A the machine parameter combinations for 1,2 and 4 pole-pairs on the high-speed rotor can be seen.

From Figure 3.6 it is observed that the cogging factor is the lowest for fractional gear ratios. In (77) the authors designed a MG for wind turbine applications. In the paper a number of gear ratios were simulated and compared, the authors concluded that fractional gear ratios offer the best performance.

3.3.2 Calculating Machine Parameters for MGAFG

In this section the machine parameters are calculated for the magnetically geared axial flux generator that was designed and constructed for this project.

Since an industrial stator was chosen for the project, some of the parameters are fixed. The technical specifications of the stator are summarised in Table 3.1.

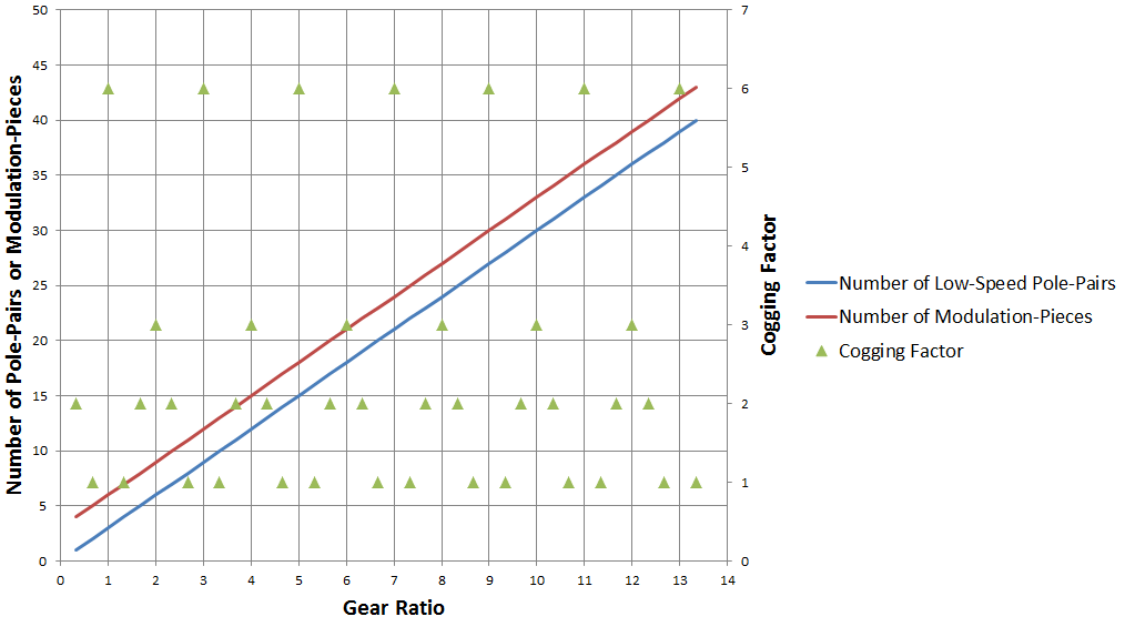

Figure 3.6: Machine Parameters for 3 Pole-Pairs on the High-Speed Rotor ($p_H = 3$)

Table 3.1: Technical Specifications of Axial Flux Stator

Power Rating [kW]	4
Number of Poles	6
Winding	Double-Layer
Number of Turns per Coil	27
Wire Size [mm]	0.9
Wires per Conductor	3 Parallel
Connection	Star
Coils per Phase	12
Outside Diameter [mm]	250
Inside Diameter [mm]	140
Axial Length [mm]	58.8

From the table it can be seen that the high-speed rotor should have 6 poles, ($p_H = 3$). In order to generate electricity at 50 Hz with 6 poles the high-speed rotor needs to rotate at:

$$n = \frac{120f}{p} \tag{3.5}$$

$$n_H = \frac{60f_{out}}{p_H} = \frac{60 \times 50}{3} = 1000rpm$$

From the input speed determined in the previous section (n_L = 150 rpm) and the high-speed rotor speed (n_H = 1000 rpm), the gear ratio can be determined:

$$G_r = \frac{n_H}{n_L} = \frac{1000}{150} = 6.667$$

With the gear ratio the number of poles on the low-speed rotor can be determined:

$$G_r = \frac{p_L}{p_H}$$
$$6.667 = \frac{p_L}{3}$$
$$p_L = 6.667 \times 3 = 20$$

Next the number of modulation pieces n_s are determined:

$$n_s = p_H + p_L = 23$$

The smallest common multiple between $p = 2 \times p_H$ and n_s is $N_c = 138$. Thus the cogging factor can be determined with Equation 3.4:

$$f_c = \frac{2 \times 3 \times 23}{138} = 1$$

Thus the cogging torque will not be very high. The results are summarised in Table 3.2.

Table 3.2: Magnetic-Geared Machine Parameters

p_H	3
n_H [rpm]	1000
p_L	20
n_s	23
G_r	6.667
f_{out} [Hz]	50
f_c	1

CHAPTER 4

DESIGN AND OPTIMISATION

In this chapter, the electrical design and optimisation procedure for magnetically geared permanent magnet generators are described. In the first section the performance calculation process of the machine, which consists of a finite element method (FEM) program and an external Python script is described. The FEM program calculates the flux-linkages between the coils and the permanent magnet poles and the relevant forces on the different components of the machine. The external script is then used to do further calculations or post-processing on the results obtained from the FEM program. In these programs the input dimensions and material properties are taken as input parameters and the machine performance is accurately calculated.

In the second section the optimisation algorithm used to optimise the machine within the required constraints is described. In the last section the results obtained with the optimisation process are described.

4.1 Performance Calculation Process

The performance calculation process consists of an FEM program, a Visual Basic Script and an external Python Script (or Post-Processing Script). Figure 4.1 shows the flow chart of the performance calculation process.

4.1.1 Finite Element Method

Finite element method (FEM) is a numerical method that is extensively used in the design and simulation of electrical machines. This technique allows the machine performance, such as torque, power and efficiency to be calculated accurately through the direct evaluation of the magnetic fields in the machine.

In the finite element method, the model is discretized into a mesh of elements. The field inside each element is represented by a polynomial with unknown coefficients. The finite element analysis is the solution of the set of equations for the unknown coefficients. In 2D, the elements are shaped like triangles defined by three vertices (nodes).

The accuracy of the solution depends on the nature of the field and the size of the mesh elements. High accuracy requires small elements in the regions where the direction or magnitude of the field changes rapidly, such as in the air-gaps, the teeth tips or in the smaller components.

There are a number of commercial packages that implement FEM. For this project MagNet 7.1.2 from Infolytica Corporation is used to model the machine (88).

The machine can either be modelled in 2D or 3D. A two dimensional model is chosen to simplify

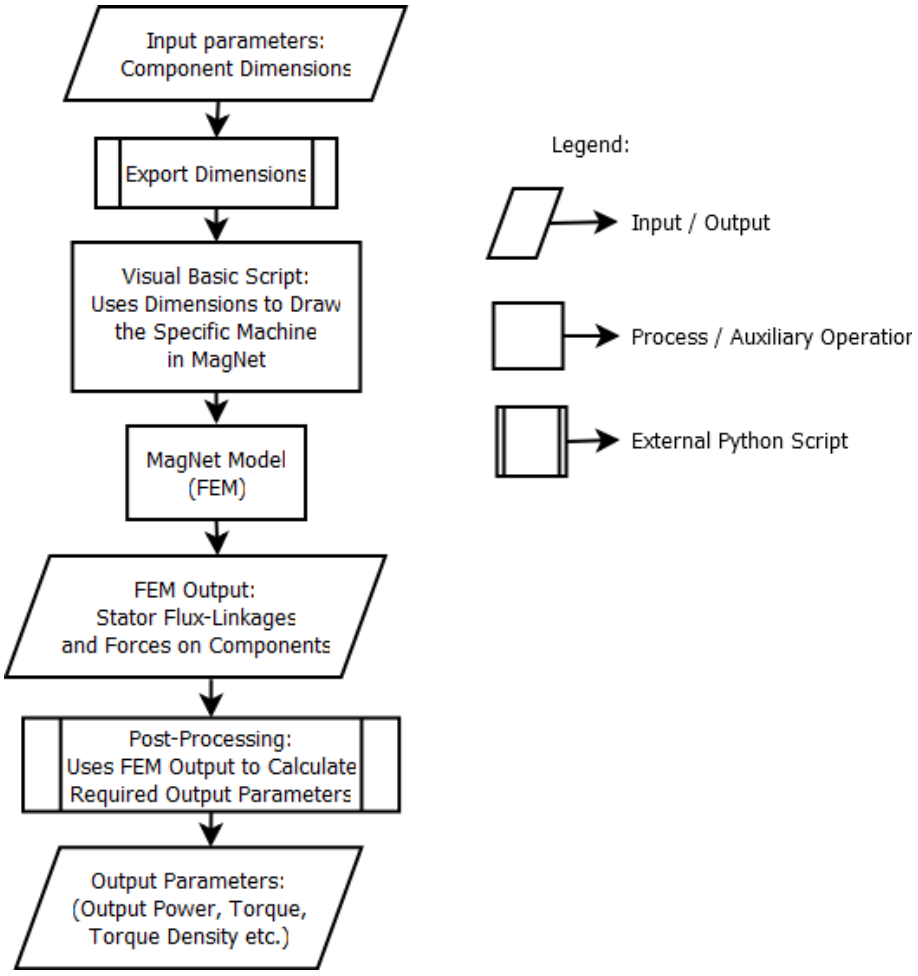

Figure 4.1: Performance Calculation Process Flow-Diagram

the model and to keep the processing time as short as possible. To model an axial-flux topology in 2D it is necessary to represent the machine as a linear machine with positive periodical boundaries. Figure 4.2 illustrates the concept of how an axial-flux permanent magnet rotor is converted to a linear representation. To calculate the length L_{linear} and the thickness T from the axial-flux topology the following equations 4.1 and 4.2 can be used:

$$L_{linear} = \frac{\pi(D+d)}{2} \tag{4.1}$$

$$T = \frac{D-d}{2} \tag{4.2}$$

where D and d are the outer- and inner-diameters of the rotors, respectively. To calculate the average radius, R, equation 4.3 can be used.

$$R = \frac{D+d}{4} \tag{4.3}$$

Normally only a symmetrical section of an electrical machine needs be modelled, this greatly reduces the time it takes to complete a simulation. The end results can then be multiplied by the number of symmetrical sections in order to obtain the results for the complete machine. However the MGAFG machine is not symmetrical, this means that the complete machine needs to be modelled in order to obtain accurate results.

Figure 4.3 illustrates the model layout and Figure 4.4 is the full model in MagNet with magnetic flux-lines to demonstrate the positive periodical boundaries.

In order to use the FEM model in conjunction with a optimisation algorithm, the model needs to be generic.This means that the input parameters, such as the dimensions and the material properties need

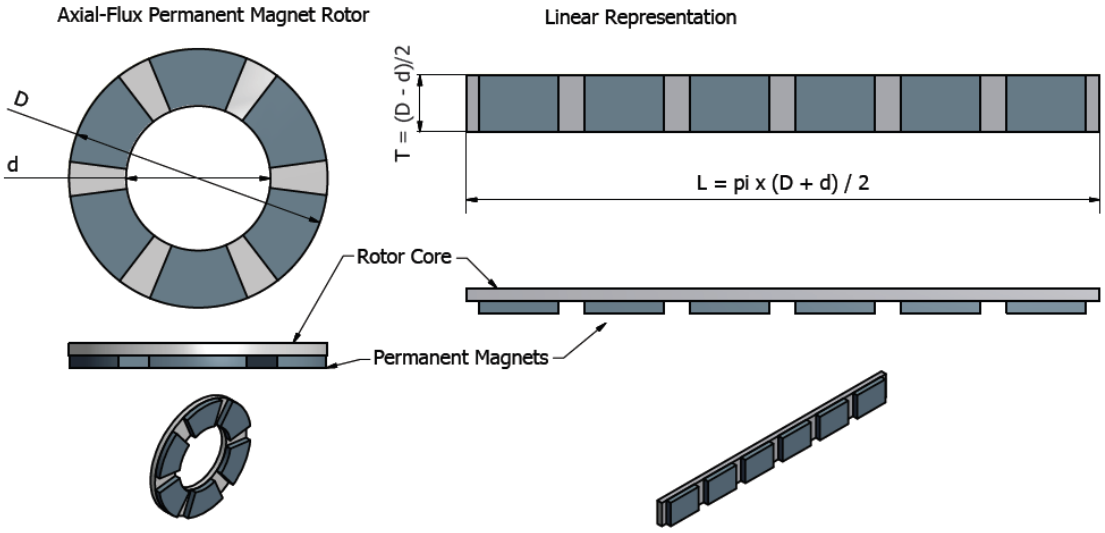

Figure 4.2: Linear Representation of an Axial-Flux Permanent Magnet Rotor

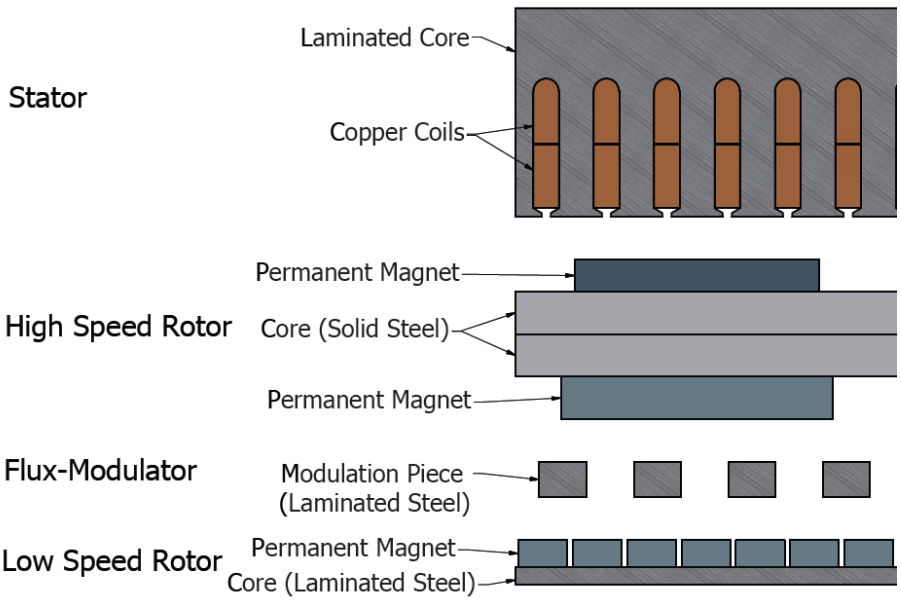

Figure 4.3: Full Model to Demonstrate MagNet Model Layout

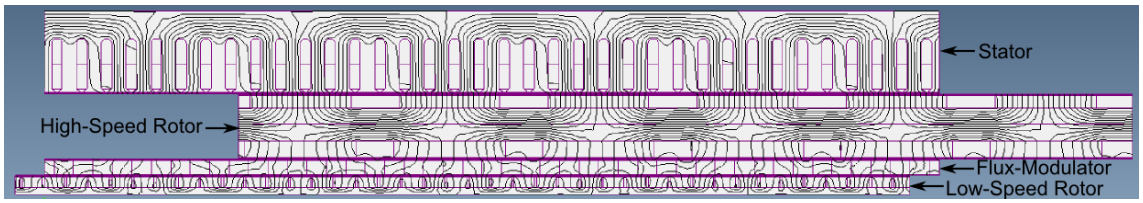

Figure 4.4: Full Machine with Magnetic Flux-Lines to Demonstrate the Positive Periodical Boundaries

to be changeable. MagNet allows Visual Basic Scripts which are used to draw, simulate and export the model results. Figure 4.5 and Table 4.1 illustrate the model variables that are used in the Visual Basic Script.

4.1.2 Post-Processing Script (Python)

With the FEM model in place the design objectives can be calculated. A Python Script is used to calculate the desired output parameters after each simulation. The Python script acts as a conduit between the optimisation algorithm and the FEM program, funnelling the input dimensions to the FEM program, extracting and further processing the output results.

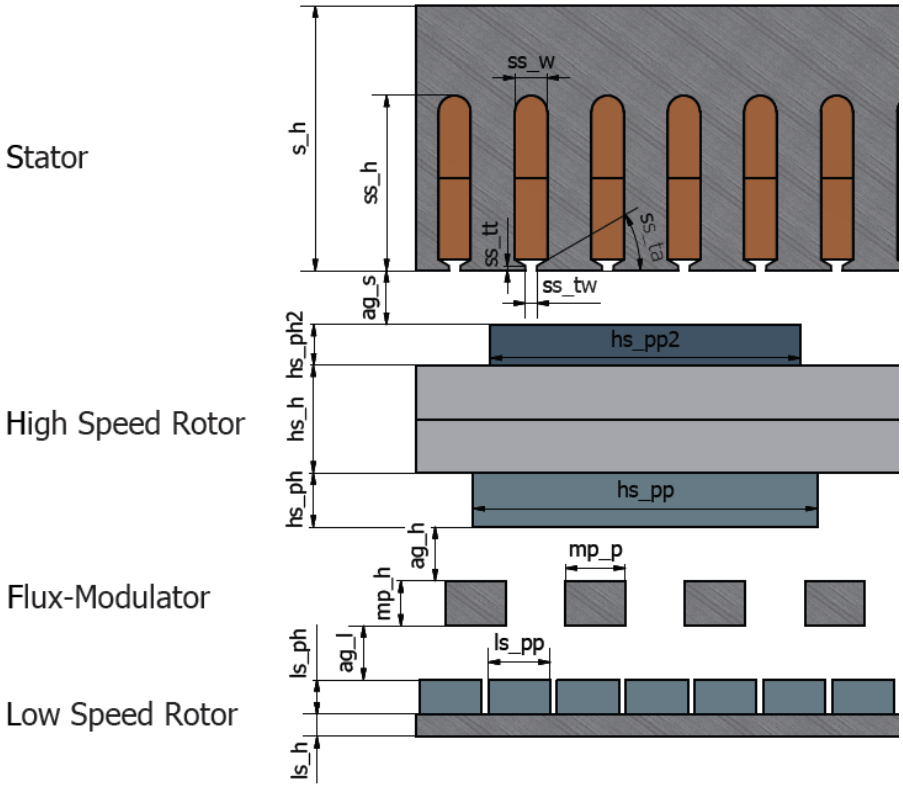

Figure 4.5: MagNet Model Variables

Table 4.1: Variables Description

Variable Name	Variable
Stator:	
Height	s_h
Slot Height	ss_h
Slot Width	ss_w
Slot Tooth Thickness	ss_{tt}
Slot Tooth Width	ss_{tw}
Slot Tooth Angle	ss_{ta}
Air-Gap	ag_s
High Speed Rotor:	
Core Height	hs_h
Pole Height 1	hs_{ph}
Pole Pitch	hs_pp
Pole Height 2	hs_{ph2}
Pole Pitch	hs_{pp2}
Air-Gap	ag_h
Flux-Modulation:	
Height	mp_h
Pitch	mp_p
Low Speed Rotor:	
Core Height	ls_h
Pole Height	ls_{ph}
Pole Pitch	ls_{pp}
Air-Gap	ag_s

To calculate the performance of the machine the torque on each rotor, the volume of each component and the power delivered by the stator are calculated. Since the FEM model is represented as a linear model, only the force on each moving body is calculated. To calculate the torque the force is simply multiplied with the average radius R of the rotors.

$$T_{avg} = F_{avg}R \tag{4.4}$$

Next the volume is easily calculated with the input dimensions (see Figure 4.5). To calculate the torque density T_D, the torque delivered by the low-speed rotor is divided by the total volume of the gear part of the machine.

$$V_{GEAR} = (hs_h/2 + hs_{ph} + ag_h + mp_h + ag_l + ls_{ph} + ls_h).L.T \tag{4.5}$$

$$T_D = T_{LS}/V_{GEAR} \tag{4.6}$$

Lastly the output power of the machine is calculated. The output power is calculated by using the flux-linkages of the stator coils and the equivalent dq-circuit theory as described in Chapter 2.

4.2 Optimisation Algorithm

Optimisation algorithms generally fall into two categories, namely gradient-based algorithms and non-gradient based algorithms (also known as global algorithms or non-traditional algorithms). In gradient based algorithms the gradient of the objectives and constraints is normally computed to get the next best solution. Generally this allows the gradient based algorithms to reach an optimum using fewer solutions than is the case with non-gradient based algorithms. The disadvantage of gradient-based algorithms in electrical machine design, especially in complicated designs as in this project, is that the algorithms tend to converge to local optima and not global optima. To counter the convergence to local optima more than one starting position can be used to determine if the global optima are reached, or more than one gradient-based algorithm can be used.

In non-gradient algorithms this is not the case, the algorithms may take longer to converge but the global optimum will generally be reached. An interesting aspect of almost all non-gradient based algorithms is that they are motivated from some process or phenomenon occurring in nature. There are two main non-gradient based algorithms which are normally used in electrical machine design. The first is Genetic Algorithms (GA) which are inspired by Darwin's theory of the survival-of-the-fittest. A simple GA involves two major operations, which are selection (survival of the fittest) and reproduction (crossover and mutation). The second non-gradient based algorithm which is widely used is the Particle Swarm Optimisation (PSO) algorithm. The PSO algorithm was chosen for this project and will be discussed in more detail.

4.2.1 Particle Swarm Optimisation

PSO was developed in 1995 by James Kennedy and Russel Eberhart (89; 90; 91).

The working principle of the PSO is based on the collective intelligence of a group of animals (birds or fish) moving together. Figure 4.6 is a flow diagram of the PSO process, which assists the explanation.

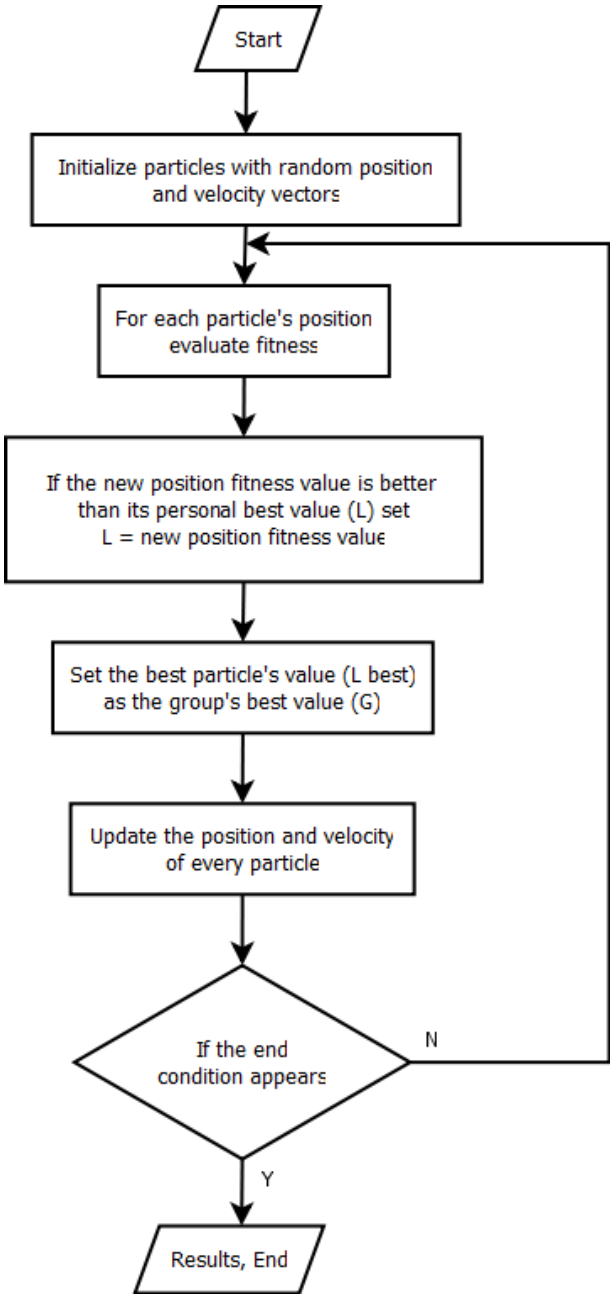

Figure 4.6: Particle Swarm Optimisation Flow Diagram

Consider a group of fish searching for food in a given area (or the search space). Assume that the fish do not know where food can be found in the given area. The objective of the fish is to find the location of the food, so the location of the food becomes the optimum and the motion of the fish is the optimisation process. Assume the fish know how close they are to the food at any instant (iteration).

Since the fish in the group know how close each member of the group is to the food, the best strategy for them is to follow the fish nearest to the food (follow the current best solution).

There are two concerns with this approach. The first is what should the current best fish do? Should it continue to move in the same direction as before? The second is if all the other fish follow the current best fish they will trace the same path and there is no benefit of using more than one fish.

This is where the idea of collective intelligence (social behaviour) of a group is introduced. Every particle (or fish) has the following information.

1. The best value achieved so far by any particle in the group (G).
2. Its own best value achieved so far (L).
3. The third type of information (which is optional) is based on the idea of the immediate neighbourhood. Every particle can communicate with its immediate neighbours (a subset of solutions closest to it in the decision space) and can learn from their experience (let the value of the best solution in its neighbourhood be N).

In PSO, the position (value of the design variable) of a particle is updated using the following formula.

$$v_t' = c_o v_i + c_1 r_1 (G_i - x_i) + c_2 r_2 (L_i - x_i) + c_3 r_3 (N_i - x_i) \tag{4.7}$$

$$x_i' = x_i + v_i' \tag{4.8}$$

In the above equation, the subscript 'i' refers to the index of the variable, x_i and v_i are the position and velocity at the previous iteration, and x_i' and v_i' are the position and velocity at the current iteration. The parameters r_1, r_2 and r_3 are uniformly distributed random numbers in (0, 1) and c_0, c_1, c_2 and c_3 are the learning factors. Typically $c_0 = 1$ and $c_1 = c_2 = c_3 = 2$.

4.3 Optimisation Considerations

Before the optimisation results are given a few of the issues considered need to be stated.

- The main objective of the optimisation process is to design a magnetic gear that can supply enough output torque to supply the permanent magnet generator to produce rated output power.
- Since not all of the losses can be accounted for in the two dimensional analysis and theoretical designs are not always 100% efficient, as was seen in (92), it is decided that the machine will be designed at a 50 % workpoint. Or differently stated, the gear is designed to operate at half capacity, which means that the start position of the low-speed rotor is adjusted to work at half of its pull-out torque. This is done to ensure that the magnetic gear will deliver the correct amount of torque to the generator, to produce enough output power, even when unexpected losses occur.

  To determine the correct start position for the low-speed rotor the magnetic gear is simulated in the FEM program. The low-speed rotor is kept stationary and the high-speed rotor rotated for one pole-pair, which is 120°, since there are 3 high-speed pole-pairs. The FEM program however,

works in milliseconds. Thus, the 120° translates to 20 ms, since the high-speed rotor rotates at 1000 rpm. This produces a graph as observed in Figure 4.7. From the figure it is seen that the maximum torque for both rotors is reached at 5 ms. Thus, the low-speed rotor's start position was moved 3.333 ms relative to the high-speed rotor's start position to transfer torque at a 50 % work point.

The design specifications made in the preceding chapters are summarised to form the design inputs which are given in Table 4.2.

4.4 Optimisation Results

Two optimisation cases were investigated. The first is where the permanent magnet generator and the magnetic gear are magnetically decoupled and the second is where they are magnetically coupled. Figure 4.8 illustrates this principle with a magnetic flux-line sketch generated in the FEM program. To decouple the generator from the gear magnetically the north poles on the generator are simply switched with the south poles, which forces the magnetic fields to turn around inside the rotor core. Since the performance of the machine varies with the two approaches, both are investigated.

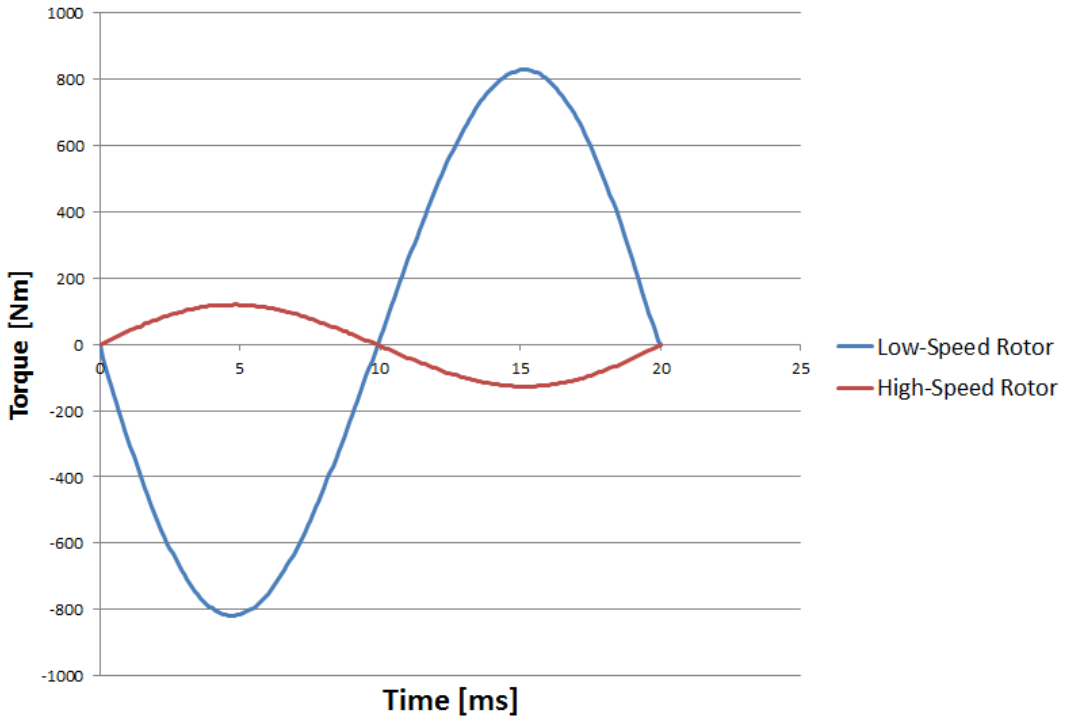

Figure 4.7: High- and Low-Speed Torque at Relative Positions to Determine Work-Point (with 2mm air-gaps)

Table 4.2: Prototype Design Specifications

Component	Design Specification
Stator	
Power	4 kW
Slots	36
Inner Diameter	140 mm
Outer Diameter	250 mm
Operating Temperature	$75°C$
Core Material	Laminated Steel
Air Gap	2 mm
High Speed Rotor	
Poles	6
Speed	1000 rpm
Core Material	Solid Steel
Magnet Material	$Nd_2Fe_{14}BN48$
Air Gap	2 mm
Modulation Pieces	
Number of Pieces	23
Material	Laminated Steel
Low Speed Rotor	
Poles	40
Speed	150 rpm
Core Material	Laminated Steel
Magnet Material	$Nd_2Fe_{14}BN48$
Air Gap	2 mm
Objectives	
Output Power	$\geq$ 4 kW
Torque Density	Maximum
Magnet Material Mass	Minimum

4.5 Magnetically Decoupled Optimisation

For the magnetically decoupled configuration it can be assumed that the magnetic forces on the gear part of the machine will only slightly influence the performance of the generator part of the machine. With this assumption the generator and the gear were optimised separately, which greatly reduced the optimisation time required.

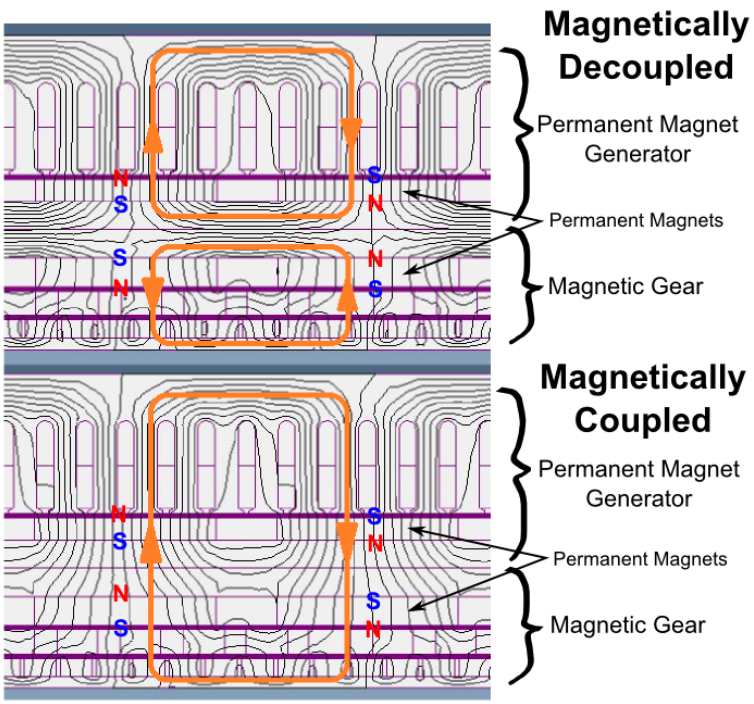

Figure 4.8: Permanent Magnet Generator and Magnetic Gear Magnetically Decoupled and Coupled Flux-Line Demonstration

4.5.1 Performance Calculation of Permanent Magnet Generator

The first part of the optimisation is to calculate the performance of the PMG or more specifically calculate the required input torque that produces the required output power. This is accomplished by simulating the PMG in the FEM program. The FEM program takes the current density as input parameter and calculates the flux-linkages and the force on the rotor. The force is easily converted to torque with Equation 4.4 and the output power is calculated with the flux-linkages. To calculate the output power the equivalent dq-circuit theory from Chapter 2 is employed. The results can be seen in Figure 4.9. The input current-density J was taken from 0 to 10 A/mm^2, producing a maximum of 10.72 kW at 106.4 Nm. From this it is observed that the generator needs just over 50 Nm of input torque to produce the 4 kW of output power.

4.5.2 Magnetic Gear Optimisation

With the required torque known the MG is optimised. The MG is optimised with the optimisation algorithm, the FEM program and the post-processing script as described in the preceding sections. From the design specifications it can be observed that the MG needs to be designed to produce the required torque, while keeping the volume and the permanent magnet material to a minimum.

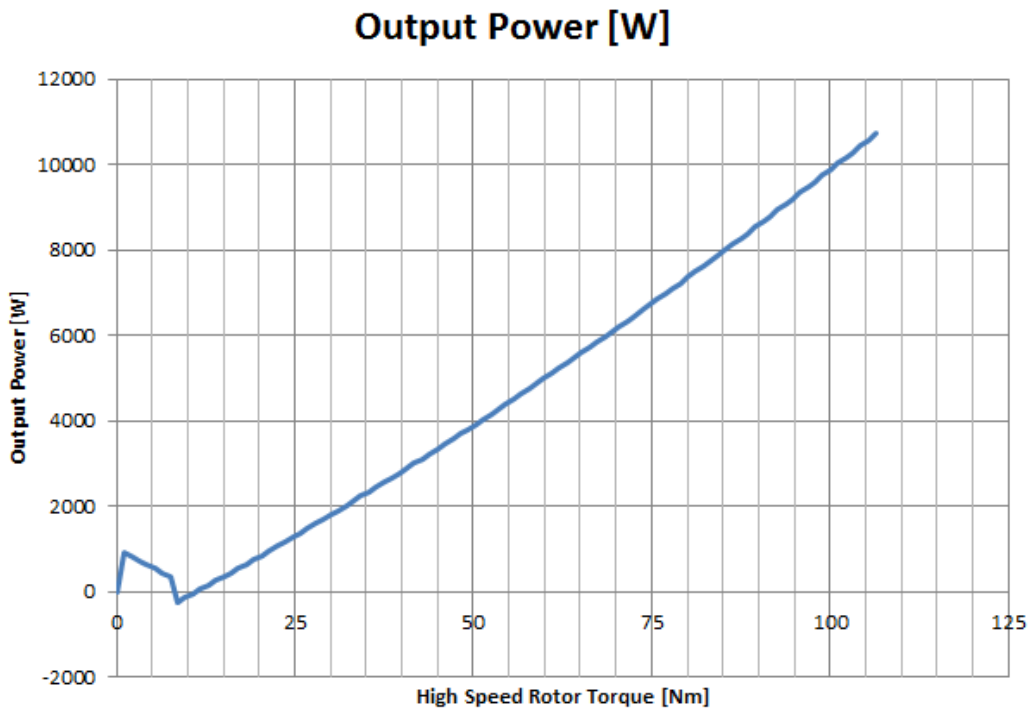

Figure 4.9: Generator Output Power Produced from Input Torque

4.5.2.1 Optimisation Results of a Magnetic Gear with the Same Diameter as the Permanent Magnet Generator

The first optimisation that was done on the MG was to determine if the magnetic gear can deliver enough output torque to the generator if the diameters of the gear and the generator stay the same. The maximum torque that can be delivered to the generator from the gear, when both diameters are equal, is T_H = 24.43 Nm, which is not even half of the required torque.

When the permanent magnet (PM) material is minimised, which is one of the main design concerns, the torque achieved is only T_H = 19.44 Nm. Table 4.3 lists all the constraints and results for the PM material minimisation optimisation.

4.5.2.2 Different Diameter Optimisation

The next optimisation that is done is to expand the outer diameter D of the gear part of the machine to see if the MG can supply the correct output torque. The stator's end-winding outer diameter is 320mm, thus the outer diameter of the gear can be enlarged without increasing the outer diameter of the machine. The machine is also optimised for maximum torque density and minimised for permanent magnet material used. All of the constraints and results obtained from the optimisation are listed in Table 4.4.

From the results it can be observed that all of the requirements are achieved. The minimum high speed rotor torque is reached, a torque density of T_D = 105 kNm/m^3 is reached, which is very high considering that the MG is designed at 50% workpoint. The PM material weight is high compared to

Table 4.3: Optimisation Results of Magnetic Gear with the same Diameter as the Permanent Magnet Generator

Machine Component	Optimisation Constraints	Optimised Results
Input Parameters		
LS Rotor Height (ls_h)	5mm $\leq ls_h \leq$ 20mm	5mm
LS Pole Height (ls_{ph})	4mm $\leq ls_{ph} \leq$ 20mm	12mm
LS Pole Pitch (ls_{pp})	$0.7 \leq ls_{pp} \leq 0.95$	0.8
MP Height (mp_h)	10mm $\leq mp_h \leq$ 30mm	10mm
HS Rotor Height (hs_h)	20mm $\leq hs_h \leq$ 30mm	30mm
HS Pole Height (hs_{ph})	4mm $\leq hs_{ph} \leq$ 12mm	12mm
HS Pole Pitch (hs_{pp})	$0.4 \leq hs_{pp} \leq 0.9$	0.9
Objective		
PM Material Mass	minimise	4.033 kg
Constraint		
HS Torque (T_H)	$T_H \geq$ 50Nm	19.44 Nm

that of the previous optimisation, which is expected since the diameter of the machine is enlarged. Even though the amount of PM material (7.73 kg) used is high the required torque and the torque density achieved is exceptional, thus the design is satisfactory.

Table 4.4: Different Diameter Optimisation Results

Machine Component	Optimisation Constraints	Optimised Results
Input Parameters		
Outer Diameter (D)	250mm $\leq D \leq$ 330mm	320mm
Inner Diameter (d)	100mm $\leq d \leq$ 140mm	140mm
LS Rotor Height (ls_h)	5mm $\leq ls_h \leq$ 20mm	5mm
LS Pole Height (ls_{ph})	4mm $\leq ls_{ph} \leq$ 20mm	7.6mm
LS Pole Pitch (ls_{pp})	$0.7 \leq ls_{pp} \leq 0.9$	0.9
MP Height (mp_h)	10mm $\leq mp_h \leq$ 30mm	10mm
MP Pitch (mp_p)	$0.3 \leq mp_p \leq 0.7$	0.65
HS Rotor Height (hs_h)	20mm $\leq hs_h \leq$ 50mm	24mm
HS Pole Height (hs_{ph})	4mm $\leq hs_{ph} \leq$ 20mm	12mm
HS Pole Pitch (hs_{pp})	$0.5 \leq hs_{pp} \leq 0.9$	0.75
Objective		
Torque Density (T_D)	maximise	105 kNm/m^3
Constraints		
HS Torque (T_H)	$T_H \geq$ 50 Nm	52.4 Nm

4.5.3 Optimised MGAFG Performance

In this section the performance of the decoupled MGAFG machine is calculated. First the performance is calculated for maximum power and then for rated power. The machine should not be operated at maximum power, since the gear starts to slip at maximum power.

Maximum MGAFG Performance

The first step is to calculate the total losses of the machine with the optimised dimensions (see Table 4.5). With the total losses the performance of the optimised decoupled MGAFG machine is calculated with the equivalent circuit theory as described in Chapter 2. The results is summarised in Table 4.6.

From the table it is observed that the efficiency for the decoupled MGAFG is 95.94 % at maximum torque.

Table 4.5: Loss Calculation of Decoupled MGAFG

Component	Ohmic Loss	Hysteresis	Eddy Current	Components	Total Loss [W]
LS Magnet	1.559			40	62.358
LS Laminated Core		12.268	2.83	1	15.099
MP Stainless Steel Rod	0.06			23	1.379
MP Laminations		0.777	0.119	23	20.623
HS Magnet Gear Side	20.393			6	122.36
HS Magnet Stator Side	0.793			6	4.76
HS Solid Steel Core	48.241			1	48.241
Stator Coil	1.094			72	78.768
Stator Core		34.782	5.153	1	39.935
Total					**393.523**

Table 4.6: Maximum Performance Calculation of Decoupled MGAFG

Parameter	Value
i_{rms}	14.086 A
V_{rms}	219.714 V
KVA	9.285 kVA
Total Loss	350.676 W
Input Power	8631.902 W
Output Power	8281.225 W
Power Factor	0.8919
Efficiency	95.94 %

Rated MGAFG Performance

The rated performance is calculated for the optimised MGAFG at 50% workpoint (see Table 4.7).

For rated power the machine is 92.55 % efficient.

4.5.4 Torque Ripple Reduction Results

Torque quality is one of the most important aspects to consider in the design of wind generators, (93). Torque quality refers to the torque ripple generated by the machine. The torque ripple is mainly caused by the slotted air-gaps and the stator winding MMF harmonics of the machine. At no load the slotted air-gaps cause the so-called cogging torque of the machine. The cogging torque is caused by the permanent magnets on the rotor, which attempt to align themselves with the slots of the machine. Cogging torque increases the start-up torque of the machine, which means that the turbine can only start to produce power at higher wind speeds. Torque ripple on the other hand can be a source of serious vibration and acoustic noise in wind generator systems. Thus improving the torque quality is of utmost importance.

Several techniques exist to improve the torque quality of PM machines. These techniques include skewing the magnets and stator slots, closing stator slots, introducing auxiliary slots and varying the magnet positions (87; 94; 95; 96; 97; 98; 99; 100).

To use these techniques on the magnetic gear the flux-modulator can be seen as a series of stator slots.

The varying of the magnet positions technique, from (100), is chosen to minimise the torque ripple. The following equation is used to determine the optimum angle to shift the magnets relatively to each other in order to obtain the least amount of torque ripple.

$$\theta_o = \frac{2\pi\gamma}{n_s N_p} \tag{4.9}$$

where θ_o is the angle that each magnet needs to be shifted relative to the others, γ is the integer

Table 4.7: Rated Performance Calculation of Decoupled MGAFG

Parameter	Value
i_{rms}	6.919 A
V_{rms}	213.623 V
KVA	4.434 kVA
Total Loss	331.897 W
Input Power	4457.291 W
Output Power	4125.394 W
Power Factor	0.93
Efficiency	92.55 %

multiple of magnets out of phase with each other ($\gamma = 1$) and as mentioned n_s and N_p are the number of slots and poles respectively.

From Equation 4.9 the angle that each magnet needs to be shifted relative to the others is determined to be $\theta_o = 1.66°$. To obtain the most balanced rotor the centre of gravity is investigated for every possible θ_o combination. Table 4.8 gives the angle that each magnet needs to be shifted with to obtain the most balanced rotor.

In Figure 4.10 the simulated torque results obtained (from FEM, MagNet) are given. The average torque for the normal placement and the shifted magnets is T_{normal} = 52.02 Nm and $T_{shifted}$ = 51.08 Nm, respectively. The normal placement has 5% torque ripple and the shifted magnets has 3% torque ripple. So with a 1 Nm drop in average torque a 2% reduction in torque ripple are achieved.

4.6 Magnetically Coupled Optimisation

In this section the coupled machine optimisation approach is described. This approach is not as straight forward as the decoupled approach, since the magnetic flux from the gear side of the machine influences

Table 4.8: Magnet Shift θ_o

Magnet	θ_o	θ_o With the Most Balanced Rotor
Mag 1	0	6.646
Mag 2	1.662	4.985
Mag 3	3.323	0
Mag 4	4.985	8.308
Mag 5	6.646	3.323
Mag 6	8.308	1.662

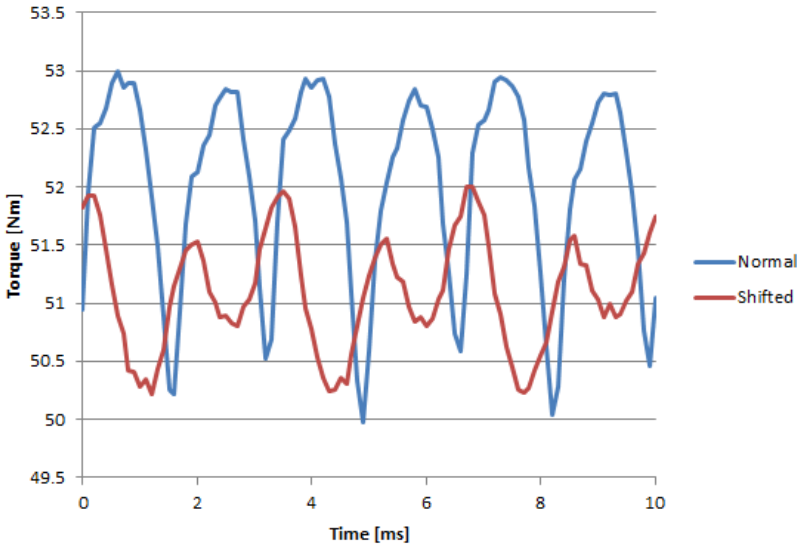

Figure 4.10: Torque Ripple: Normal Magnet Placement vs. Shifted Magnets

the performance of the generator side of the machine. This means that the full machine needs to be simulated for every design iteration.

4.6.1 Optimisation Process

The FEM program used requires the instantaneous three phase current in order to calculate the torque produced by the PMG rotor. The performance of the machine is calculated by the FEM program as if it is a motor and not a generator. In this project a generator is designed, this means that the simulation process is in reverse. To overcome this problem the current density that the stator coils can handle is determined and then it is converted to the instantaneous three phase currents, which are a function of the dimensions of the coils (see Equation 2.16).

This approach works when the machine that needs to be designed has only one rotor. The required torque to produce the current is then easily calculated with the current density J as input to the system. However in this project the machine that needs to be designed has more than one rotor. The low speed rotor is the input rotor and the high speed rotor is the interface between the PMG and the MG. The high speed rotor should then have zero torque when operational, since the torque produced by the MG, is converted to electrical power by the PMG. This complicates the simulation process, since the current that would balance the high speed rotor torque is not known before every simulation.

Figure 4.11 illustrates this problem. The inputs of the MG are the instantaneous three phase currents and the component dimensions and the output is the torque of the high speed rotor. However the input of the MG is also the component dimensions and the output is the torque produced by the high speed rotor. The problem with this setup is that the torque of the high speed rotor needs to be balanced (zero) in order to calculate the performance of the machine accurately. This can be solved by simulating the machine multiple times until the correct input current is known which will balance the high speed rotor. However this will greatly increase the time required to simulate one design iteration.

Another approach would be to calculate the torque that the PMG will produce for a number of current inputs (the same as was done in Figure 4.9). The MG can then be simulated to determine the torque of the high speed rotor. The full machine can then be simulated with the known torque that the MG produces and the estimated current that will balance the machine. The problem with this approach is that the two machines are still simulated decoupled and then joined, which will yield different results.

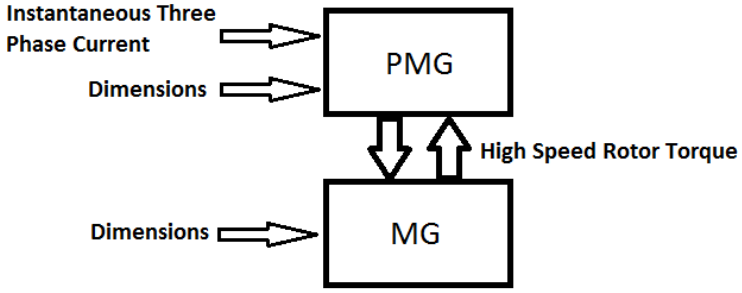

Figure 4.11: Full Coupled Model Simulation Description

4.7 Conclusion

In this chapter the simulation and optimisation processes are described. Two different design approaches are identified, namely the coupled and decoupled optimisation approaches. Due to the complexities and time required to complete the coupled design approach, only the decoupled approach is fully investigated. From the decoupled optimisation results, it is found that the axial-flux magnetic gear could reach a torque-density of over 100 kNm/m^3, which is significantly higher than traditional mechanical gears can achieve. It is also found that the torque quality of the MGAFG is reasonable without extra improvements.

CHAPTER 5

MECHANICAL DESIGN AND CONSTRUCTION

5.1 Introduction

To design an effective renewable energy converter involves both electrical performance design, mechanical strength and integrity considerations. In this chapter the forces, namely the electrical interaction, the mechanical interaction and the component properties such as weight are considered to investigate the strength and reliability of the MGAFG. While designing for mechanical strength the electrical properties should always be considered so as to keep unwanted losses to a minimum.

5.2 Electrical Specifications

In the previous chapter the main dimensions and resulting forces of the electrical components are determined. Figure 5.1 and Table 5.1 give the machine layout, material descriptions and dimensions of the individual components. The maximum forces on the flux-modulator, the high- and low-speed rotors can be seen in Table 5.2. Note that for the full-machine the resulting torque of the high-speed rotor should be near zero. This is due to the balance of the input electromagnetic torque of the gear versus the extracted torque of the stator. The worst case is chosen to allow for assembly when the forces on the high-speed rotor are not balanced. With the dimensions, the layout and the calculated forces known the MGAFG can be designed.

5.3 Mechanical Design of the Individual Components

From Figure 5.1 it can be seen that the stator and the flux-modulator are stationary and the low- and high-speed rotors rotate. The high-speed rotor needs to be able to rotate freely and the low-speed rotor is the input rotor.

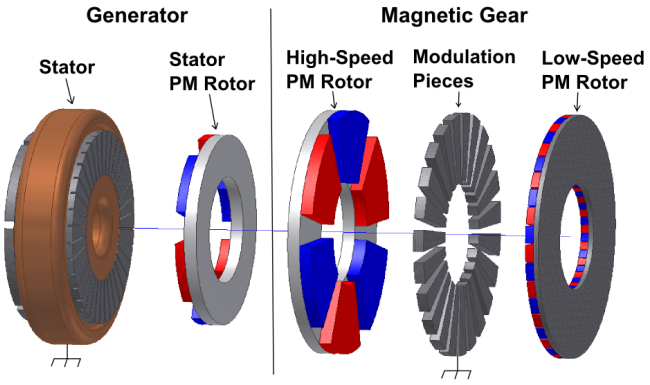

Figure 5.1: Electrical Model Representation

Table 5.1: Electrical Design Specifications

Machine Component	Dimensions	Material
Stator	d=140mm D=250mm	Laminated Steel and Copper
High Speed Rotor:		
Stator Side:	d=140mm D=250mm	
Core	T=12mm	Solid Mild Steel
Magnets	40.5deg T=9mm	N48 $Nd_2Fe_{14}B$
Gear Side:	d=140mm D=320mm	
Core	T=12mm	Solid Mild Steel
Magnets	45deg T=12mm	N48 $Nd_2Fe_{14}B$
Flux-	d=140mm D=320mm	
Modulator	10.1deg T=10mm	Laminated Steel
Low Speed Rotor:	d=140mm D=320mm	
Core	T=5mm	Laminated Steel
Magnets	8.1deg T=7.6mm	N48 $Nd_2Fe_{14}B$

Table 5.2: Electrical Design Specifications

Machine Component	Torque [Nm]	Axial Force [N]
High-Speed Rotor	100	-6000
Modulation Pieces	-800	-6000
Low-Speed Rotor	700	12000

5.3.1 Shaft

In order to keep the number of bearings to a minimum it is decided to keep the shaft stationary. Figure 5.2 and Table 5.3 illustrates the maximum forces that the shaft will endure. The radial force components are mainly due to the weight of the different components, while the axial forces and the torque are due to electro-magnetic forces.

With the maximum forces on the shaft known; a stress analysis is performed in Autodesk Inventor 2009 to determine the deformation of the shaft. This can be seen in Figure 5.3. The maximum deformation is not even 7μm and the safety factor is calculated to be $n = 8.7$. This means that the shaft is rigid enough and more than strong enough.

5.3.2 Bearing Calculations

To facilitate the relative motion between the components, both the high- and low-speed rotors need bearings. The high-speed rotor is sandwiched in-between the stator and the flux-modulator, this leaves little room for mechanical strengthening. To overcome this problem it is decided to support the high-speed rotor with a sealed double-row angular contact ball bearing. A double-row angular contact ball bearing consists of two back-to-back angular contact bearings, which allows for stability and strength

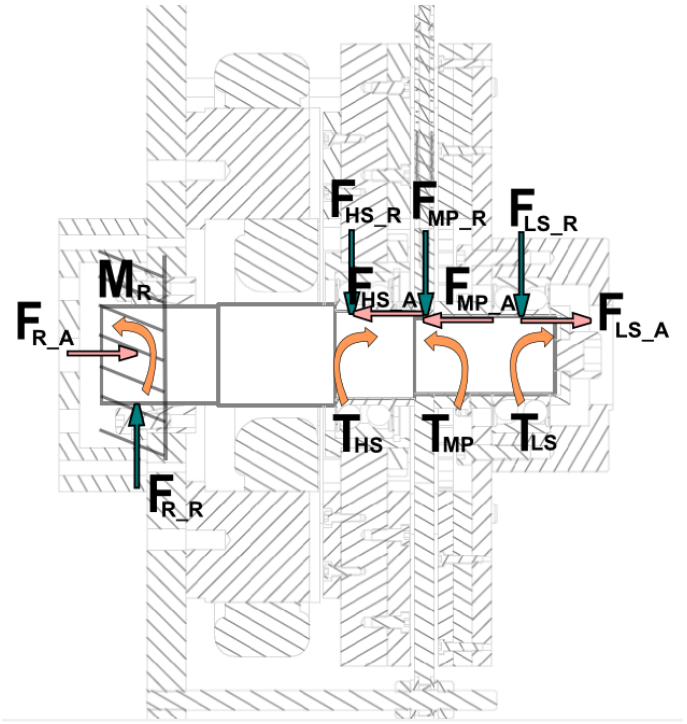

Figure 5.2: Forces Distribution on the Shaft

Table 5.3: Shaft Forces

Component	Torque [Nm]	Axial Force [N]	Radial Force [N]
Self-Centring Lock	Bending Moment $M_R = 68.8$	$F_{R_A} = 0$	$F_{R_R} = 500$
High-Speed Rotor	$T_H = 100$	$F_{H_A} = -6000$	$F_{H_R} = 200$
Flux-modulator	$T_{MP} = -800$	$F_{MP_A} = -6000$	$F_{MP_R} = 120$
Low-Speed Rotor	$T_L = 700$	$F_{L_A} = 12000$	$F_{L_R} = 180$

in the axial- as well as the radial direction. The bearing is also sealed, which allows it to operate for the desired life-span without extra lubrication.

The low-speed rotor is located at the end of the machine which leaves more space for bearings, however to keep conformity in the machine and to reduce the overall size of the machine a sealed double row angular contact ball bearing is chosen for the low speed rotor. To calculate the bearing life the following needs to be known; the equivalent load P, the lubricant operating viscosity v, the dynamic load rating C and the operating speed n. To calculate the equivalent load P of the bearings the following equation is used,

$$P = XF_r + YF_a \tag{5.1}$$

where F_r is the radial load, F_a the axial load, X and Y are the radial and the axial load factors, respectively. The values of X and Y are obtainable from the bearing manufacturer (bearing tables). The lubricant operating viscosity is a function of the operating temperature, speed and the type of lubrication

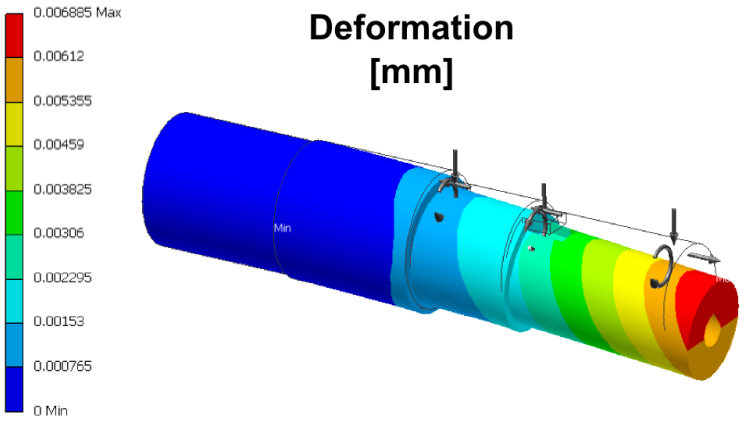

Figure 5.3: Deformation of the Shaft

chosen. In this case the viscosity is standard to the bearing lubrication chosen and is also obtainable from the bearing manufacturer. With all the coefficients known, the bearing life can be calculated. The rated life for the high speed bearing is 4130 hours and for the low speed bearing 1830 hours. For a lab prototype this is more than enough operating hours before replacement is necessary.

The bearing losses is calculated with SKF's frictional moment or power loss calculator (101). The results show that the high-speed bearing has a loss of 5.64 W at rated speed and the low-speed bearing 0.683 W.

All the bearing results is summarised in Table 5.4.

5.3.3 High-Speed Rotor

There are two high speed rotor configurations that need to be designed. The first is where the gear part of the machine is magnetically decoupled to the generator and the second is where it is magnetically coupled. This is accomplished with two different rotor cores. The first core is just a solid steel core

Table 5.4: Bearing Calculations Summary

Component:	**High Speed Bearing:**	**Low Speed Bearing:**
Bearing	3209 A-2RSI/MT33	3208 A-2RSI/MT33
Inner Diameter d [mm]	45	40
Outer Diameter D [mm]	85	80
Basic Dynamic Load C [kN]	51	47.5
Equivalent Dynamic Load P [kN]	8.12	18.7
Operating Speed n [r/min]	1000	150
Lubricant Viscosity	20.1	20.1
Basic Rating Life L_{10} [Mrev]	250	16
Rating Life L_{10h} [operating hours]	4130	1820
Power loss N_R [W]	5.64	0.683

where the permanent magnets are arranged 60 degrees out of phase with each other (see Figure 5.4). The magnets are arranged by rotating all of the magnets on the stator side by 60 degrees, which will force the magnetic fields to turn around in the rotor and not to go all the way through.

The second configuration is where the rotor core is cut in-between the magnets. This will force the magnetic fields to go through the rotor core from the gear side to the stator side (see Figure 5.5).

To switch between the rotor configurations the lock nut is simply unscrewed and the old rotor core is replaced with the new one.

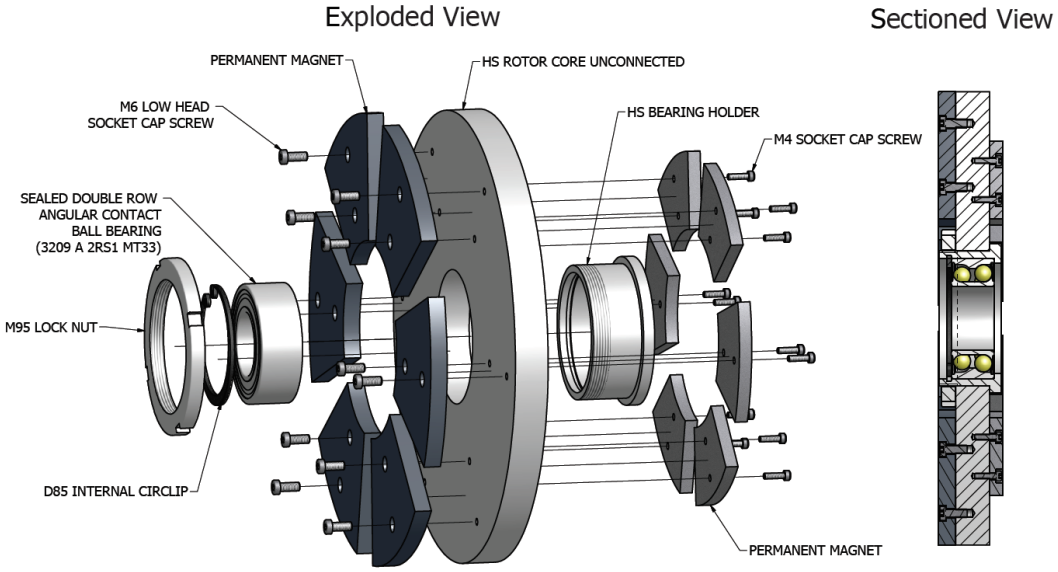

Figure 5.4: High-Speed Rotor with Exploded and Sectioned Views (Magnetically Uncoupled)

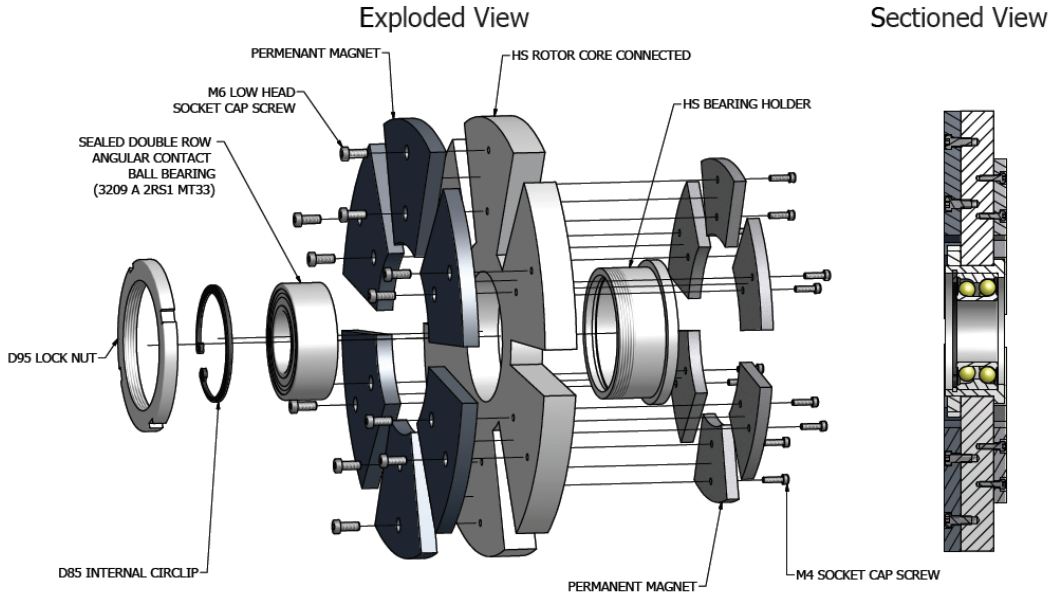

Figure 5.5: High-Speed Rotor with Exploded and Sectioned Views (Magnetically Coupled)

5.3.4 Flux Modulator

The flux-modulator is manufactured from laminated steel to reduce electrical losses. This significantly complicates the mechanical design. It is found in (92) that in radial magnetic gears the flux modulation pieces can be connected with a thin bridge. This closes the slot openings, thus reducing the cogging torque, while increasing the mechanical integrity of the component (see Figure 5.6).

In axial-flux machines this is not easy to accomplish. The lamination stacks are not in the same direction as in radial-flux machines. To simplify the flux modulation pieces it is decided to cut laminated squares and stack them together to form a modulation piece. To keep the slope of the component, the pieces are stepped in four sections (see Figure 5.7). A hole is cut in the centre of each square to allow for a stainless steel rod which strengthens the stacked assembly. The rod keeps the lamination squares in place for easy assembly and also strengthens the lamination pieces, both in the axial and the radial directions. For further strengthening it is decided to cast the full lamination assembly in an epoxy resin and to support the component from the inner as well as the outer diameter.

The axial force on the complete assembly is calculated to be F=6000N (see Table 5.2). To calculate the force on the individual strengthening rods the total force is divided by the number of rods $F_{rod} = \frac{6000}{23} \approx 261$ N. Inventor 2009 Stress Analysis is used to calculate the deformation and the safety factor for the strengthening rods. As mentioned above, both the inner and outer diameter of the modulation pieces are supported, from this it can be assumed that both ends of the rods are fixed. Figure 5.8 is a

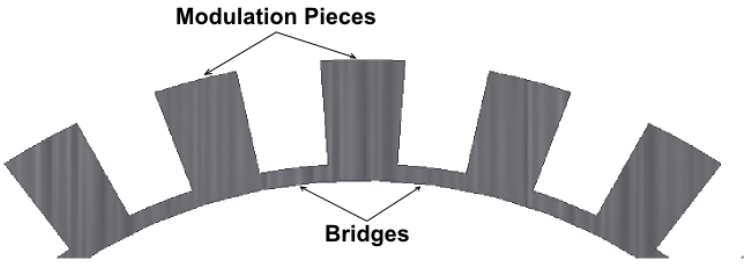

Figure 5.6: Radial Flux Modulation Pieces with Connecting Bridges

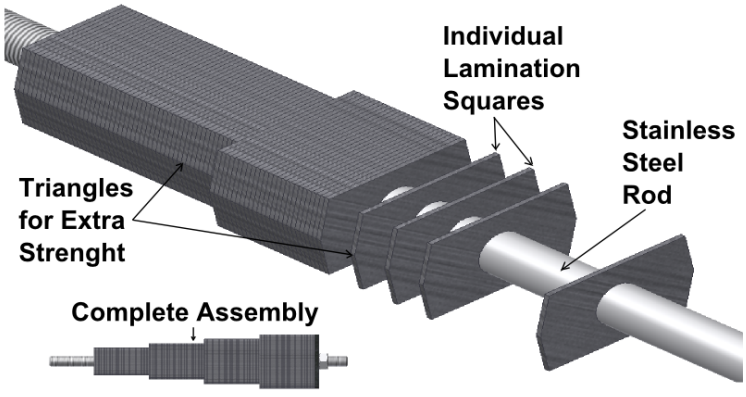

Figure 5.7: Stepped Lamination Stack with Stainless-Steel Rod for Strengthening

visualisation of the deformation and the safety factor of the rods. It can be observed that the rods have a safety factor of 1.4 and a maximum deformation of 0.115 mm which occurs in the middle of the rods.

The strengthening rods are made of stainless steel which is not magnetically conductive, but they are still electrically conductive. This means that the rods can form an electrical circuit if connected at the inner as well as the outer diameter with an electrical conductive material. To avoid further losses it is decided to connect the rods at the inner diameter to an aluminium support and to cast the outer diameter with the epoxy resin mould. The outer diameter of the mould is strengthened with steel rings, but it

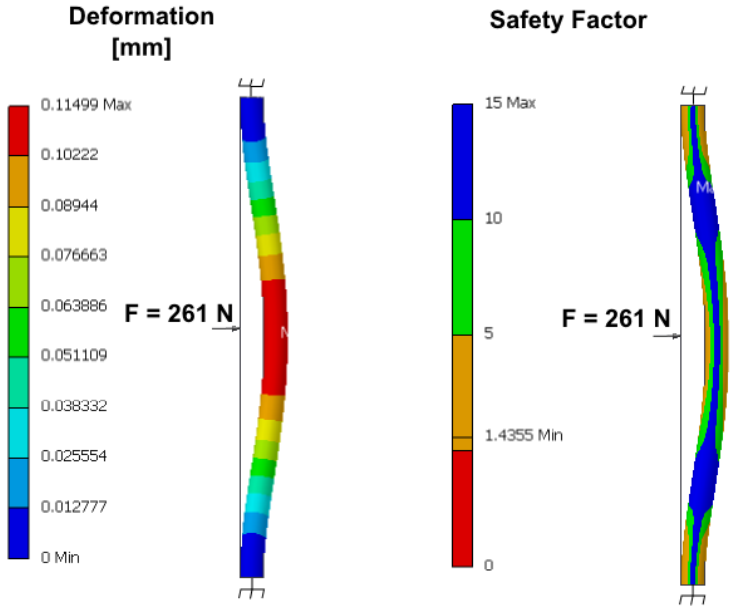

Figure 5.8: Deformation and Safety Factor for the Modulation Pieces Strengthening Rod

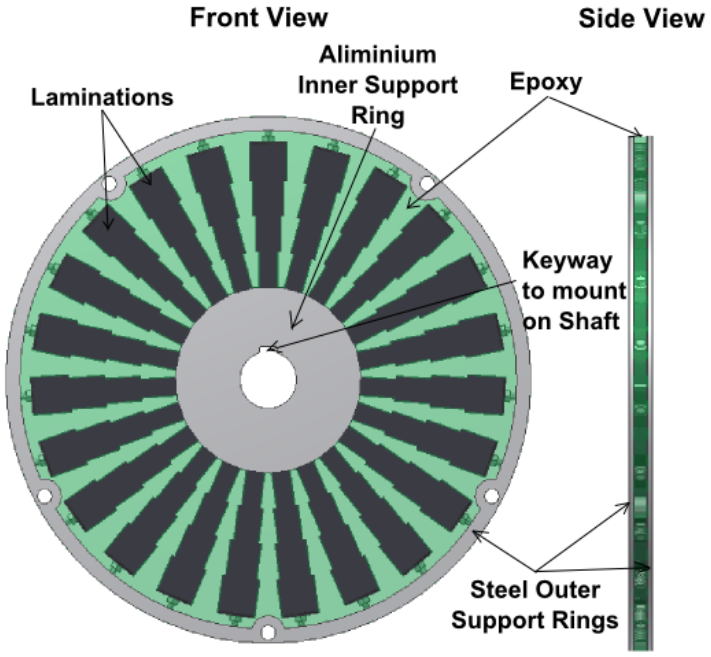

Figure 5.9: Complete Assembly of Modulation Pieces

is connected to the stainless-steel rods with the epoxy resin. Figure 5.9 shows the complete lamination assembly and Appendix B shows the flux-modulator assembly photos taken.

5.3.5 Low-Speed Rotor

The low-speed rotor core needs to be laminated steel to minimise losses, which increases the complexity of the mechanical design. The laminated core is not strong enough on its own, which is why it is decided to mount the laminated core on a solid steel back plate (see Figure 5.10). This back plate strengthens the low-speed rotor and allows for space to connect a bearing holder. A strength analysis is performed on the backplate to ensure that it will be strong enough and that it won't deform (see Figure 5.11). From the analysis it is found that the backplate has a safety factor of 2.2 and the maximum deformation can be seen in the figure, which yields a maximum deformation of 0.22 mm at the outer diameter of the backplate. The bearing holder also has a propshaft connection point, since the low-speed rotor is the input rotor.

5.4 Assembly of Machine Components

Careful consideration should be taken when assembling the machine components, since the attraction force caused by the permanent magnets could deform or break the critical components. It is also extremely difficult to remove a PM rotor when it sticks to a component or when the air-gap between a PM rotor and another component is too small. To ensure that the correct air-gaps are upheld, spacers are used in-between the PM rotors and the flux-modulator. In Figure 5.12 the exploded view of the full assembly is illustrated. The air-gap in-between the high-speed rotor and the stator are controllable with the help of the shaft-positioning-hub and the self-centring-lock. The distance is controlled with a bolt that screws into the shaft-positioning-hub and another smaller bolt that screws into the shaft. When the distance needs to be enlarged the self-centring-lock is loosened and the bigger bolt is used to push the

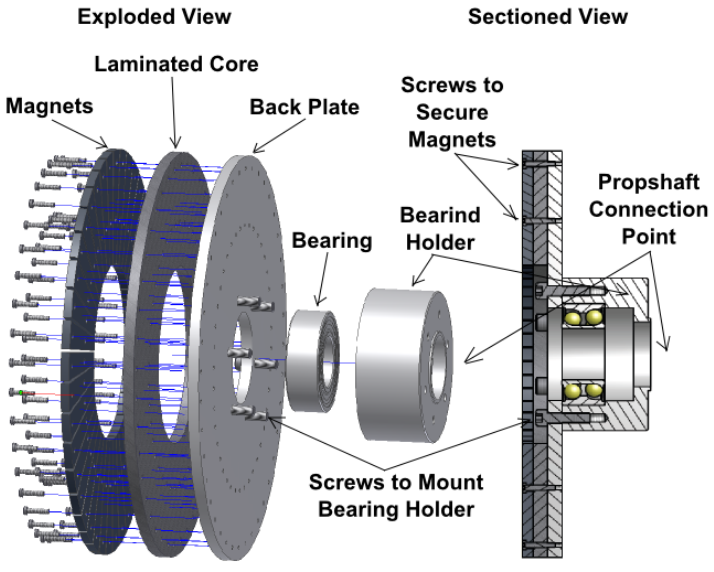

Figure 5.10: Low-Speed Rotor with Exploded and Sectioned Views

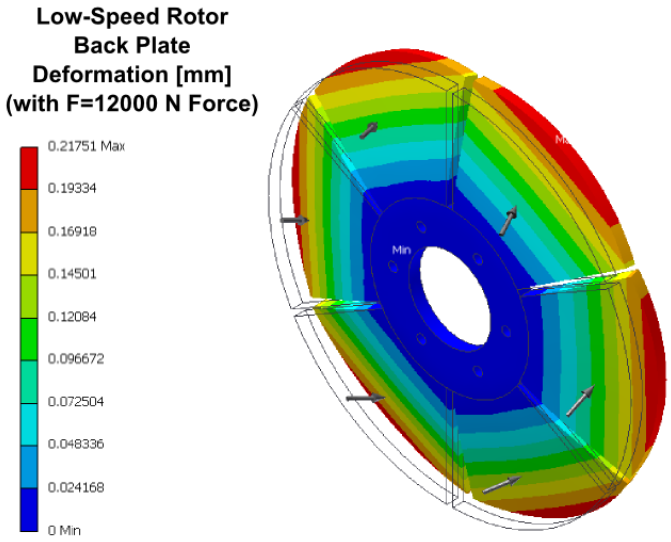

Figure 5.11: Low-Speed Rotor Back-Plate Deformation

shaft away. To decrease the distance of the stator air-gap the smaller bolt is used, which screws into the shaft and can freely rotate on the shaft-positioning-hub, the screw is then tightened to pull the shaft closer.

Thin aluminium plates that are of the same thickness as the air-gap distances are used as spacers in the air-gaps to ensure that the air-gaps will be the correct distance and that the rotors can not bend and stick to the other components. Figure 5.13 shows the complete MGAFG assembled machine on the test bench.

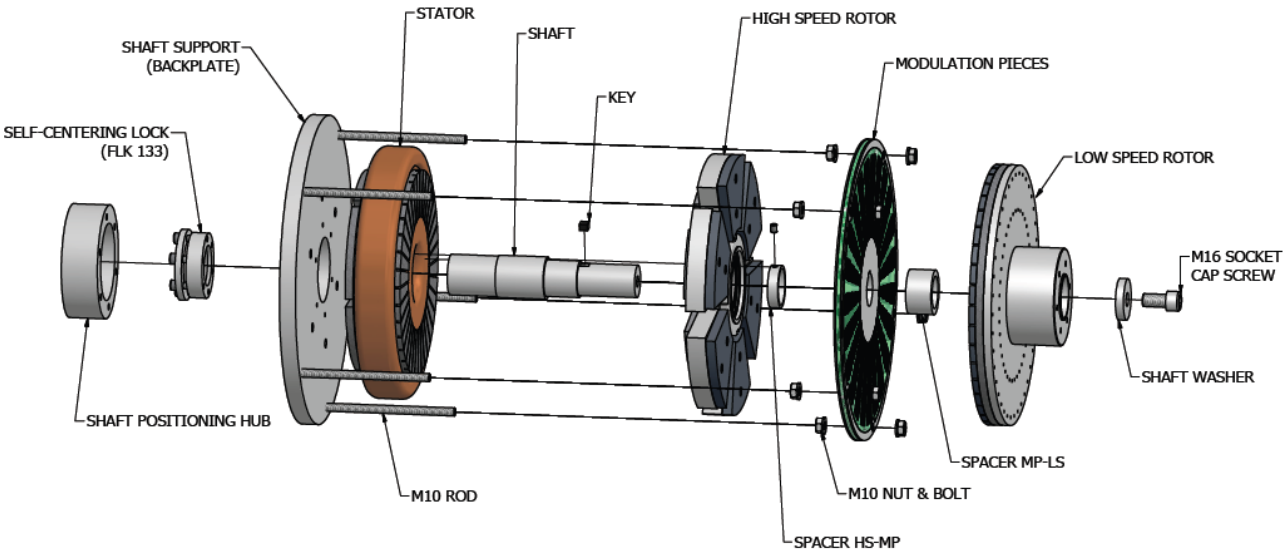

Figure 5.12: Full Assembly Exploded View

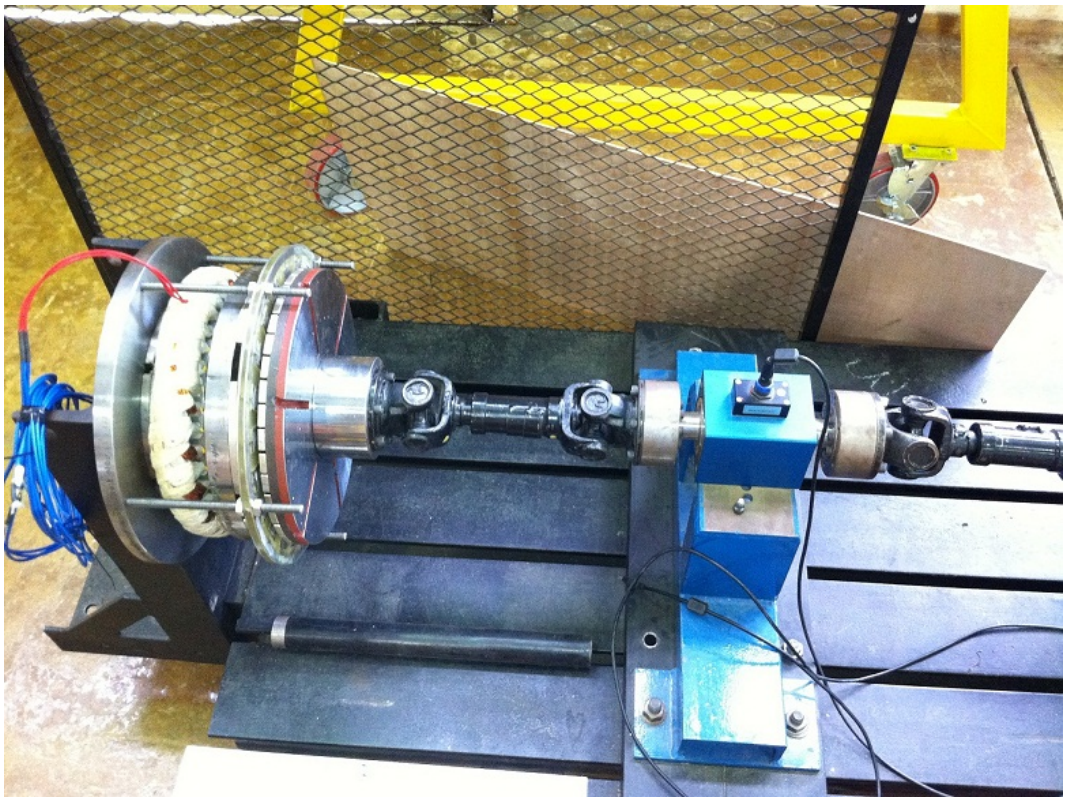

Figure 5.13: Complete MGAFG Assembled Machine on the Test Bench

CHAPTER 6

EXPERIMENTAL EVALUATION

In this chapter the experimentally evaluation of the MGAFG prototype is described and the measured results are discussed. All tests on the machine were performed at the Stellenbosch University Electrical Machines Research Laboratory.

6.1 Test Set-up

The test bench set-up consisted of the following:

- A 4-pole 55 kW *English Electric* induction motor. The motor drove the prototype machine at the desired speed and/or torque to simulate the input power of the wind on the turbine blades.
- An *Allan Bradley* variable speed drive (VSD). The drive controlled the motor at the desired speed and/or torque.
- A *Lorenz* torque sensor was used to measure the input speed (ω_L) and the input torque (T_L), with which the input power (P_{in}) was calculated. The measured data was logged via a USB 2.0 connection and stored on a Laptop PC.
- Two prop shafts were connected between the induction drive motor, the torque sensor and the MGAFG prototype. These prop shafts have the advantage of not needing precise alignment and losses are small and negligible.
- A *Fluke* infra-red temperature camera that captured temperature distribution of the prototype. The components with high temperature rise are those where losses are most likely to occur.
- A *Brockhaus Messtechnik* Model 410 Gaussmeter, which measured the flux-density in the prototype air-gap, to compare simulated and measured results.
- Various other pieces of test and measurement equipment: oscilloscopes, multimeters and a 3-phase resistor-bank.

Figure 6.1 shows the test bench and some of the equipment used to test the prototype.

Due to the large axial forces, as a conservative measure, the air-gaps of the prototype were increased to 4mm, which is twice as much as the designed value. This was done as a precaution to get preliminary results and thus to ensure that the machine did not suffer premature failure.

To verify the air-gap size 4mm aluminium plates were used as spacers in the air-gaps during assembly (see Figure 6.2). The air-gap size may however be slightly bigger than 4mm, since the plates still needed to be removed after the machine had been assembled.

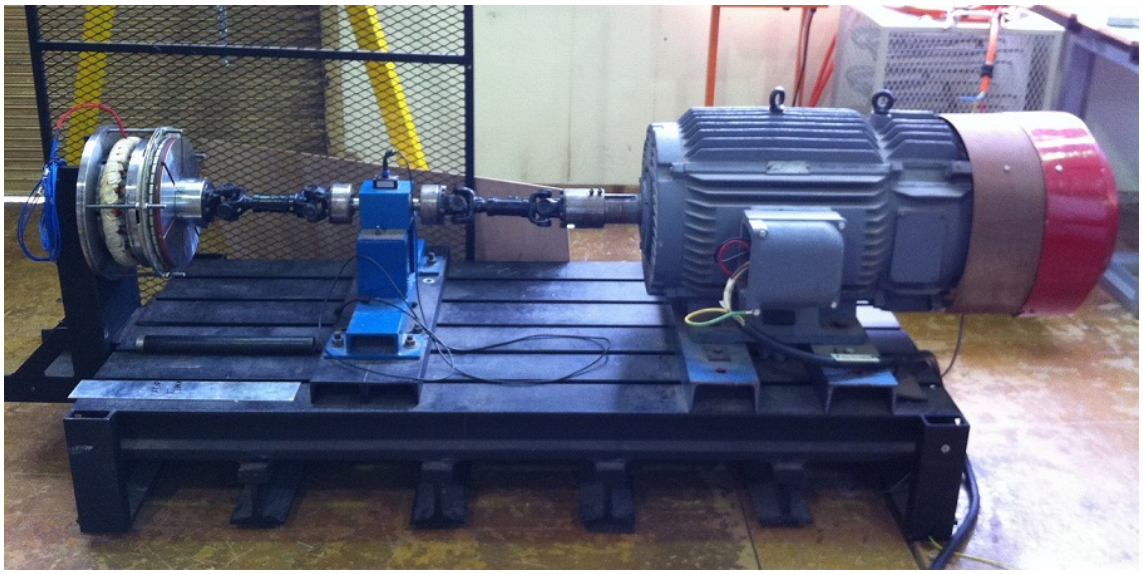

Figure 6.1: Test Bench

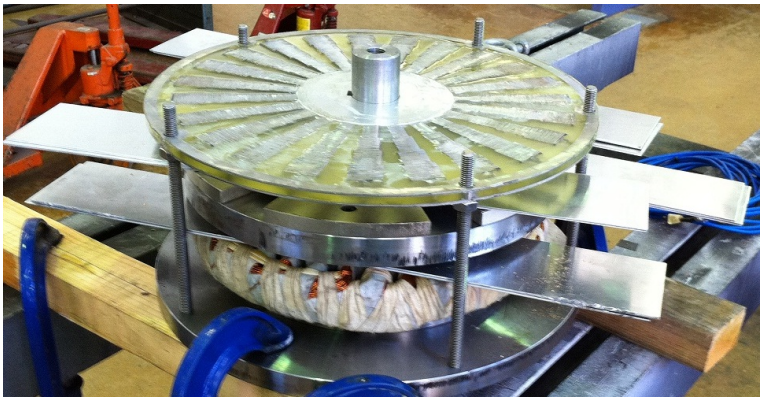

Figure 6.2: Assembly Process to Ensure Correct Air-Gap Sizes

After assembly it was found that the low-speed rotor was not rigid enough. The double angular contact ball bearing's internal clearance allowed for some movement; thus, the low-speed rotor vibrated when in operation. However, due to time restrictions it was decided to keep the machine as was and do the tests with the increased air-gaps. (Appendix C gives an alternative bearing configuration, which may solve the vibration issues.)

The machine was first tested for the decoupled configuration and then for the coupled configuration.

6.2 MGAFG with Decoupled Configuration Experimental Results

6.2.1 No-Load Losses

The first test was performed to measure input mechanical power versus the input speed of the machine. With this test the no-load losses of the machine at different speeds were observed (see Figure 6.3). The torque sensor used takes 2500 samples per minute, thus in the figure a second order polynomial trend line is added to show the trend of the losses.

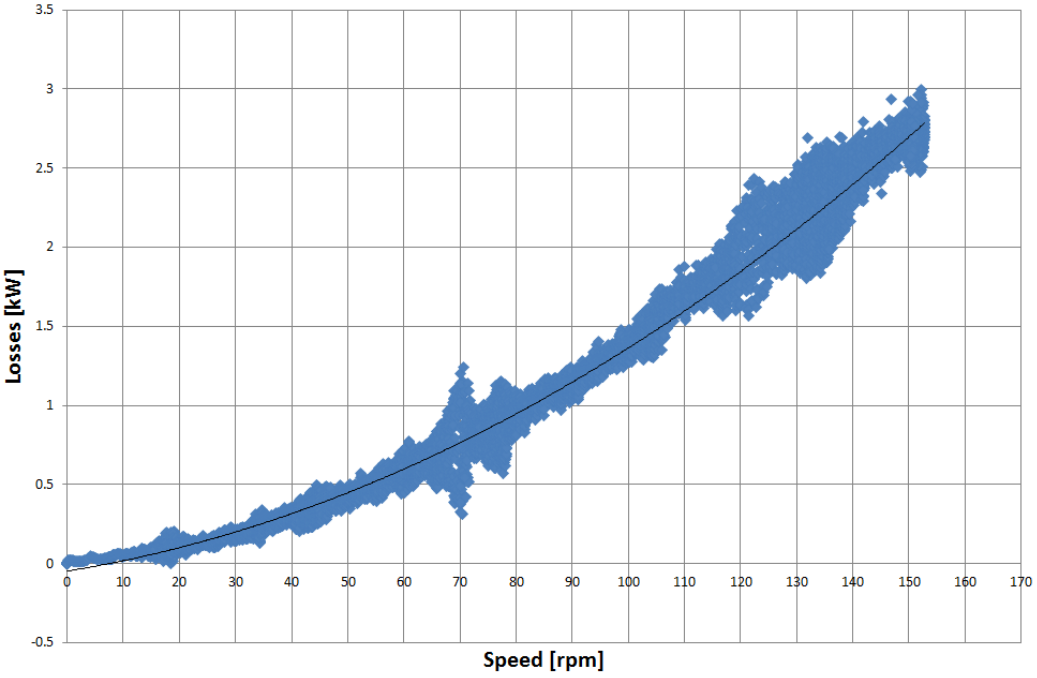

Figure 6.3: No-Load Losses versus Input Speed

From Figure 6.3, it is observed that for rated input speed (150rpm) the losses of the machine are almost 2.7 kW.

Since the high losses were not predicted in the simulated results, it is important to identify the cause of the unknown losses. An infra-red camera was used to measure the temperature of the different components. The component with a high temperature should be a source of the high losses. Figure 6.4 represents the temperature measurement of the machine, in which it is evident that the low-speed rotor is much warmer than the rest of the components, especially the backplate of the low-speed rotor. Thus, there are significant losses in the backplate of the low-speed rotor.

The low-speed rotor has a laminated core, which is mechanically strengthened with a solid steel backplate. The backplate was not simulated in the electromagnetic design; it was only considered in the mechanical design to ensure the strength of the low-speed rotor. The low-speed rotor's laminated steel core is 10mm thick, which is highly saturated with the PM flux. It is seen in an FE model that the PM flux path still protruded through the laminated core into the solid backplate (see Figure 6.5).

Figure 6.6 shows 2D transient FEM simulation results to determine the ohmic losses of the low-speed rotor backplate. The low-speed backplate was also simulated in 3D, which closely corresponds to the 2D simulated results. The ohmic losses of the low-speed rotor backplate settle at about 530 W.

To quantify the high loss components a number of simulations were performed and are summarised in Table 6.1. From the table it is observed that the total simulated losses of the machine is 805.121 W. This is still lower than the measured results.

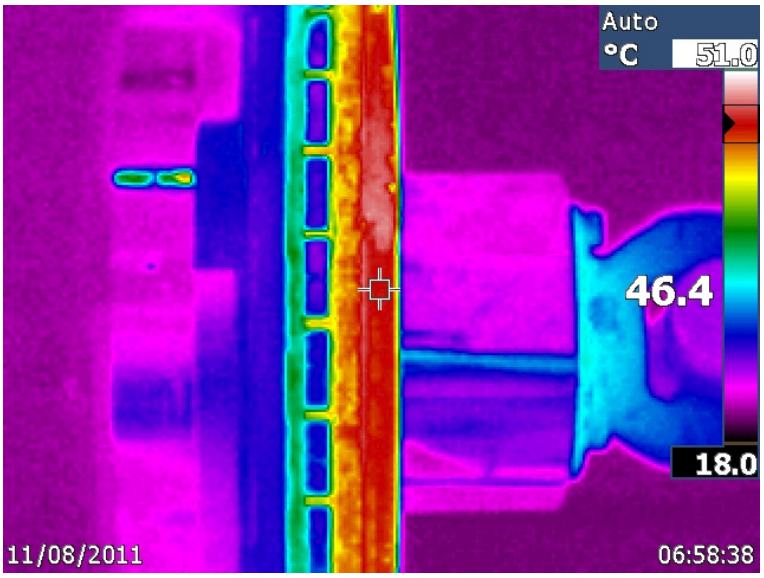

Figure 6.4: Temperature Measurement of the Machine to Identify the Loss Component

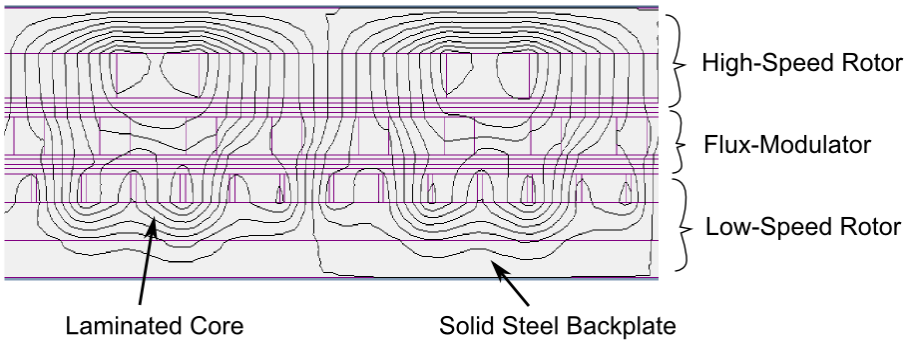

Figure 6.5: Flux Line Drawing to Illustrate Flux Protruding into the Low-Speed Rotor's Solid Steel Backplate

Apart from the windage and bearing losses, the underestimated losses may be attributed to the following aspects:

- The low speed laminated core were machined to get the rotor parallel and concentric, this compromised the electrical insulation of the laminated core.
- Unparallel discs may have caused additional high harmonics in the low speed rotor.
- Losses may have been caused due to vibration in the low-speed rotor.

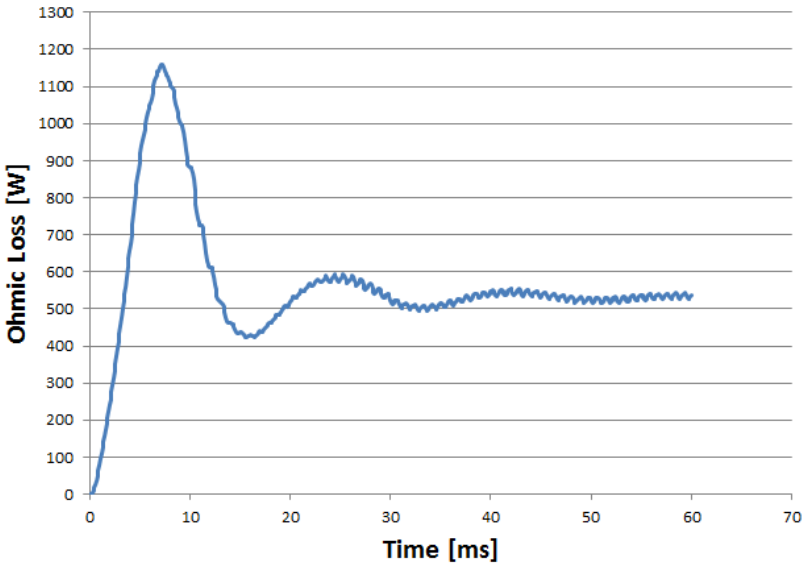

Figure 6.6: Ohmic Losses of Low-Speed Rotor Backplate

6.2.2 No-Load Back EMF

The no-load back EMF waveform for the decoupled MGAFG machine at rated speed is given in Figure 6.7 and the simulate back EMF is given in Figure 6.8. From the figure it is observed that the three phases are balanced. The simulated back EMF is slightly lower than the measured results. The frequency of the machine is calculated by measuring the time it takes to complete one wave form, which is 20ms. Therefore the frequency of the machine at rated speed is 50Hz. With the input speed and the output electrical frequency known the gear ratio of the machine can be determined with Equation 2.12 and 3.5.

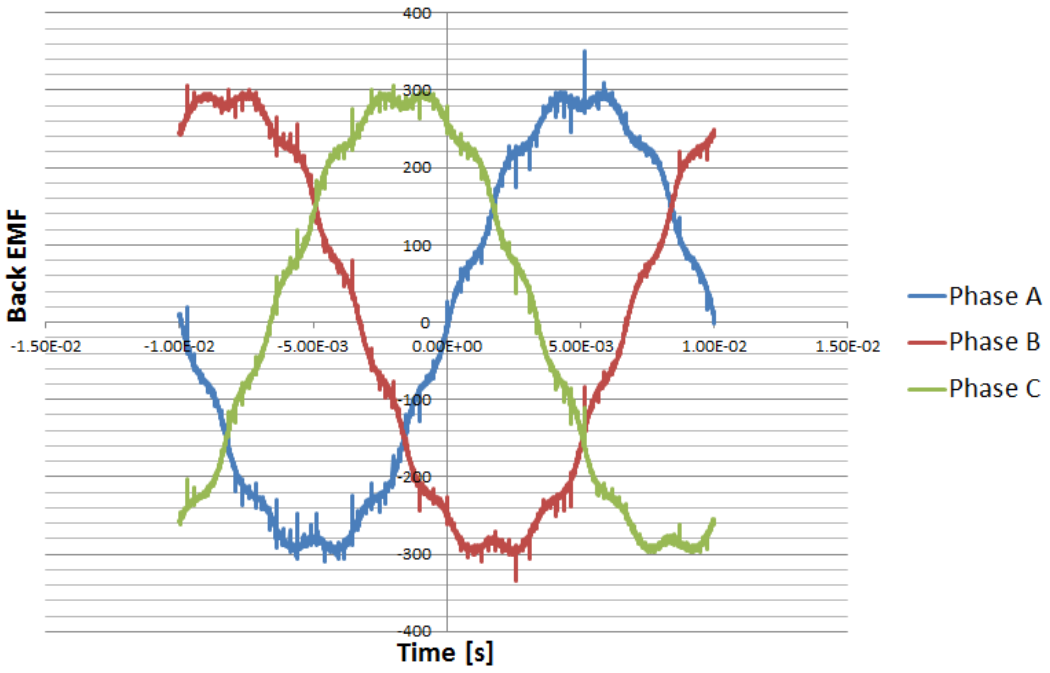

Figure 6.7: Back EMF at Rated Speed

Table 6.1: Losses of MGAFG

Component	Losses per Component [W]	Number of Components	Total Losses [W]
LS Rotor:			
Backplate	530	1	530
Laminated Core (Hysteresis and Eddy)	14.909 + 1.922	1	16.83
Magnets	0.5	40	20
Screws	0.0007	40	0.028
Total			**566.858**
HS Rotor:			
Magnets Gear-Side	25.8	6	154.8
Magnets Stator-Side	3	6	18
Rotor Core	17	1	17
Total			**189.8**
Flux-Modulator:			
Hysteresis	0.8	23	18.4
Eddy Current	0.15	23	3.45
Stainless-Steel Rods	0.008	23	0.184
Total			**22.034**
Stator:			
Hysteresis	23.468	1	23.468
Eddy Current	2.961	1	2.961
Total			**26.429**
MGAFG Total			**805.121**

$$n_H = \frac{60 f_{out}}{p_h} = \frac{60 \times 50}{3} = 1000 rpm$$

The input speed is known to be n_L = 150 rpm. Thus, the gear ratio is determined with:

$$G_r = \frac{n_H}{n_L} = \frac{1000}{150} = 6.667$$

The gear ratio is the same as in the design specifications; therefore the gear action of the machine operates as expected.

Figure 6.9 represents the back EMF peak values of the machine at no load at different speeds for the experimental measurements and for the simulated results. From the figure it is observed that the experimental measurements are a bit higher when compared to the simulated results.

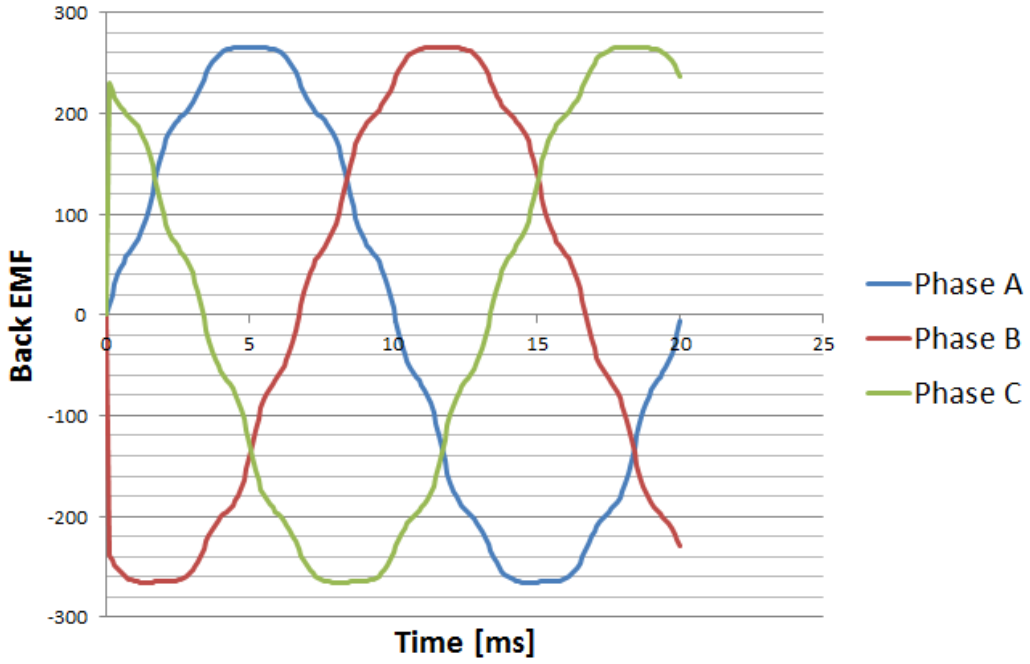

Figure 6.8: Simulated EMF at Rated Speed

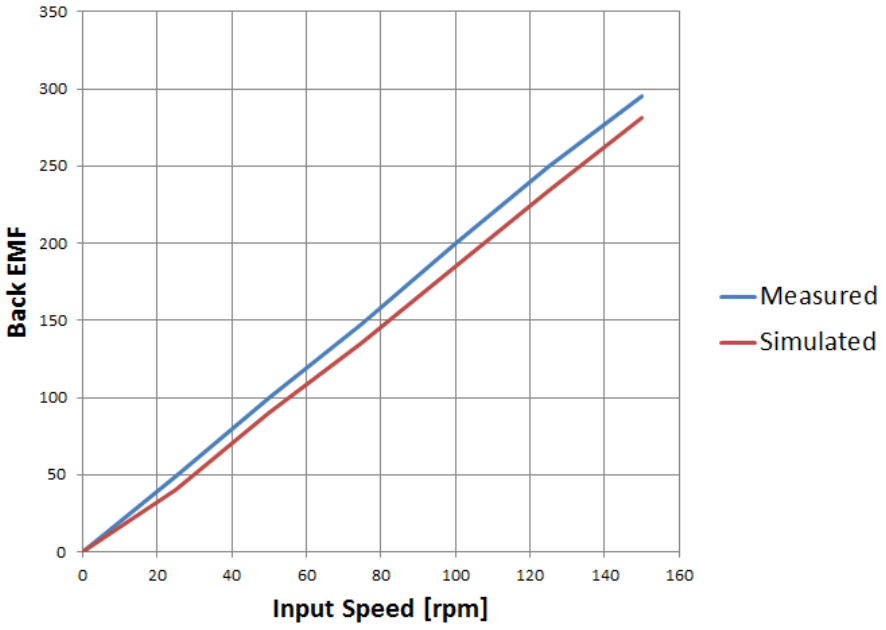

Figure 6.9: Decoupled Back-EMF versus Input Speed

6.2.3 Load Measurements

Since the machine exhibits such high losses in the low-speed rotor backplate, it was decided that the load test should be measured at low speeds, which would keep the losses low. The test was performed between 25rpm and 50rpm, with a three phase 30 Ω load. Figure 6.10 gives the results obtained, namely; the input power and the extracted output power of the machine at different speeds.

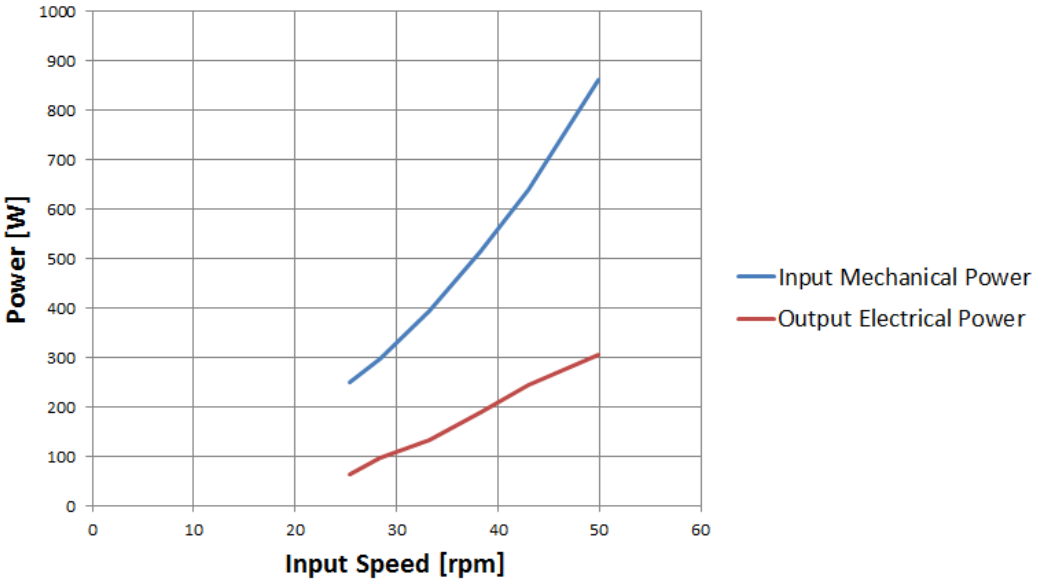

Figure 6.10: Decoupled Load Test

With the results the efficiency at different input speeds are calculated (see Figure 6.11). From the figure it is observed that at an input speed of 50 rpm the efficiency of the machine is 35.5%. The efficiency is low, which is expected, since the losses in the machine are so overwhelming. Since the losses calculated in the simulated results is much lower than in the measured results, the efficeincy of the simulation is 69.4%.

6.2.4 Torque Measurements

For the torque measurements the input torque for the load and no-load tests are measured and analysed. Figure 6.12 illustrates the no-load input torque at rated speed. The average no-load input torque at rated speed is 163.7 Nm with a torque ripple of 8 %.

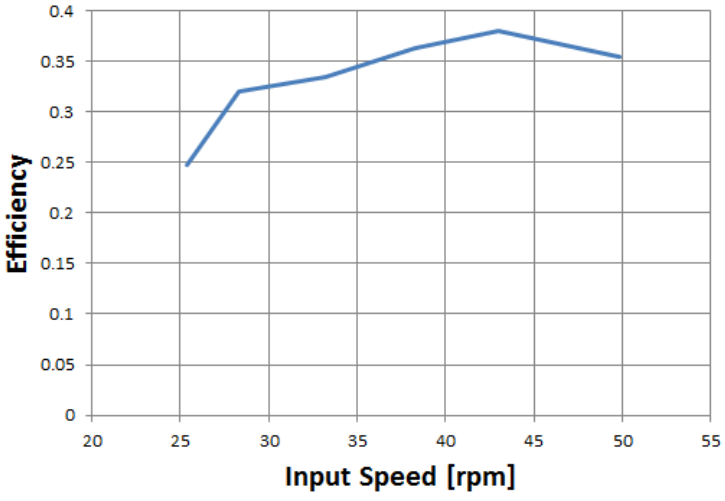

Figure 6.11: Efficiency at Different Input Speeds

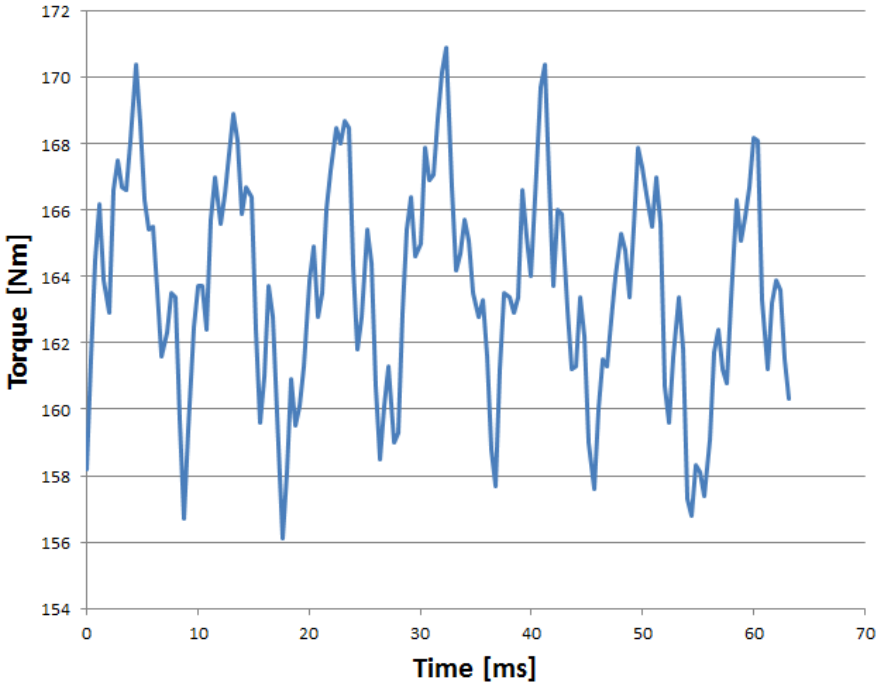

Figure 6.12: No Load Input Torque at Rated Speed

To measure the pull out torque of the prototype the machine is overloaded until the gear part of the machine start to slip. Figure 6.13 illustrates the measured input torque versus time, in which it can be seen that the gear starts to slip at about 17.5 seconds. After the slip point the torque oscillates between positive and negative at a high frequency until the input speed is decreased. The gear slips at just over 200 Nm.

The static pull out torque is measured by locking the high-speed rotor and then rotating the low-speed rotor with a crank until it slips, while measuring the input toque with the torque sensor. Figure

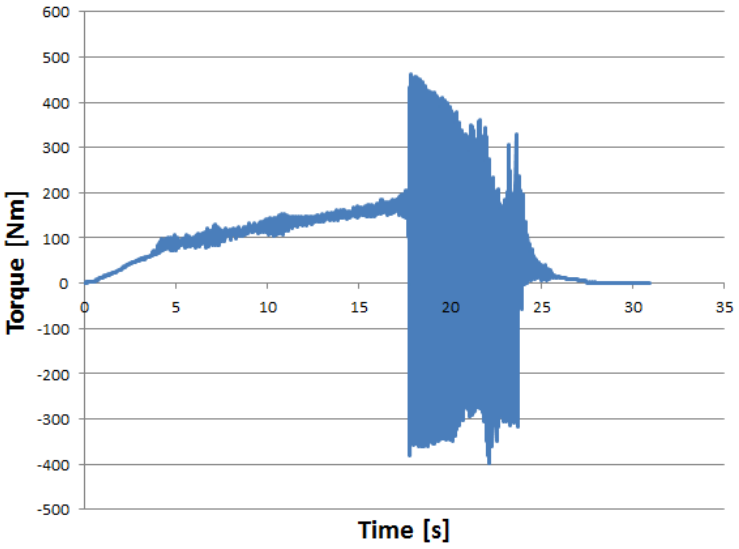

Figure 6.13: Overload Test to Determine Maximum Input Torque of Prototype Machine

6.14 shows the measured torque. From this it can be seen that the static pull out torque is reached at just under 200 Nm, which is very similar to the results obtained for the overload test.

The cogging torque or the input torque before the machine starts to rotate is calculated by taking the average start torque measured in the tests. The cogging torque is calculated to be 48.2 Nm for the decoupled machine.

To quantify the low pull out torque of the prototype a number of simulations are performed. The first simulation is to determine the pull-out torque of the MGAFG machine with the increased air-gaps without considering any losses. This is done to have a bench mark. The torque is calculated to be T_L = 328.996 Nm.

Next the low speed rotor backplate is added. With the backplate the torque decreases with 14.898 Nm.

The next simulation determines the influence of the screws that secure the PMs to the low-speed rotor's backplate. The screws are designed to be non-ferrous stainless steel; however normal steel screws are used to obtain experimental results due to unavailability of stainless steel screws.

To draw the screws in 2D the volume percentage that the screws occupy in the PMs is calculated and then converted to the area percentage. In 2D the screws are drawn in the middle of the PMs with the percentage area calculated that it would occupy in 3D. Figure 6.15 shows a flux plot on the cross section of the screws to show the influence that the steel screws have on the flux-density between the flux-modulator and the low-speed rotor.

From the figure it is observed that the screws form a return path, which decreases the flux-density across the low-speed rotor air-gap. Due to the steel screws used in the low-speed rotor the torque decreases with 20.0672 Nm. For the same reason, the steel screws used in the high speed rotor account for 4.784 Nm reduction of torque.

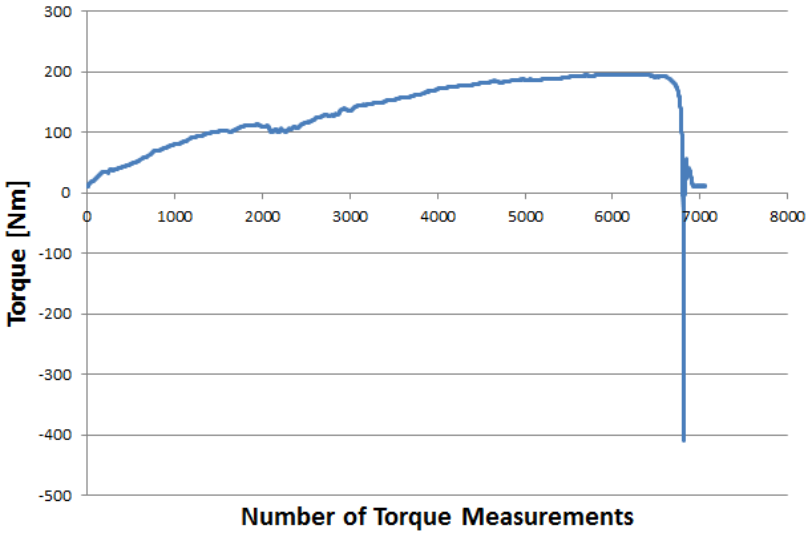

Figure 6.14: Locked High-Speed Rotor Test to Determine Maximum Torque

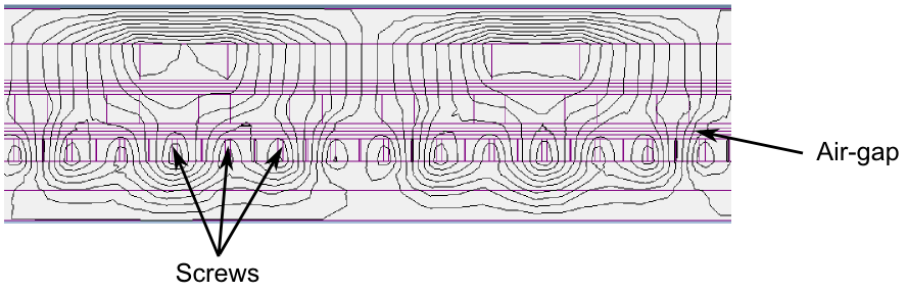

Figure 6.15: Flux Plot to Illustrate the Influence of the Steel Screws on the Flux-Density in the Low-Speed Rotor Air-Gap.

The stainless steel rods used to strengthen the flux-modulator decreases the torque with 40.018 Nm. Thus, with all of these factors the pull-out torque becomes T_L = 249.537 Nm, which is still about 50 Nm higher than the measured results.

The high losses in the low-speed rotor increased the overall temperature of the low-speed rotor; therefore the temperature in the low-speed rotor's PMs also increased. The PMs used on the low-speed rotor are $Nd_2Fe_{14}B$ grade N48 magnets, which may be subject to a certain degree of demagnetisation at an operating temperature of more than $80°C$ (102). The flux-density in the low-speed air-gap was measured with the gaussmeter, to verify if any demagnetisation occurred. From the measurements it was found that the flux-density in the low-speed air-gap was 0.87 T where the 3D simulated flux-density was calculated to be 1.15 T, thus the flux-density decreased by almost 25% when compared to the simulated results. However, the measured flux-density in the high-speed air-gap closely corresponded to the simulated results. The measured flux-density in the high-speed air-gap was 0.68 T and the simulated flux-density was 0.7 T. This means that the flux-density in the low-speed air-gap is lower than it should be. Figure 6.16 shows the flux density representation of the 3D model air gap for the low- and high-speed rotor air gaps. The measurement was taken at spot x in the figure.

The MG was then simulated with lower grade PMs on the low-speed rotor with the same flux-density

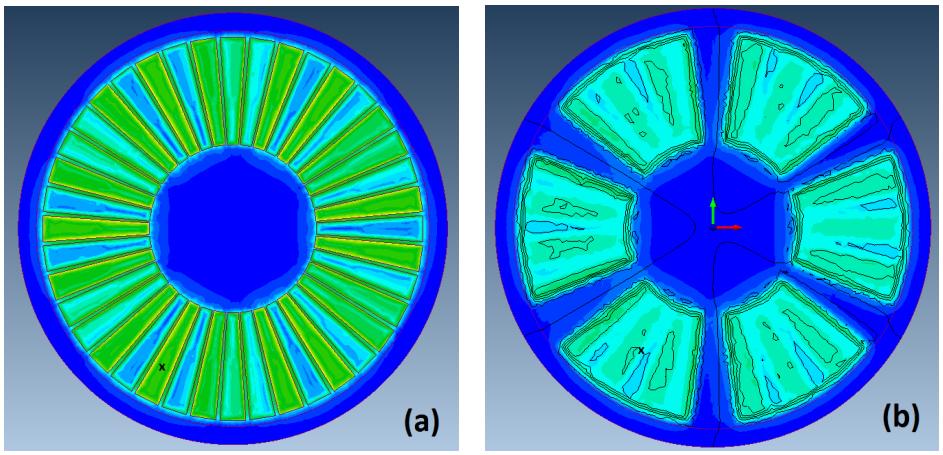

Figure 6.16: 3D Flux-Density Simulated Measurement of the; (a) Low Speed Air Gap and the (b) High Speed Air Gap

in the air-gap as measured in the prototype. The PM grade with the same flux-density is N28 $Nd_2Fe_{14}B$ magnets. The pull out torque reached with the degraded PM simulation is 195.85 Nm on the low-speed rotor, which is similar to the measured values. The decrease in flux-density in the low speed air gap is thus likely also due to the demagnetisation of PMs during the early test ran stage.

6.3 MGAFG with Coupled Configuration Experimental Results

The same tests are performed on both the coupled machine and on the decoupled machine, to investigate the difference in performance for the two configurations.

6.3.1 No-Load Losses

The first test calculated the input power for the machine at different speeds (at no-load), this is done to investigate the losses of the machine at different speeds. Figure 6.17 indicates the losses of the machine at different input speeds. From this figure it is observed that the coupled machine has similar losses as the decoupled machine at rated speed.

6.3.2 No-Load Back EMF

Figure 6.18 shows the no-load back EMF results obtained at rated speed and Figure 6.19 shows the simulated results. From the measured results it is observed that the no-load back EMF is similar to that of the decoupled machine, however the simulated results is slightly higher.

The period of one wave form is 20ms, thus the machine operates at 50Hz for the rated input speed of 150rpm. Therefore the gear ratio for the coupled machine is G_r = 6.667.

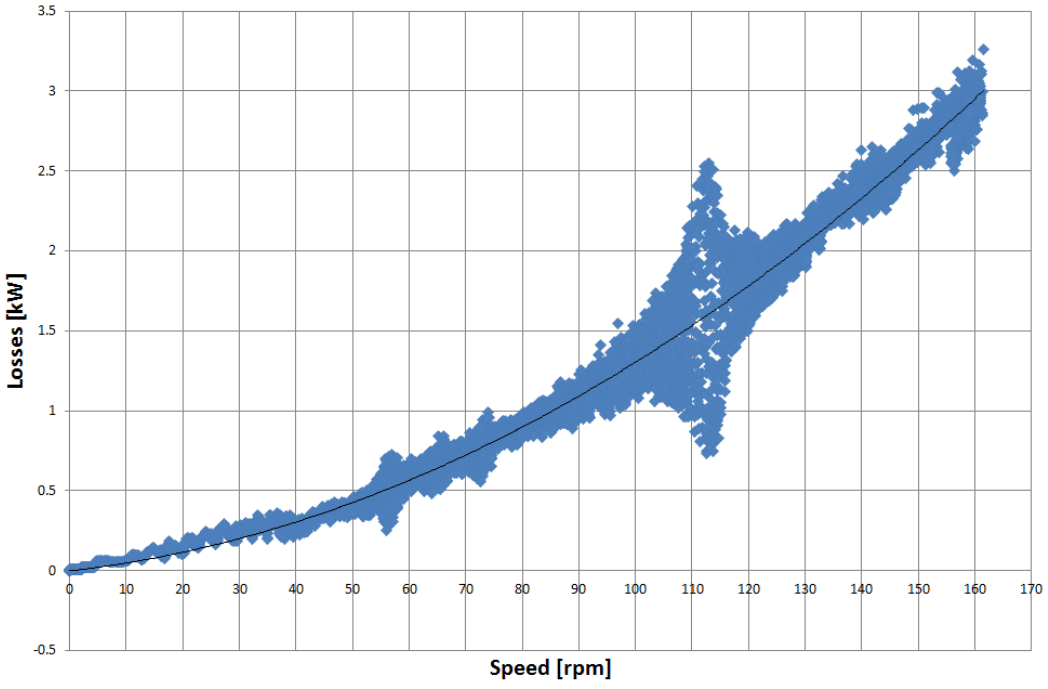

Figure 6.17: Coupled No-Load Losses versus Input Speed

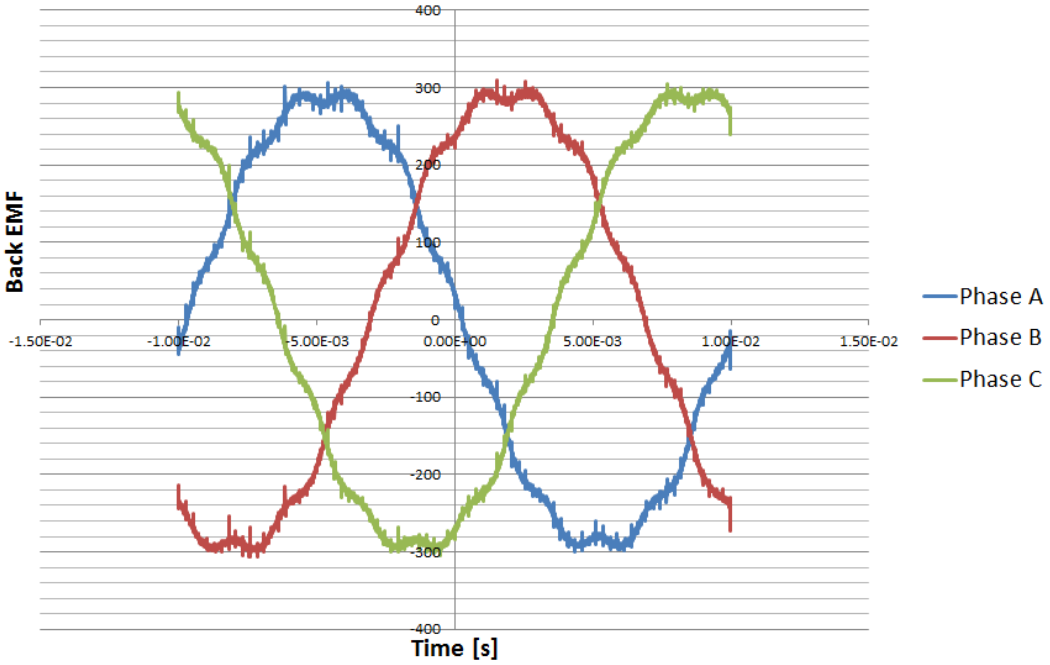

Figure 6.18: Coupled Back EMF at Rated Speed

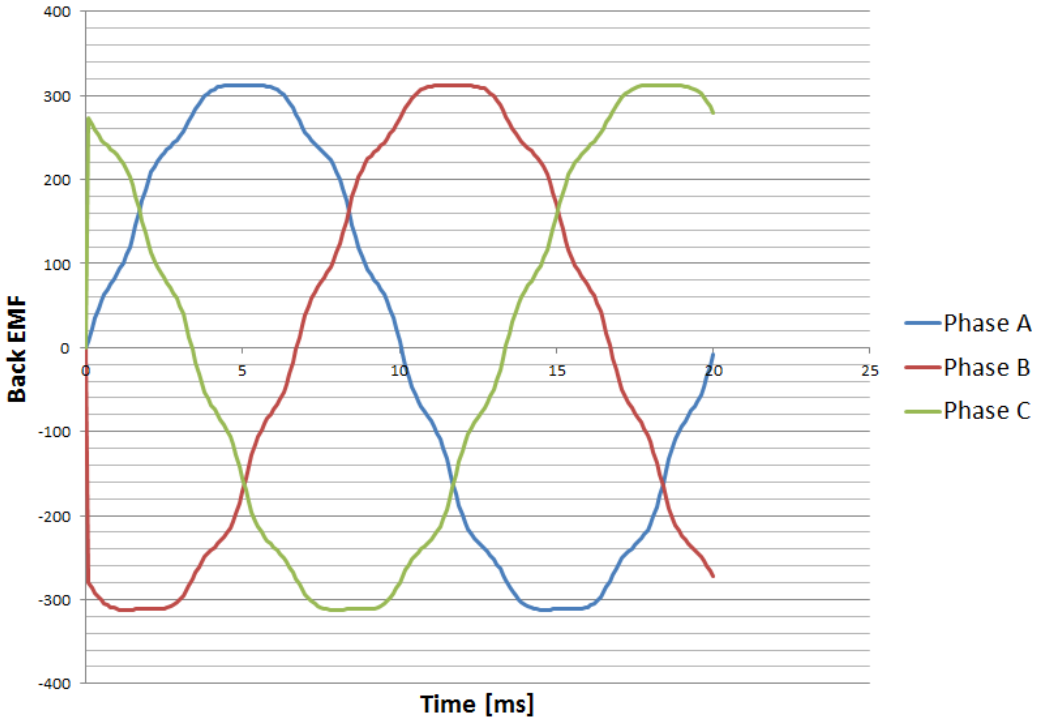

Figure 6.19: Coupled Simulated Back EMF at Rated Speed

Figure 6.20 shows the measured and simulated peak values for the back EMF at different speeds. The simulated results is slightly higher than the measured results.

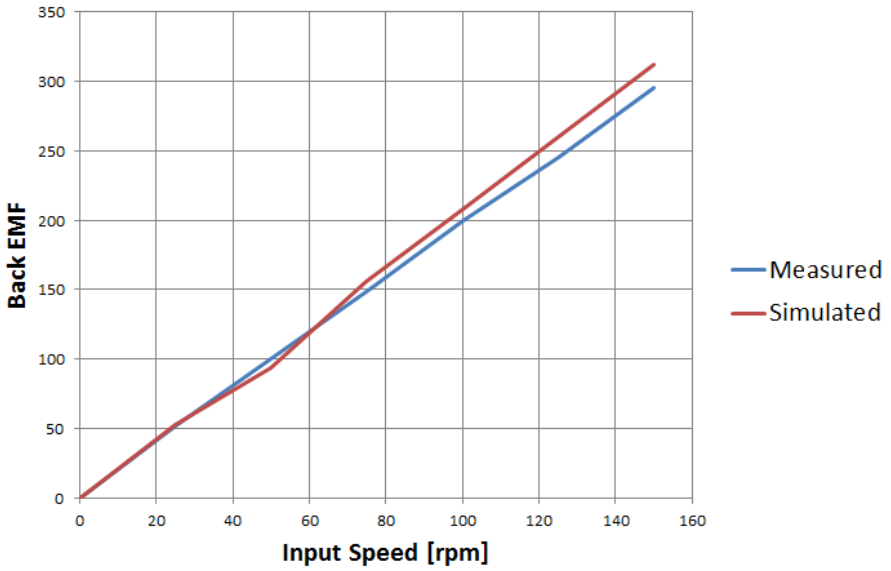

Figure 6.20: Coupled Peek Back EMF versus Input Speed

6.3.3 Load Measurements

The coupled load measurements were performed at low speeds (from 25rpm to 50rpm) to reduce the influence of the high losses. Figure 6.21 illustrates the mechanical input power and the electrical output power of the machine at different speeds. The results obtained are very similar to the decoupled results.

The efficiency of the coupled machine at 50rpm (see Figure 6.22) is higher when compared to the decoupled machine. The efficiency of the coupled machine is 37.5% and the efficiency of the decoupled machine is 35.5%. Thus, the coupled configuration has a 2% higher efficiency when compared to the decoupled configuration.

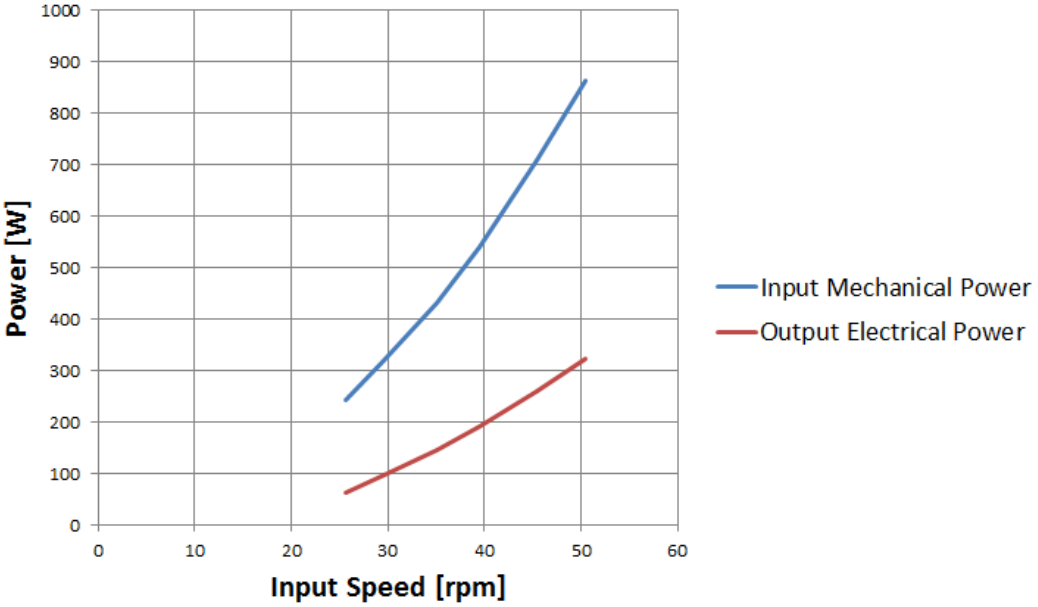

Figure 6.21: Coupled Load Test

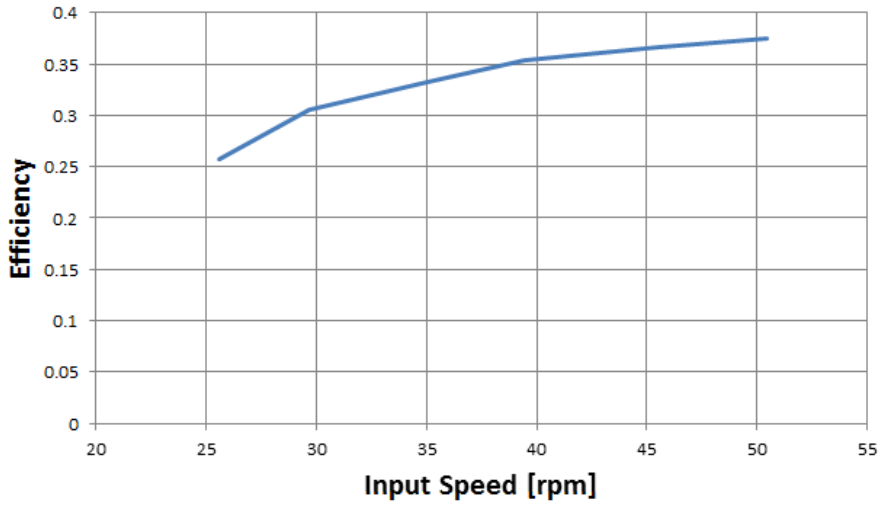

Figure 6.22: Coupled Efficiency at Different Input Speeds

6.3.4 Torque Measurements

Figure 6.23 illustrates the no-load input torque at rated speed. The average no-load input torque at rated speed is 166 Nm with a torque ripple of 8.7 %, which is very similar to the no-load torque for the decoupled configuration.

Next the cogging torque is calculated for the coupled configuration by taking the average start torque for all the tests performed. The average cogging torque is calculated as 47.7 Nm, which is slightly lower than for the decoupled configuration.

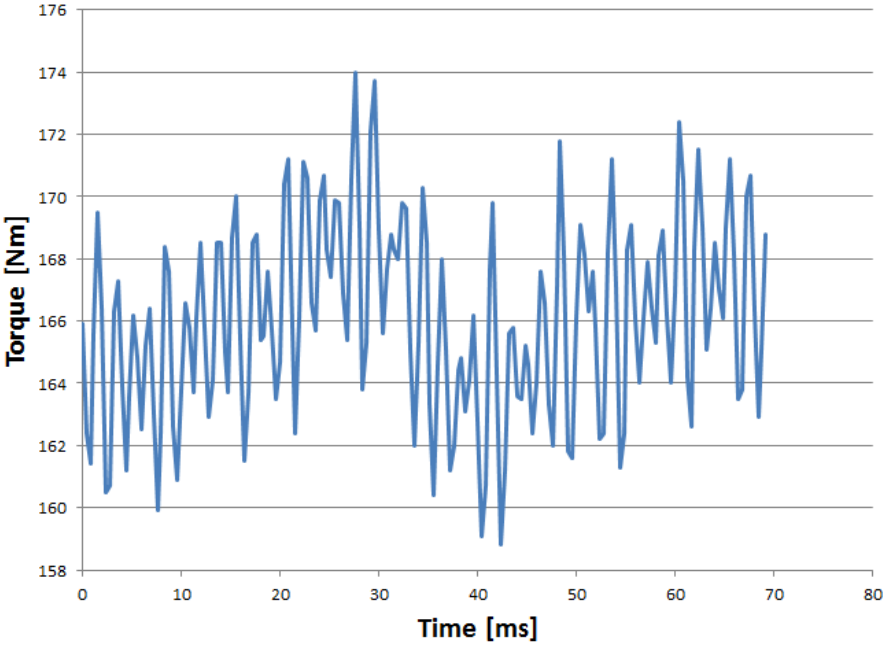

Figure 6.23: Coupled No-Load Input Torque at Rated Speed

The pull out torque is determined for the coupled configuration in the same manner as for the decoupled configuration, by overloading the machine until the gear starts to slip (see Figure 6.24).

The pull out torque was also measured by locking the high-speed rotor and rotating the low-speed rotor until the rotor started to slip (see Figure 6.25)

From both tests it is observed that the maximum torque on the low-speed rotor is just under 200 Nm for the coupled configuration, which is similar to the results obtained for the decoupled configuration.

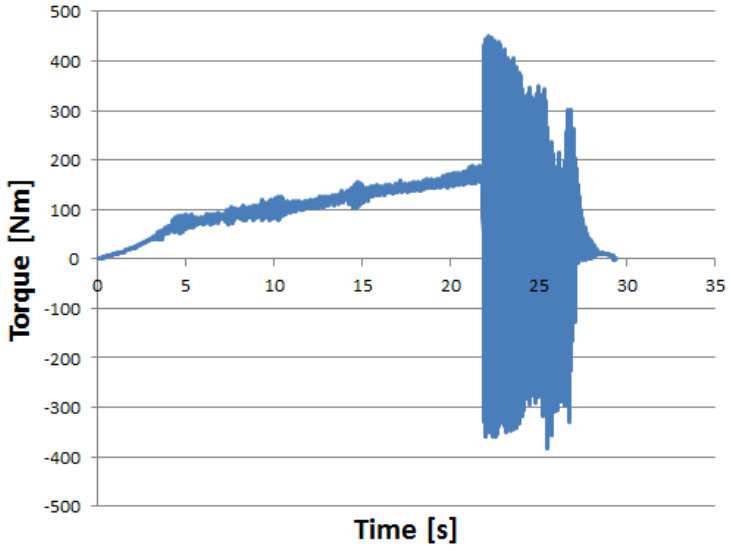

Figure 6.24: Overload Test to Determine Maximum Input Torque of Coupled Configuration

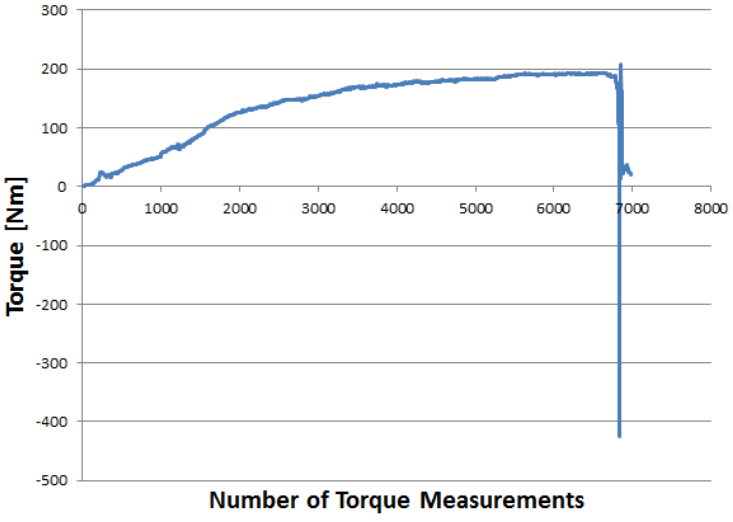

Figure 6.25: Locked High-Speed Rotor Test to Determine Maximum Input Torque

6.4 Conclusion

Table 6.2 lists the summarised results obtained in the experimental and simulated evaluations for the decoupled and coupled configurations. For the simulations the input current density is adjusted to produce the same output power as in the measured results (the simulated losses at 50 rpm can be seen in Table 6.3).

From the table it is observed that the losses on both configurations are similar, however the coupled machine produces more output power for the same amount of input power. This can be explained by the extra low-speed flux-linkage component in the stator. Therefore the coupled configuration exhibits a higher efficiency when compared to the decoupled configuration.

The coupled configuration however exhibits slightly worse torque characteristics. The maximum torque point is 5 Nm lower, which slightly reduces the torque density of the coupled configuration.

From the decoupled measured and simulated results it is observed that the measured results exhibit much larger losses. From this it is clear that unidentified losses still occur in the machine. The high losses could be due to end effects, since end effects are not calculated in 2D simulations. To calculate the losses in 3D, transient analysis is needed. Since magnetic gears are not normally symmetrical, the full machine needs to be modelled, which requires substantial simulation time. Especially if all the mechanical components are investigated.

Table 6.2: Performance Comparison of Decoupled and Coupled Configurations

Test:	**Decoupled**		**Coupled**	
	Simulated	**Measured**	**Simulated**	**Measured**
No-Load: (at rated speed)				
Losses	805.121 W	2.7 kW	812.3 W	2.7 kW
Peak back EMF	280.9	295	312.436	295
Gear ratio	6.687	6.667	6.667	6.667
Load: (at 50rpm)				
Per phase I_{rms}	1.678 A	1.534 A	1.677 A	1.556 A
Per phase V_{rms}	62.611 V	66.468 V	66.182 V	69.3 V
Input mechanical power	440.657 W	861.854 W	457.163 W	861.414 W
Output electrical power	305.796 W	305.97 W	323.074 W	323.03 W
Efficiency at 50rpm	69.4%	35.5%	70.67%	37.5%
Torque:				
Torque ripple	4.918%	8%	5.27%	8.7%
Cogging torque	14.491Nm	48.2Nm	14.32Nm	47.7Nm
Maximum torque point	195.85Nm	200Nm	190.86Nm	195Nm
Torque density (full machine)	9.437kNm/m^3	9.637kNm/m^3	9.197 kNm/m^3	9.396kNm/m^3
Torque density (active gear)	34.989kNm/m^3	37.73kNm/m^3	34.097 kNm/m^3	34.837kNm/m^3

Table 6.3: Losses of MGAFG at 50 rpm

Component	**Decoupled Losses [W]**	**Coupled Losses [W]**
LS Rotor:		
Backplate	23.747	20.884
Laminated Core (Hysteresis and Eddy)	3.731 + 0.195	3.7 + 0.25
Magnets	1.76	1.664
Screws	0.0208	0.0183
Total	**29.45**	**26.681**
HS Rotor:		
Magnets Gear-Side	8.142	8.481
Magnets Stator-Side	6	6.03
Rotor Core	62.99	63.87
Total	**77.132**	**78.381**
Flux-Modulator:		
Hysteresis	2.452	2.994
Eddy Current	0.115	0.147
Stainless-Steel Rods	0.004	0.004
Total	**2.571**	**3.145**
Stator:		
Hysteresis	9.7	9.8
Eddy Current	4.4	4.407
Total	**14.1**	**14.207**
MGAFG Total	**123.203**	**122.714**

CHAPTER 7

CONCLUSION AND RECOMMENDATIONS

In this thesis there is a description of a design approach that was developed whereby a magnetically geared permanent magnet generator was optimised subject to performance constraints. With the optimised design a prototype machine was built and experimentally evaluated.

The problems to solve set out in Section 1.3.1 are addressed in previous chapters. The key conclusions and findings may be summarised as follows:

- The axial-flux topology chosen for the prototype machine was the first magnetically geared axial-flux machine that was experimentally evaluated. The disadvantage of this topology is that the forces are predominantly in one direction, they do not counter each other as in radial machines. However the axial topology allowed for easy observability of the prototype machine.
- The prototype machine was designed for wind energy conversion applications, for which MGs may solve the following problems:
  - An MG transfers power without contact between moving parts, which allows for lubricant free operation and little or no maintenance. However, before a MG is implemented in wind turbines the design should be further simplified to allow for easy assembly and maintenance.
  - MGs offer high torque densities, which may reduce the overall weight and size of wind energy conversion systems.
  - MGs allow for inherent overload protection, which may offer additional protection to wind turbines, however if the maximum torque is exceeded the input speed must be reduced to almost zero velocity before the gear starts to re-engage.
- The magnetically geared generator can be designed in coupled or decoupled configurations. A design approach was formulated for the decoupled approach. The decoupled design approach allows the MG and the PMG to be optimised separately, which significantly decreases the optimisation time required, when compared to the coupled design approach.
- During the optimisation it was realised that the gear needed a larger outer diameter in order to provide a sufficient amount of torque to the generator. The increase in diameter however did not significantly increase the volume of the machine, since the stator's endwindigs are the same diameter as the optimised outer diameter of the gear.

  From the optimisation results it is found that a torque density in excess of 100 kNm/m^3 is obtainable at 50% of the maximum torque in the gear part of the machine.
- The mechanical design was analysed in order to ensure that the prototype machine is mechanically sound.

There are unwanted losses in some mechanical components that are purely for mechanical strength, such as the stainless steel rods in the flux-modulator and the solid steel backplate of the low speed rotor.

To simplify the design only two angular contact ball bearings were chosen for the design, one for each rotor. The limited space between the stator and the flux-modulator leaves little room for a bearing. However, one bearing is sufficient for the high-speed rotor, since the resultant force on the high-speed rotor is countered from both sides of the rotor. The axial force on the low-speed rotor is however predominantly in one direction, thus attention should be paid to the bearing choice for the low-speed rotor. The low-speed rotor is situated at the end of the machine, thus more room is available for bearings. Appendix C gives an alternative bearing configuration for the low speed rotor, which may solve the vibration problems.

- A MGAFG prototype machine was manufactured and constructed in this project. The machine was configured to allow for the decoupled and the coupled configurations.

  The most time consuming aspect of the assembly process of the prototype machine was the positioning of the components to ensure that PMs on the rotors do not stick to other components. The high grade PM material used greatly complicated the assembly process.

  Due to the large axial forces, as a conservative measure, the air-gaps of the prototype was increased to 4mm, which is twice as much as the designed value.

- For the experimental evaluation the prototype machine was evaluated by testing the machine at no-load and at load.

  From the no-load tests it was observed that for rated input speed (150rpm) the losses of the machine were almost 2.7 kW. High losses were observed in the backplate of the low-speed rotor by measuring the difference in temperature of different parts of the machine. The ohmic losses of the low-speed rotor were simulated in 2D and 3D. For both simulations the losses in the backplate were observed to be about 530 W.

  Apart from the windage and bearing losses, the underestimated losses may be attributed to the following aspects:

  - The low speed laminated core were machined to get the rotor parallel and concentric, this compromised the electrical insulation of the laminated core.
  - Unparallel discs may have caused additional high harmonics in the low speed rotor.
  - Losses may have been caused due to vibration in the low-speed rotor.

  Since the machine exhibited such high losses, the load tests were measured at low speeds, which kept the losses to a minimum. The tests were performed between 25rpm and 50rpm, with a three phase 30Ω load. With the results the efficiency at different input speeds were calculated. The efficiency for the decoupled configuration were measured to be 35.5 %. The losses calculated in

the simulated results were however much lower than the losses measured in the prototype, thus the efficiency of the simulated models were higher.

The pull out torque of the machine were measured to be just under 200 Nm. To determine the factors that decreased the pull-out torque a number of simulations were performed (see Table 7.1 for the summary).

- The prototype was experimentally evaluated for the decoupled and the coupled configurations.

  From the experimental evaluation results it was observed that the losses on both the decoupled and the coupled configurations are similar, however the coupled machine produces more output power for the same amount of input power. This can be explained by the extra low-speed flux-linkage component in the stator for the coupled configuration. Therefore the coupled configuration exhibits a higher efficiency when compared to the decoupled configuration.

Not all of the losses could be explained with electromagnetic simulations. To accurately determine the losses it is necessary to first fix the mechanical problems made in the prototype, such as; the vibration in the low-speed rotor and to get the air-gap distance correct and even throughout the machine. If the major mechanical problems are solved the experimental results should compare more closely to the simulated results.

Even though the performance of the prototype machine were lower than expected, the advantages that magnetically geared machines offer over traditional mechanically geared machines are substantial. If the mechanical complexities of the prototype machine are solved the design efficiency and the design torque density can still be reached.

7.1 Recommendations

Apart from some recommendations made throughout this thesis, the following recommendations regarding future developments of magnetically geared machines are proposed:

Optimisation Aspects:

- In the optimisation the torque density of the machine is the main concern. The main concern should be the efficiency, with the torque density and the cost of the machine as secondary concerns.

Table 7.1: Pull-Out Torque Reduction due to Component

Component	Torque Reduction [Nm]
Low Speed Rotor Backplate	14.898
Low Speed Rotor Screws	20.067
High Speed Rotor Screws	4.784
Flux-Modulator Shape and Rods	40.018

- The high-speed rotor can be configured with only one row of PMs. The machine will then be permanently in the coupled configuration, which will increase the efficiency and the torque density. The torque density will increase since the axial length of the machine would decreases. However the decrease in space will leave little room for mechanical strengthening.
- With a full-scale frequency converter used to regulate the output power, the machine could be designed to operate at a higher frequency. This could make more use of the high gear ratios obtainable in a single stage in MGs.
- From (77) it was found that fractional gear ratios exhibits the lowest cogging torque and from (87) that the cogging factor f_c is the lowest for fractional gear ratios.
- Since magnetically geared machines normally exhibit no symmetry, the full machine needs to be modelled in FEM, thus it is better to optimise the machine in 2D and only to verify the results in 3D.

Mechanical Aspects:

- If a MG is used as an alternative to mechanical gears in renewable energy applications for the advantage of little to no maintenance. Special care should be given to the parts that still needs to be maintained. For example the bearings should be easily replaceable. This is complicated by the high number of components that rotate relative to each other in magnetically geared machines.
- The high losses in the low-speed rotor backplate could have been prevented if the backplate was simulated in FEM before the design was finalised. In future development the following changes to the low-speed rotor could be made in order to minimise losses:
  - The laminated core could be enlarged to ensure that no magnetic flux penetrates the solid steel core.
  - Grooves could be cut in the backplate to reduce the size of the induced current paths in the backplate.
  - The backplate could be removed or replaced with a nonferrous alternative, such as stainless steel.

  It is very important to simulate all of the mechanical elements in FEM to determine losses in the components before the design is finalised.
- The screws used to secure the PMs to the rotors must be nonferrous metal, to minimise losses.
- Fibre glass can be added in the epoxy of the flux-modulator to increase the strength of the moulded component.
- The mechanical components should also be optimised to save weight and size, which will further improve the advantages of MGs.

- Utmost care should be taken during the assembly process, because of the high attraction forces between PMs and magnetic materials used.
- If aluminium plate are used as spacers in the air-gaps, the plates chosen should be smaller than the air-gap size to ensure that the plates can be removed after assembly and that the correct air-gap size is still maintained.

Cost Improvements:

Figure 7.1 illustrates the cost percentages of the components used in the prototype. From the figure it is observed the magnetic material used in this prototype is 58.75% of the total cost of the components.

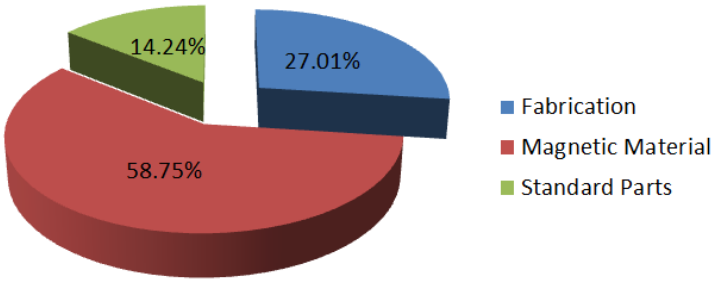

Figure 7.1: Cost of Prototype Parts

Therefore, if the machine is optimised for magnetic material, the cost of producing a machine could significantly be reduced.

Further savings can be made by using using only one row of PMs in the high-speed rotor instead of two.

PM material can also be saved by employing the technique of (75) by inserting PMs with the same polarity into the iron core, thus creating a distributed magnetic field with the same number of pole pairs (see Figure 1.34b). The proposed configuration (75) reduced the magnetic material by 16% while decreasing the pull-out torque by only 5.3%.

Appendices

APPENDIX A

GRAPHS TO ASSIST IN CHOOSING MAGNETICALLY GEARED PARAMETERS

Figure A.1, A.2 and A.3 illustrates the machine parameters for magnetically geared machines for 1,2 and 4 pole-pairs on the high-speed rotor, respectively.

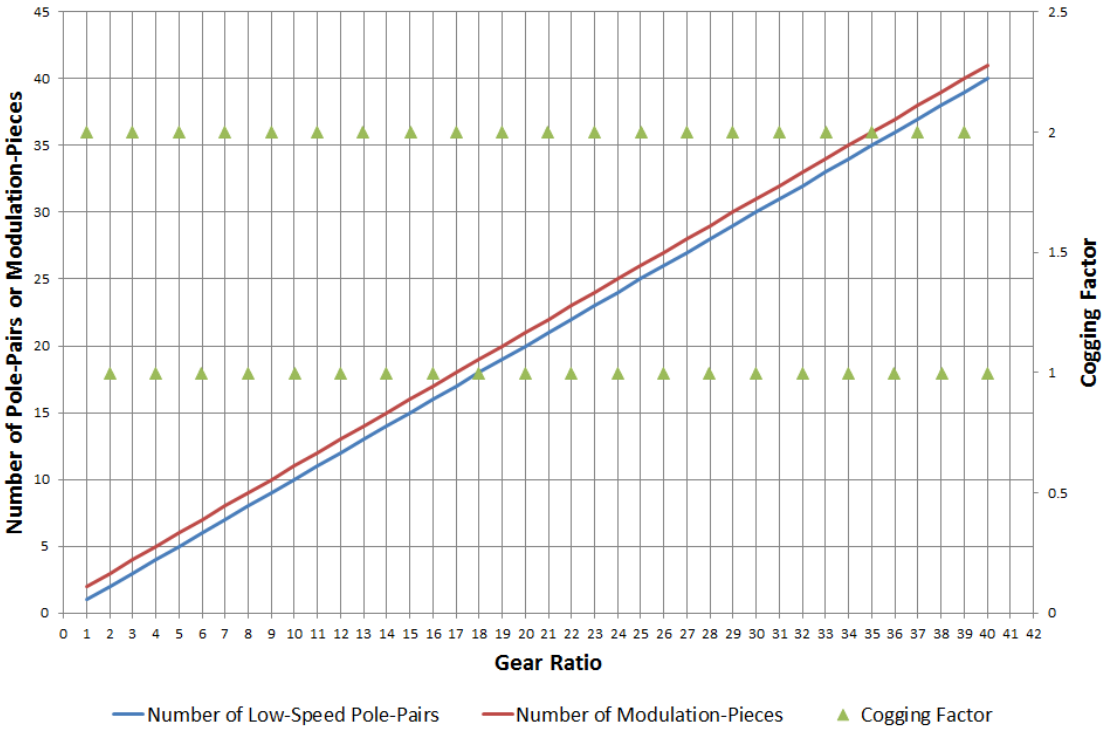

Figure A.1: Machine Parameters for 1 Pole-Pair on the High-Speed Rotor ($p_H = 1$)

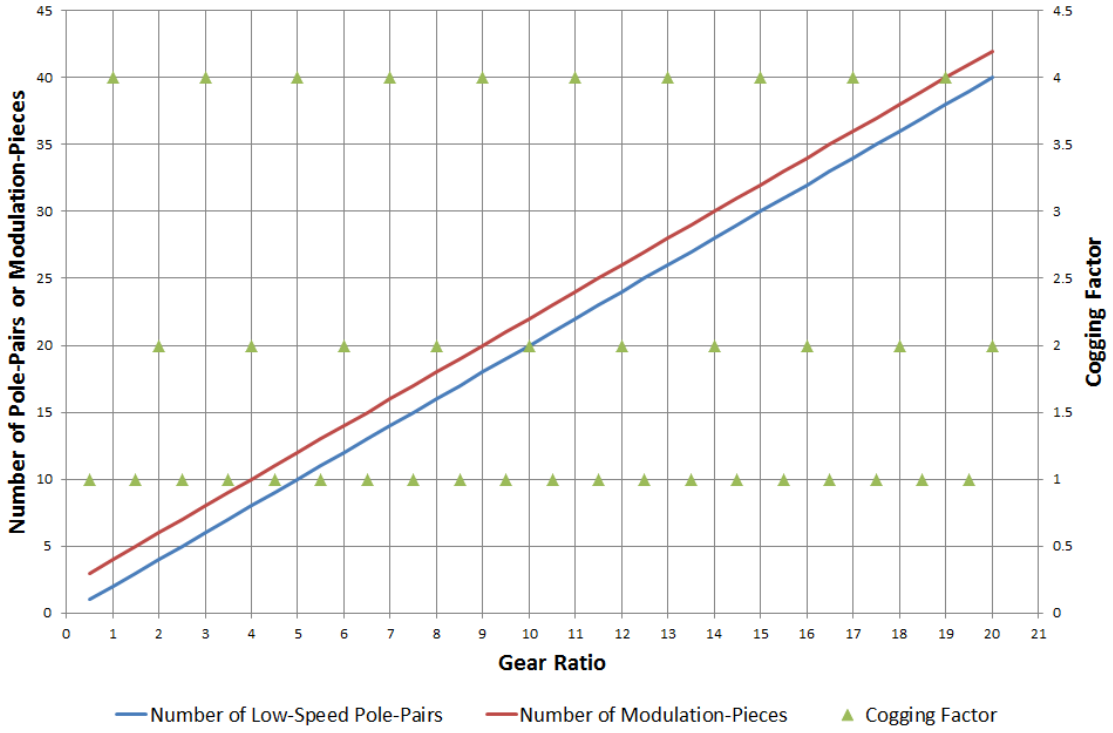

Figure A.2: Machine Parameters for 2 Pole-Pairs on the High-Speed Rotor ($p_H = 2$)

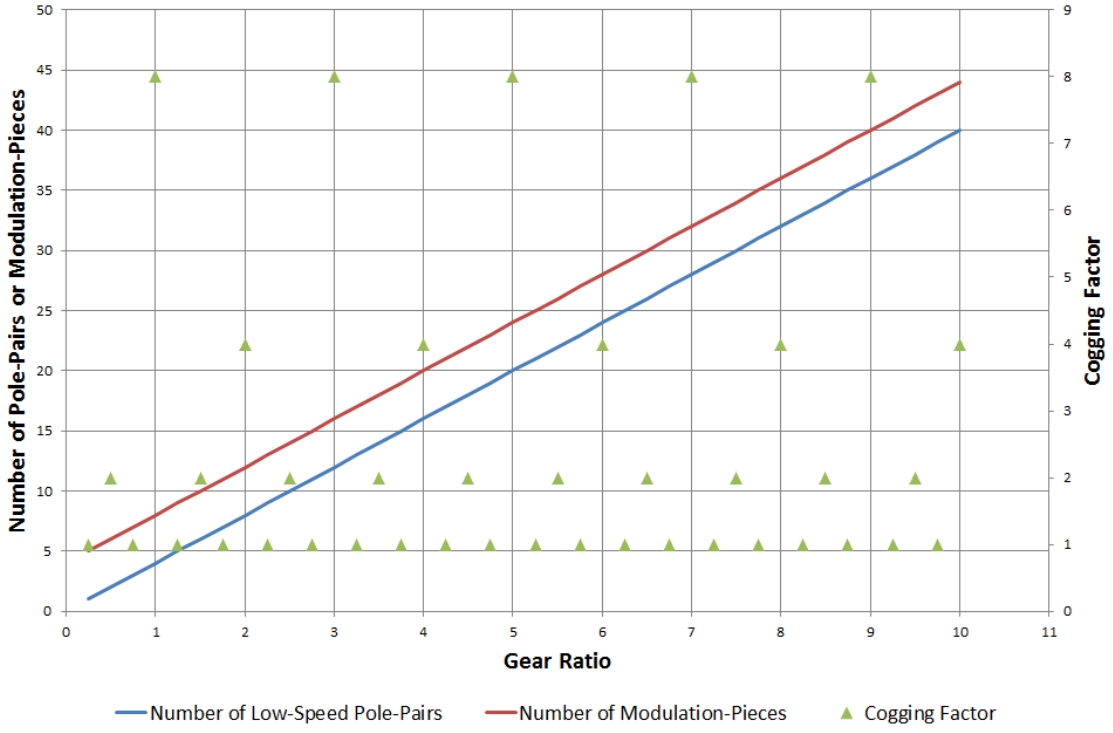

Figure A.3: Machine Parameters for 4 Pole-Pairs on the High-Speed Rotor ($p_H = 4$)

APPENDIX B

FLUX-MODULATOR ASSEMBLY PROCESS

The flux-modulator is manufactured from laminated steel squares to reduce electrical losses. This significantly complicates the assembly process.

The laminated steel squares are assembled onto stainless steel rods for strength and easy assembly. To keep the slope of the component, the squares are stepped in four sections (see Figure B.1).

To strengthen the component the full flux-modulator is moulded in an epoxy resin. The epoxy used is *Ampreg 21* from (103). The mix ratio is 33g hardener for every 100g epoxy resin. Figure B.2 shows the complete lamination stack in the mould. To ensure that the moulded component is released from the mould after the epoxy is cured, the mould is rubbed with silicon grease.

In Figure B.3 the mixed epoxy is poured into the mould and Figure B.4 shows the mould after all the epoxy is poured in. The mould was then baked at 80°C for 5 hours to cure the epoxy (see Figure B.5).

Figure B.6 and B.7 shows the finished flux-modulator.

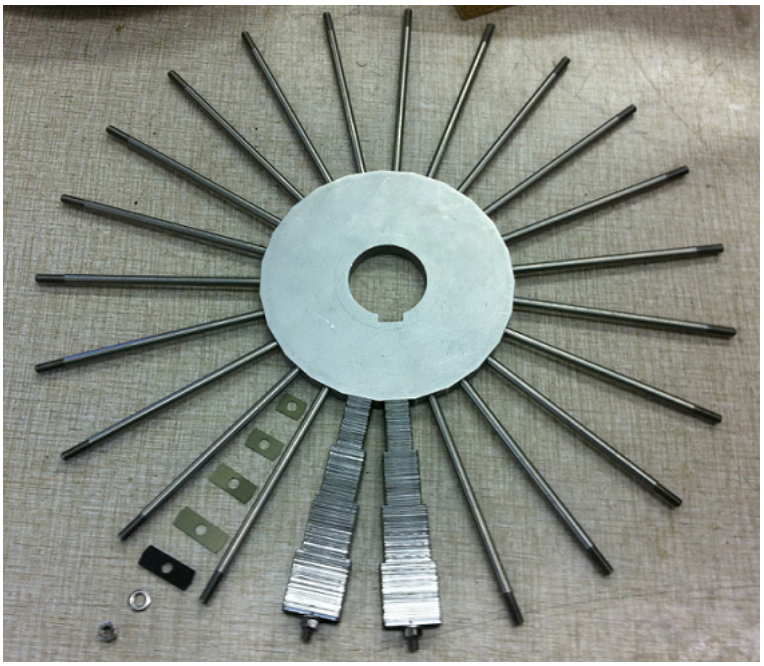

Figure B.1: Laminated Squares Assembly

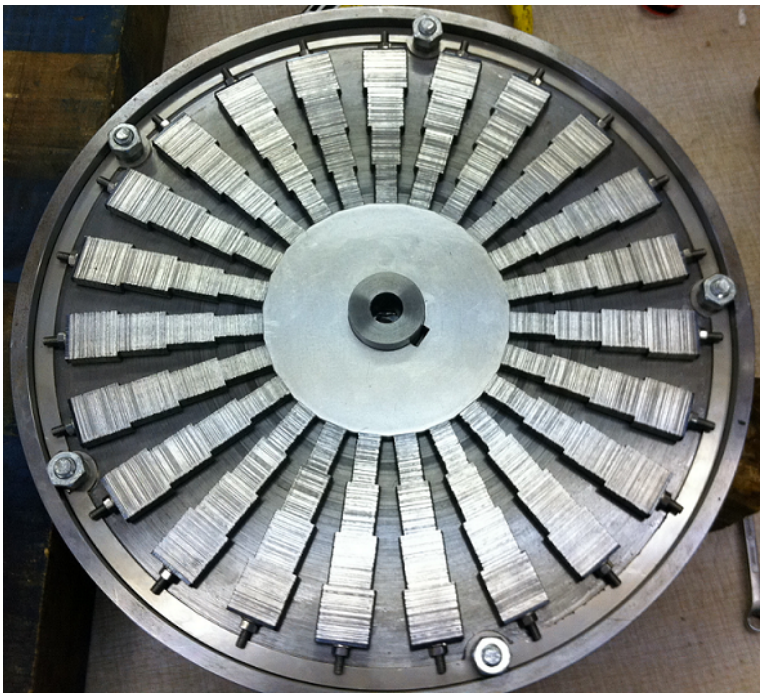

Figure B.2: Assembly in Mould

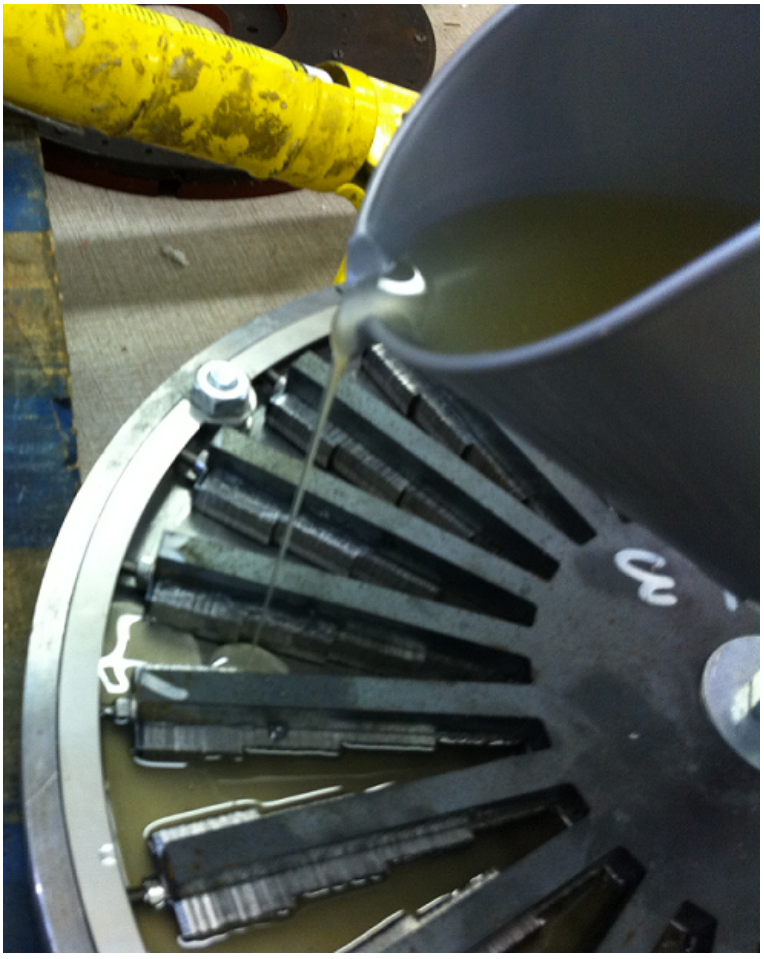

Figure B.3: Epoxy being Poured into Mould

Figure B.4: After the Epoxy is Poured

Figure B.5: Mould being Baked in Oven

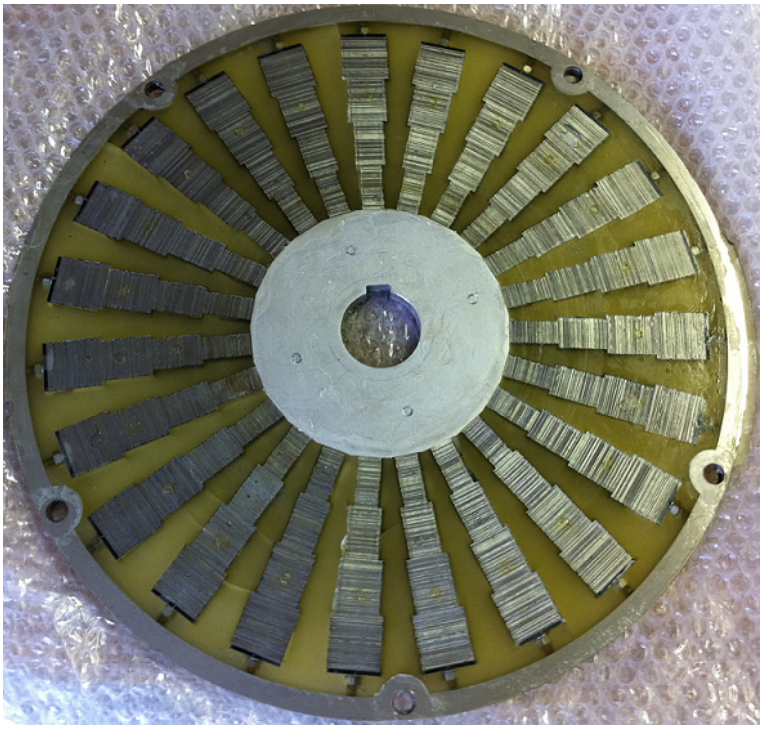

Figure B.6: Finished Flux-Modulator Top View

Figure B.7: Finished Flux-Modulator

APPENDIX C

NEW IMPROVED LOW SPEED ROTOR DESIGN

In this study the low speed bearing vibrated when operational. A new low speed rotor configuration is proposed in this appendix. The double angular contact ball bearing (see Figure C.1) is replaced with a new double row tapered roller bearing (see Figure C.2), the same as used in passenger cars. This bearing can handle more axial force and is wider than the angular contact bearing, therefore the vibration of the rotor will be stabilised and less losses will occur.

Since the tapered roller bearing is bigger than the angular contact ball bearing the low speed rotor bearing holder and the shaft will have to be enlarged with 20mm. Figure C.3(a) shows the old configuration and Figure C.3(b) shows the new improved configuration with the tapered roller ball bearing. The modified shaft and bearing holder's new mechanical drawings is given in Figure C.4 and C.5, respectively.

The tapered roller bearing used is a SKF 31308 J2/QCL7CDF bearing. The power losses is calculated with SKF's power loss calculator (101) and is calculated to be N_R = 0.458 W. The force on the low speed rotor is high and the operational speed is low, thus the SKF calculator suggests that extreme pressure

Figure C.1: Double Row Angular Contact Ball Bearing

Figure C.2: Double Row Tapered Roller Bearing (23)

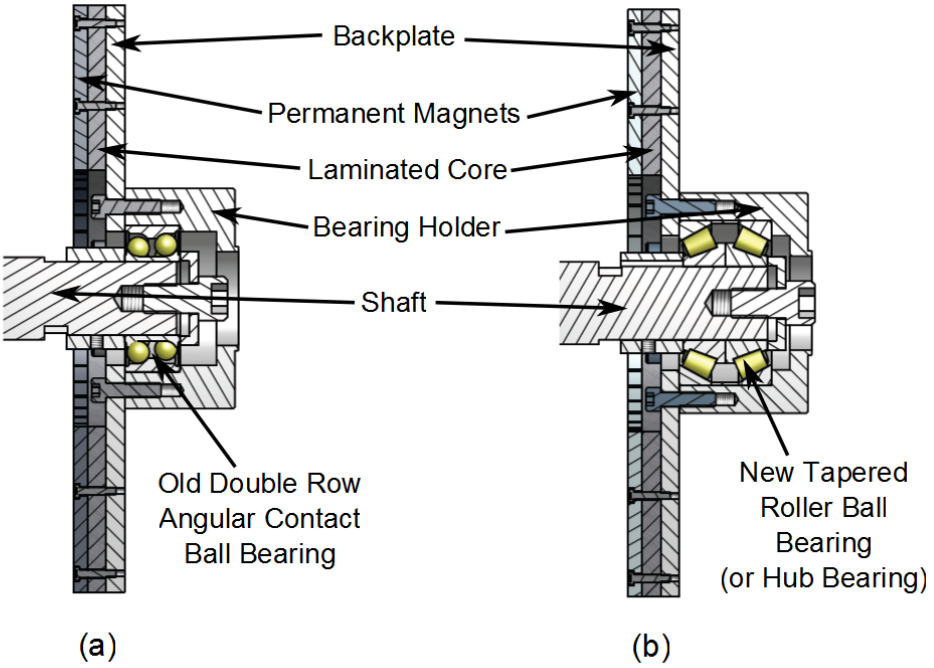

Figure C.3: Low Speed Rotor Configurations: (a) Old Configuration, (b) Improved Configuration

(EP) additives should be added in the bearing lubrication. The rating life for the bearing is calculated to be L_{10h} = 108700 hours.

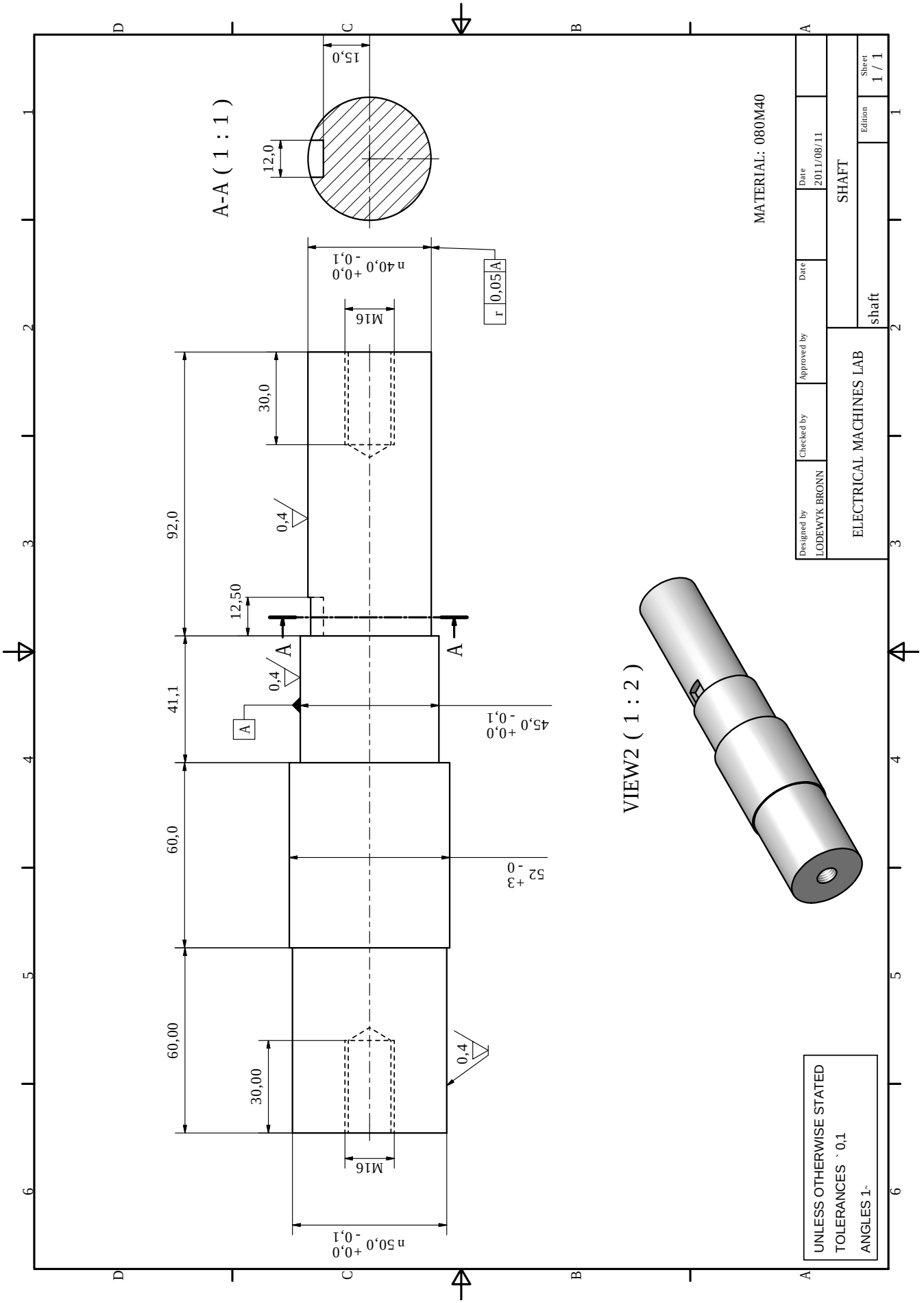

Figure C.4: Modified Shaft for new Tapered Roller Bearing

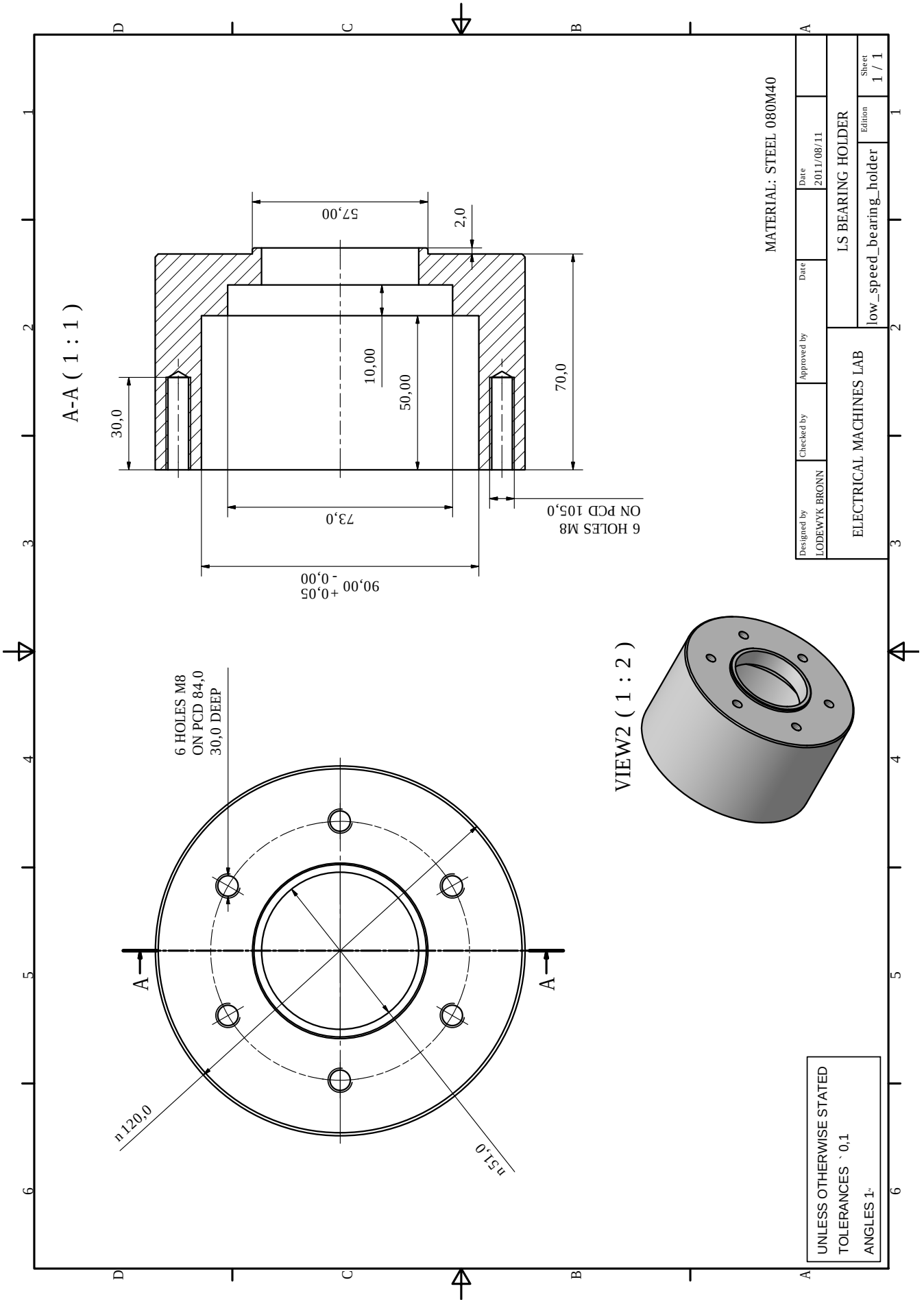

Figure C.5: Modified Low Speed Bearing Holder to House new Tapered Roller Bearing

BIBLIOGRAPHY

[1] C. Armstrong, "Power transmitting device," US Patent 687 292, 1901. (document), 1.2, 1.2, 1.3, 1.2

[2] A. Neuland, "Apparatus for transmitting power," US Patent 1 171 351, 1916. (document), 1.2, 1.4, 1.2, 1.2, 1.2, 1.2.1

[3] L. Chubb, "Vernier motor," US Patent 1 894 979, 1933. (document), 1.2, 1.5

[4] H. Faus, "Magnet gearing," US Patent 2 243 555, 1941. (document), 1.2, 1.6

[5] H. Hurvitz, "Magnetic gearing system," US Patent 2 548 373, 1951. (document), 1.2, 1.7

[6] J. Cluwen, "Magnetic circuits and devices," US Patent 2 722 617, 1955. (document), 1.2, 1.8

[7] M. Baermann, "Permanent magnet device for generating electrical energy," US Patent 3 273 001, 1966. (document), 1.2, 1.9

[8] J. T.B. Martin, "Magnetic transmission," US Patent 3 378 710, 1968. (document), 1.2, 1.11, 1.2, 1.2.1

[9] S. Rand, "Magnetic transmission system," US Patent 3 523 204, 1970. (document), 1.2, 1.13

[10] S. Kikuchi, "Design and characteristics of a new magnetic worm gear using permanent magnet," *IEEE TRANSACTIONS ON MAGNETICS*, vol. 29, no. 6, NOVEMBER 1993. (document), 1.2, 1.17

[11] C. H. D. C. S. W. Y.D. Yao, D.R. Haung and T. Ying, "The radial magnetic coupling studies of perpendicular magnetic gears," *IEEE TRANSACTIONS ON MAGNETICS*, vol. 32, no. 5, 1996. (document), 1.2, 1.18

[12] B. Ackermann and L. Honds, "Magnetic drive arrangement comprising a plurality of magnetically cooperating parts which are movable relative to one another," US Patent 5 633 555, 1997. (document), 1.2, 1.19

[13] K. Atallah and D. Howe, "A novel high-performance magnetic gear," *IEEE TRANSACTIONS ON MAGNETICS*, vol. 37, no. 4, pp. 2844–2846, 2001. (document), 1.2, 1.20, 1.2

[14] F. J. P.O. Rasmussen, T.O. Anderson and O. Nielsen, "Development of a high performance magnetic gear," in *Conference Record of the 38th IAS Annual Meeting in Industry Applications*, vol. 3, 2003. (document), 1.2, 1.21

[15] K. C. L. Jian and J. Jiang, "A magnetic-geared outer-rotor permanent-magnet brushless machine for wind power generation," *IEEE TRANSACTIONS ON INDUSTRY APPLICATIONS*, vol. 45, no. 3, pp. 954–962, MAY/JUNE 2009. (document), 1.22, 1.2, 2.3.1, 3.2

[16] J. W. K. Atallah and D. Howe, "A high-performance linear magnetic gear," *JOURNAL OF APPLIED PHYSICS 97*, vol. 10N516, 2005. (document), 1.2, 1.23, 1.2, 3.2

[17] K. A. S. Mezani and D. Howe, "A high-performance axial-field magnetic gear," *JOURNAL OF APPLIED PHYSICS 99*, vol. 08R303, 2006. (document), 1.2, 1.24, 3.2

[18] S. C. J. Rens, K. Atallah and D. Howe, "A novel magnetic harmonic gear," in *IEEE International Electric Machines & Drives Conference IEMDC '07*, 2007. (document), 1.2, 1.2, 1.28, 1.2, 1.2.1

[19] J. J. C. L. K.T. Chau, D. Zhang and Y. Zhang, "Design of a magnetic-geared outer-rotor permanent-magnet brushless motor for electric vehicles," *IEEE TRANSACTIONS ON MAGNETICS*, vol. 43, pp. 2504–2506, 2007. (document), 1.2, 1.29, 1.2, 1.2, 3.2

[20] Y. W. L.L. Wang, J.X. Shen and K. Wang, "A novel magnetic-geared outer-rotor permanent-magnet brushless motor," *Power Electronics, Machines and Drives, PEMD*, pp. 33–36, 2008. (document), 1.2, 1.31, 3.2

[21] J. Potgieter, "Design and analysis of gearless direct-grid permanent magnet induction wind generator," Master's thesis, Department of Electrical and Electronic Engineering, University of Stellenbosch, 2011. (document), 3.1

[22] P. B. U. Hoffmann and M. Kamper, "Direct grid connection of a slip-permanent magnet wind turbine generator," in *IEEE Energy Conversion Congress and Exposition*, 2010. (document), 3.2

[23] (2011, December) Skf tapered roller bearings. [Online]. Available: http://www.skf.com/portal/skf/home/products?maincatalogue=1&lang=en&newlink=1_14_0 (document), C.2

[24] A. Ragheb and M. Ragheb, "Wind turbine gearbox technologies," in *Proceedings of the 1st International Nuclear and Renewable Energy Conference (INREC10)*, 2010. 1.1, 1.3, 3.2

[25] S. Trout, "Rare earth magnet industry in the usa: Current and future trends," in *For the XVII Rare Earth Magnet Workshop*, 2002. 1.1

[26] T. V. Zweigbergk, "Electric change speed gearing for automobiles," US Patent 1 292 218, 1919. 1.2

[27] G. Reese, "Magnetic gearing arrangement," US Patent 3 301 091, 1967. 1.2, 1.2, 1.2.1

[28] N. Laing, "Magnetic transmission," US Patent 345 650, 1972. 1.2, 1.2

[29] ——, "Centrifugal pump with magnetic drive," US Patent 3 762 839, 1973. 1.2

[30] J. Kaegi and J. Fehr, "Magnetic drive," US Patent 4 146 805, 1979. 1.2

[31] N. Sakai, "Multiple magnet drive pump," US Patent 4 850 821, 1989. 1.2

[32] D. Hesmondhalgh and D. Tipping, "A multielement magnetic gear," *IEEE PROCEEDINGS*, vol. 127, 1980. 1.2

[33] K. Tsurumoto and S. Kikuchi, "A new magnetic gear using permanent magnet," *IEEE TRANSACTIONS ON MAGNETICS*, vol. MAG-23, NO. 5, 1987. 1.2

[34] K. Tsurumoto, "Power transmission of magnetic gear using common meshing and insesibility to center distance," *IEEE TRANSACTION JOURNAL ON MAGNETICS IN JAPAN*, vol. 3, no. 7, 1988. 1.2

[35] ——, "Some consideration on the improvement of performance characteristics of magnetic gear," *IEEE TRANSACTION JOURNAL ON MAGNETICS IN JAPAN*, vol. 4, no. 9, SEPTEMBER 1989. 1.2

[36] ——, "Study of a trial production of magnetic gear with variable circular arc tooth profile," *IEEE TRANSACTION JOURNAL ON MAGNETICS IN JAPAN*, vol. 5, no. 8, AUGUST 1990. 1.2

[37] ——, "Generating mechanism of magnetic force in meshing area of magnetic gear using permanent magnet," *IEEE TRANSACTION JOURNAL ON MAGNETICS IN JAPAN*, vol. 6, no. 6, JUNE 1991. 1.2

[38] ——, "Basic analysis on transmitted force of magnetic gear using permanent magnet," *IEEE TRANSACTION JOURNAL ON MAGNETICS IN JAPAN*, vol. 7, no. 6, 1992. 1.2

[39] ——, "Some improvements of starting characteristics of magnetic gear by eddy current effect," *IEEE TRANSACTION JOURNAL ON MAGNETICS IN JAPAN*, vol. 8, no. 1, JANUARY 1993. 1.2

[40] N. T. K. Tsurumoto, S. Togo and S. Okano, "Characteristics of the magnetic gear using a bulk high-tc superconductor," *IEEE TRANSACTIONS ON APPLIED SUPERCONDUCTIVITY*, vol. 12, no. 1, MARCH 2002. 1.2

[41] S. Kikuchi and K. Tsurumoto, "Trail construction of a new magnetic skew gear using permanent magnet," *IEEE TRANSACTIONS ON MAGNETICS*, vol. 30, no. 6, NOVEMBER 1994. 1.2

[42] J.-P. H. Kyung-Ho Ha and Y.-J. Oh, "Design and characteristic analysis of non-contact magnet gear for conveyor by using permanent magnet," in *37th IAS Annual Meeting in Industry Applications Conference*, 2002. 1.2

[43] S. L. Y.D. Yao, D.R. Haung and S. Wang, "Theoretical computations of the magnetic coupling between magnetic gears," *IEEE TRANSACTIONS ON MAGNETICS*, vol. 32, no. 3, MAY 1996. 1.2

[44] C. L. S. W. D. C. Y.D. Yao, D.R. Huang and T. Ying, "Magnetic coupling studies between radial magnetic gears," *IEEE TRANSACTIONS ON MAGNETICS*, vol. 33, no. 5, SEPTEMBER 1997. 1.2

[45] C. H. D. C. Y.D. Yao, D.R. Huang and S. Wang, "Simulation study of the magnetic coupling between radial magnetic gears," *IEEE TRANSACTIONS ON MAGNETICS*, vol. 33, no. 2, MARCH 1997. 1.2

[46] E. Furlani, "A two-dimensional analysis for the coupling of magnetic gears," *IEEE TRANSACTIONS ON MAGNETICS*, vol. 33, no. 3, MAY 1997. 1.2

[47] S. W. Y.D. Yao, C.M. Lee and D. Huang, "Method of designing optimal bi-axial magnetic gears and system of the same," US Patent 6 047 456, 2000. 1.2

[48] Y. Zhiyi and Z. Han, "Torque calculation and analysis of permanent-magnetic gears," in *International ANSYS Conferenece Proceedings*, 2002. 1.2

[49] T. A. F.T. Jorgensen and P. Rasmussen, "Two dimmensional model of a permanent magnetic spur gear," in *Conference Record of the Fourtienth IAS Annual Meeting in Industry Applications Conference*, 2005. 1.2

[50] A. Landry, "Magnetic transmission," US Patent 3 864 587, 1975. 1.2

[51] B. Ackermann, "Magnetic drive arrangement," US Patent 5 994 809, 1999. 1.2

[52] S. C. K. Atallah and D. Howe, "High-performance magnetic gears," *Journal of Magnetism and Magnetic Materials*, pp. 272–276, 2004. 1.2

[53] J. C. A.G. Razzel, "Compact electrical machine," US Patent 6 794 781 B2, 2004. 1.2, 1.2

[54] A. C. L. Shah and B. Williams, "A magnetic gear box for application with contra-rotating tidal turbine," in *7th International Conference in Power Electronics and Drive Systems PEDS '07*, 2007. 1.2

[55] S. C. K. A. J. Rens, R. Clark and D. Howe, "Design, analysis and realization of a novel magnetic harmonic gear," in *Proceedings of the 2008 International Conference on Electrical Machines*, 2008. 1.2

[56] S. C. J. Rens, K. Atallah and D. Howe, "A novel magnetic harmonic gear," *IEEE TRANSACTION ON INDUSTRY APPLICATIONS*, vol. 46, no. 1, pp. 206–212, 2010. 1.2

[57] T. A. F.T. Jorgensen and P. Rasmussen, "The cycloid permanent magnetic gear," *IEEE TRANSACTIONS ON INDUSTRY APPLICATIONS*, vol. 44, no. 6, pp. 1659–1665, NOVEMBER/DECEMBER 2008. 1.2

[58] J. J. K.T. Chau, D. Zhang and L. Jian, "Transient analysis of coaxial magnetic gears using finite element comodeling," *JOURNAL OF APPLIED PHYSICS*, vol. 103, 2008. 1.2

[59] Y. Z. S. Du and J. Jiang, "Research on a novel combined permanent magnet electrical machine," in *International Conference of Electrical Machines and Systems, ICEMS*, 2008. 1.2, 3.2

[60] K. C. L. Jian and J. Jiang, "An integrated magnetic-geared permanent-magnet in-wheel motor for electric vehicles," in *IEEE Vehicle Power and Propulsion Conference (VPPC)*, 2008. 1.2, 3.2

[61] A. B. W. Hafla and W. Rucker, "Efficient design analysis of a novel magnetic gear on a high performance computer," *The International Journal for Computation and Mathematics in Electrical and Electronic Engineering*, vol. 26, no. 3, pp. 712–726, 2007. 1.2

[62] C. Graham, "A magnetic gearbox arrangement," WO Patent 107 691 A1, 2007. 1.2

[63] K. Atallah and J. Rens, "Electrical machines," WO Patent 125 284 A1, 2007. 1.2

[64] K. Atallah, "Magnetic gear," WO Patent 144 556 A1, 2007. 1.2

[65] R. C. J. R. K. Atallah, S. Calverley and D. Howe, "A new pm machine topology for low-speed, high-torque drives," in *Proceedings of the 2008 International Conference on Electrical Machines*, 2008. 1.2

[66] S. M. K. Atallah, J. Rens and D. Howe, "A novel "pseudo" direct-drive brushless permanent magnet machine," *IEEE TRANSACTIONS ON MAGNETICS*, vol. 55, no. 11, pp. 4349–4352, 2008. 1.2

[67] P. L. W. F. C. W. L.L. Wang, J.X. Shen and H. Hao, "Development of a magnetic-geared permanent-magnet brushless motor," *IEEE TRANSACTIONS ON MAGNETICS*, vol. 45, no. 10, pp. 4578–4581, OCTOBER 2009. 1.2

[68] D. D. C.C. Huang, M.C. Tsai and B. Lin, "Development of a magnetic planetary gearbox," *IEEE TRANSACTIONS ON MAGNETICS*, vol. 44, no. 3, pp. 403–412, 2008. 1.2

[69] A. Reinap and F. Marquez, "Development of a modular linear magnetic gear as a project in the electrical engineering education," in *Proceedings of the 2008 International Conference on Electrical Machines*, 2008. 1.2

[70] M. W. K. Davey and G. Wedeking, "Magnetic gears - an essential enabler for the next generation's electromechanical drives," in *ELECTRICAL MACHINES TECHNOLOGY SYMPOSIUM, (EMTS)*, 2008. 1.2

[71] P. K. L. Yong, X. Jingwei and L. Yongping, "Principle and simulation analysis of a novel structure magnetic gear," in *International Conference of Electrical Machines and Systems, ICEMS*, 2008. 1.2, 2.2

[72] L. Jian and K. Chau, "Analytical calculation of magnetic field distribution in coaxial magnetic gears," *Progress in Electromagnetics Research, PIER 92*, pp. 1–16, 2009. 1.2

[73] Y. G. J. J. C. Y. L. Jian, K.T. Chau and W. Li, "Comparison of coaxial magnetic gears with different topologies," *IEEE TRANSACTIONS ON M*, vol. 45, no. 10, pp. 4526–4529, 2009. 1.2

[74] L. Jian and K. Chau, "Design and analysis of an integrated halbach-magnetic-geared permanent-magnet motor for electric vehicles," *Journal of Asian Electric Vehicles*, vol. 7, no. 1, pp. 1213–1219, 2009. 1.2

[75] J. J. X. Liu, K.T. Chau and C. Yu, "Design and analysis of interior-magnet outer-rotor concentric magnetic gears," *JOURNAL OF APPLIED PHYSICS 105*, vol. 07f101, 2009. 1.2, 7.1

[76] N. Frank and H. Toliyat, "Gearing ratios of a magnetic gear for marine applications," in *IEEE Electric Ship Technologies Symposium, ESTS.*, 2009. 1.2

[77] ——, "Gearing ratios of a magnetic gear for wind turbines," in *IEEE International Electrical Machines and Drives Conference, IEMDC'09.*, 2009. 1.2, 3.3.1, 7.1

[78] H. T. H. M. P.O. Rasmussen, T.M. Jahns and T. Matzen, "Motor integrated permanent magnet gear with a wide torque-speed range," in *IEEE Energy Conversion Congress and Exposition, ECCE.*, 2009. 1.2, 3.2

[79] W. Fu and S. Ho, "A quantitative comparative analysis of a novel flux-modulated permanent-magnet motor for low-speed drive," *IEEE TRANSACTIONS ON MAGNETICS*, vol. 46, pp. 127–134, 2010. 1.2

[80] S. C. K. Atallah and D. Howe, "Design, analysis and realisation of a high-performance magnetic gear," in *IEEE Proceedings in Electric Power Applications*, 2004. 2.2

[81] K. V. d. W. R.J. Wang, M.J. Kamper and J. Gieras, "Optimal design of a coreless stator axial flux permanent-magnet generator," *IEEE TRANSACTIONS ON MAGNETICS*, vol. 41, pp. 55–64, 2005. 2.3.1, 2.3.1

[82] J. Gieras and M. Wing, *Permanent Magnet Motor Technology*, 2nd ed. Marcel Dekker, Inc., 2002. 2.3.1

[83] F. White, *Fluid mechanics - Fifth edition*. McGraw Hill, 2003. 3.1

[84] J. M. J.F. Manwell and A. Rogers, *Wind energy explained - Theory, design and application*. John Wiley & Sons Ltd, 2003. 3.1

[85] N. J. T. Burton, D. Sharpe and E. Bossanyi, *Wind energy handbook*. John Wiley & Sons Ltd, 2008. 3.1, 3.1

[86] J. Stander, "The specification of a small commercial wind energy conversion system for the south african anatartic research base sanae iv," Master's thesis, University of Stellenbosch, Department of Mechanical and Mechatronic Engineering, 2008. 3.1

[87] Z. Q. Zhu and D. Howe, "Influence of design parameters on cogging torque in permanent magnet machines," *IEEE Transactions on Energy Conversion*, vol. 15, pp. 407–412, 2000. 3.3.1, 4.5.4, 7.1

[88] (2011, November) Magnet 7.1.2, infolytica corporation. [Online]. Available: http://www.infolytica.com/en/products/magnet/ 4.1.1

[89] R. Eberhart and J. Kennedy, "A new optimizer using particle swarm theory," *Proceedings of Sixth International Symposium on Micro Machine and Human Science*, 1995. 4.2.1

[90] J. Kennedy and R. Eberhart, "Particle swarm optimization." *Proceedings of IEEE Conference on Neural Networks*, pp. 1942–1948, 1995. 4.2.1

[91] ——, "Swarm intelligence," *Morgan Kaufmann Academic Press*, 2001. 4.2.1

[92] R. W. L. Bronn and M. Kamper, "Development of a shutter type magnetic gear," in *Proceedings of the 19th Southern African Universities Power Engineering Conference, SAUPEC*, 2010. 4.3, 5.3.4

[93] J. Potgieter and M. Kamper, "Cogging torque sensitivity in design optimisation of low cost non-overlap winding pm wind generator," in *XIX International Conference on Electrical Machines (ICEM)*, 2010. 4.5.4

[94] N. Bianchi and S. Bolognani, "Design techniques for reducing the cogging torque in surface-mounted pm motors," *IEEE Transactions on Industry Applications*, vol. 38, 2002. 4.5.4

[95] W. Fei and P. Luk, "Torque ripple reduction of axial flux permanent magnet synchronous machine with segmented and laminated stator," *IEEE Transactions on Magnetics*, vol. 45, 2009. 4.5.4

[96] T. L. M. Aydin, Z. Q. Zhu and D. Howe, "Minimization of cogging torque in axial-flux permanent-magnet machines: Design concepts," *IEEE Transactions on Magnetics*, vol. 43, 2007. 4.5.4

[97] S. M. M.S. Islam and T. Sebastian, "Issues in reducing the cogging torque of mass-produced permanent-magnet brushless dc motor," *IEEE Transactions on Industry Applications*, vol. 40, 2004. 4.5.4

[98] M. H. W. C. C. Hwang and S. P. Cheng, "Influence of pole and slot combinations on cogging torque in fractional slot pm motors," *Journal of Magnetism and Magnetic Materials*, vol. 304, pp. 430–432, 2006. 4.5.4

[99] S. H. S.A. Saied, K. Abbaszadeh and M. Fadaie, "A new approach to cogging torque reduction in surface-mounted permanent-magnet motors," *European Journal of Scientific Research*, vol. 26, pp. 499–509, 2009. 4.5.4

[100] L. Dosiek and P. Pillay, "Cogging torque reduction in permanent magnet machines," *IEEE TRANSACTIONS ON INDUSTRY APPLICATIONS*, vol. 43, pp. 1565–1570, 2007. 4.5.4

[101] (2011, November) Skf frictional moment - power loss calculations. [Online]. Available: http://www.skf.com/skf/productcatalogue/calculationsFilter?lang=en&newlink=&prodid=&action=Calc5 5.3.2, C

[102] (2011, November) Armstrong magnetics, inc. [Online]. Available: http://www.armsmag.com/neodymium.htm 6.2.4

[103] (2011, September) Amt composites - product groups. [Online]. Available: http://www.amtcomposites.co.za/ac_epoxy.html B